2012

Investigation of doped ZnO by Molecular Beam Epitaxy for n- and p-type Conductivity

Huiyong Liu
Virginia Commonwealth University

Investigation of doped ZnO by Molecular Beam Epitaxy for n- and p-type Conductivity

A dissertation submitted in partial fulfillment of the requirements for the degree of Doctor of Philosophy at Virginia Commonwealth University

by

Huiyong Liu

Bachelor of Engineering in Electrical Engineering
Shenyang Normal University, Shenyang, China, 2002

Master of Science in Optical Engineering
Rose-Hulman Institute of Technology, Terre Haute, Indiana, USA, 2007

Director: Dr. Hadis Morkoc
Founders Professor of Electrical and Computer Engineering

Virginia Commonwealth University
Richmond, Virginia
August 2012

Acknowledgements

My deepest and sincere appreciation first goes to my advisor, Professor Hadis Morkoç, for his support, guidance, and faith in both me and my project during these years. This dissertation simply would not have been possible without his supervision and encouragement.

I am indebted to my Ph.D. committee members, Professors S. Bandyopadhyay, A. Baski, M. Reshchikov, Ü. Özgür, and Dr. V. Avrutin, for their time and effort. Their advice and support are highly appreciated throughout this endeavor.

I have also benefited from many friends and co-workers inside and outside the VCU community. I would like to express my gratitude to my friends and co-workers, including Mr. X. Li, Mr. F. Zhang, Dr. N. Izyumskaya, Dr. H. Gao, Dr. X. Gu, Dr. B. Xiao, Dr. J. Xie, Dr. X. Ni, Dr. Q. Fan, Mr. M. Wu, Ms. J. Nie, Prof. P. Voyles, Dr. A. Kvit, Mr. A. Yankovich, and any others who I may forgotten, for their suggestions, assistance, and friendship.

Finally, I would like to thank my parents and my younger sister for their selfless love, support, and encouragement. Special thanks to my wife, Lili Ding, and my uncle, Hongwei Liu for their understanding and caring. I am proud of you all.

Table of Contents

List of Tables

List of Figures

Abstract

Investigation of doped ZnO by Molecular Beam Epitaxy for n- and p-type Conductivity

Huiyong Liu, Ph.D

A dissertation submitted in partial satisfaction of the preliminary examination requirements for the degree of Doctor of Philosophy in Electrical and Computer Engineering at Virginia Commonwealth University

Supervisor: Dr. Hadis Morkoç

This dissertation presents an investigation of the properties, especially the electrical properties, of doped ZnO films grown by plasma-assisted molecular beam epitaxy (MBE) under different conditions. The interest in investigating ZnO films is motivated by the potential of ZnO to replace the currently dominant ITO in industries as n-type transparent electrodes and the difficulty in achieving reliable and reproducible p-type ZnO. On the one hand, n-type ZnO heavily doped with Al or Ga (AZO or GZO) is the most promising to replace ITO due to the low cost, abundant material resources, non-toxicity , high conductivity, and high transparency. On the other hand, ZnO doped with a large-size-mismatched element of Sb (SZO) or co-doped with N and Te exhibits the possibility of achieving p-type ZnO.

In this dissertation, the effects of MBE growth parameters on the properties of GZO have been investigated in detail. The ratio of oxygen to metal (Zn+Ga) was found to be critical in affecting the structural, electrical, and optical properties of GZO layers as revealed by x-ray diffraction (XRD), transmission electron microscopy (TEM), Hall measurement, photoluminescence (PL), and transmittance measurements. Highly conductive ($\sim 2\times10^{-4}$ Ω-cm) and transparent GZO films (> 90% in the visible spectral range) were achieved by MBE under metal-rich conditions (reactive oxygen to incorporated Zn ratio < 1). The highly conductive and transparent GZO layers grown under optimized conditions were applied as p-side transparent electrodes in InGaN-LEDs, which exhibited many advantages over the traditional thin semi-transparent Ni/Au electrodes. The surface morphologies of GaN templates were demonstrated to be important in affecting the structural and electrical properties of GZO layers. In those highly conductive and transparent GZO layers with high-quality crystalline structures, studies revealed ionized impurity scattering being the dominant mechanism limiting the mobility in the temperature range of 15-330 K, while polar optical phonon scattering being the mechanism responsible for the temperature-dependence for T>150 K. The majority Sb ions were found to reside on Zn sites instead of O sites for lower Sb concentrations (~0.1 at.%), which can lead to a high electron concentration of above 10^{19} cm^{-3} along with a high electron mobility of 110 cm^2/V-s at room temperature. The reduction in electron concentration and mobility for higher Sb concentrations (~1 at.%) was caused by the deterioration of the crystalline quality. ZnO co-doped with N and Te was also studied and the advantages of the co-doping technique and problems in achieving p-type conductivity are discussed.

Chapter 1: Introduction

The semiconductor material of zinc oxide (ZnO) is an attractive material for applications in electronics, photonics, acoustics, and sensing.[1] ZnO has grained substantial interest in optoelectronics application mainly due to its direct wide band gap of ~3.3 eV at 300 K and large exciton binding energy of ~60 meV, which permits excitonic emission at room temperature (RT) and above because this value is 2.4 times that of the RT thermal energy (25 meV). [2]

1.1 Motivation

Unfortunately, ZnO suffers from the doping asymmetric problem (also dubbed as the p-type problem) which means it is easy to achieve strong n-type ZnO but very difficult to create consistent, reliable, high-conductivity p-type material.[3,4] The lack of reproducible and low-resistivity p-type ZnO is the main obstacle to the applications of ZnO in optoelectronic devices such as light-emitting diodes (LEDs) and laser diodes (LDs).[2,3,4]

In the realm of p-ZnO, nitrogen (N) is widely regarded as the most promising p-type dopant in ZnO since it can substitutes a chalogen atom and forms a shallow acceptor[5] due to its similar ionic radius to that of oxygen[6]. Look et al. [4] summarized the pertinent data of most of ZnO:N with p-type behaviors grown by different deposition techniques. Although many reports of ZnO:N being p-type materials are available in literatures, problems are also reported. It was found that the crystal quality of ZnO films with the incorporation of N atoms exhibited serious degradation which hampers p-type conductivity.[6,7] The formation of $(N_2)_O$ defects having sufficiently low energies converts $(N)_O$ acceptors into donors, which along with the low solubility of N hinders the p-type conductivity.[8, 9] To achieve high N concentration and high crystalline simultaneously, the technique of co-doping of N and Te was recently proposed[10], which need to be examined carefully.

Recently, some groups also reported p-type behaviors of ZnO doped with large-size-mismatched group-V elements (As, Sb) and proposed that the p-type behaviors are due to the As_{Zn}-$2V_{Zn}$ or Sb_{Zn}-$2V_{Zn}$ complexes. As well known, reports of p-type ZnO have been controversial. Therefore, more careful studies are needed for ZnO doped with large-size-mismatched group-V elements, especially for Sb doped ZnO (SZO) because of few available reports.

On the other track, the potential world-wide shortage of indium has stimulated the investigation of ZnO as an n-type transparent conducting oxide (TCO) to replace the currently dominant indium tin oxide (ITO) in industries.[11] Compared to ITO yielding the lowest resistivities of about 1×10^{-4} $\Omega\cdot$cm it is much more difficult to prepare doped ZnO of such low resistivities[12.] Despite decades of research on ZnO it is not yet clear what the lower limit of the resistivity of such film is.[13] Therefore, it is necessary to study and explain the intrinsic physical limitations that affect the development of ZnO as an alternative to ITO.

The molecular beam epitaxy (MBE) technique, with its precise control over the process parameters, such as substrate temperature and fluxes of the constituent components and dopants, allows one to gain insight into the nature of physical phenomena governing the electrical properties of either n- or p-type ZnO and thus provide valuable information for further improving their characteristics. It is undoubtedly imperative to use MBE technique to grow high-quality doped ZnO and then investigate the origins and the intrinsic physical limitations in the n- or p-type conductivity.

1.2 Objectives

In brief, the objectives of this dissertation include the followings based on the existing problems, doubts, great interests, and the lack of information in literature.

1) For n-type conductivity,
    - to investigate the MBE growth parameter effects on ZnO:Ga (GZO) properties,
    - to apply highly conductive and transparent GZO as transparent electrodes in InGaN based light-emitting diodes (LEDs),
    - to study the nature of mechanisms that limit the mobility in GZO.
2) For p-type conductivity,
    - to investigate the MBE growth parameter effects on SZO electrical properties,
    - to investigate the MBE growth parameter effects on the electrical properties of ZnO co-doped with N and Te (ZnO:[N+Te]).

More detailed information regarding the problems, doubts, great interests, etc. mentioned above can be found in next chapter “Literature Review”.

1.3 Dissertation contents

This dissertation describes the achievements of investigating the properties of GZO, SZO, and ZnO:[N+Te] grown by plasma-enhanced MBE under different conditions as well as the applications of GZO as transparent electrodes in InGaN-based LEDs and the electron transport in heavily doped GZO. This dissertation includes:

Chapter 1: Introduction

A brief introduction of the motivations, objectives, and the organization of this dissertation,

Chapter 2: Literature Review

A relatively detailed literature review of the development of ZnO-based TCOs, the status of MBE-grown GZO and the application of GZO in InGaN-LEDs as well as the controversy in explaining the electron transport in heavily doped ZnO, followed by the review of the development of SZO and ZnO: [N+Te] for p-type conductivity,

Chapter 3: MBE Growth Parameter Effects on GZO Properties

A detailed study of the effects of MBE growth parameters including oxygen pressure, Ga flux, and substrate temperature on the structural, electrical, and optical properties of GZO layers from which highly conductive (resistivity $< 2\times10^{-4}\ \Omega\cdot\text{cm}$) and transparent (transmittance > 90% in the visible range) GZO layers were achieved when metal-rich conditions (reactive oxygen to incorporated Zn ratio < 1:1) were employed,

Chapter 4: Applications of GZO as transparent electrodes in InGaN-LEDs and effects of GaN templates on GZO properties

Applications of highly conductive and transparent GZO layers as p-side transparent electrodes in conventional GaN-based LEDs along with the optimization of post-annealing temperatures to achieve the minimum series resistance, the comparison between LEDs with GZO electrodes and LEDs with typical Ni/Au semi-transparent electrodes, and the effects of GaN template surface morphologies on GZO properties,

Chapter 5: Electron Transport and Physical Limitation in GZO

Numerical fittings to the temperature-dependent Hall mobility curves of GZO layers grown under different conditions with a combination of different scattering mechanisms to explore the physical limitation in the resistivity of heavily doped GZO, where structural properties by X-ray diffraction (XRD) and transmission electron microscopy (TEM) are also provided,

Chapter 6: Doped ZnO for p-type conductivity

Studies of properties of SZO and ZnO:[N+Te] films grown under different conditions by MBE, revealing (i) Sb behaves as donor and highly conductive n-type SZO with a RT mobility of 110 cm^2/V-s along with an electron concentration of ~4.6×10^{20} cm^{-3} can be achieved for a Sb concentration of ~0.1 at% ; (ii) for a higher Sb concentration of ~0.9 at%, both the electron concentration and mobility reduced due to the deterioration of crystal quality and the lattice distortion caused by extra Sb; (iii) ZnO co-doped with N and Te can have much lower conductivities than either N-doped or Te-doped ZnO films and the co-doping technique could have some potential to achieve p-type ZnO ,

Chapter 7 Conclusions

The last chapter of the dissertation which will summarize the key contributions of this dissertation and foresee the future works.

Chapter 2 Literature Review

2.1 Basic properties of TCO

TCO materials are electrically conductive either due to intrinsic defects (oxygen vacancies or metal interstitials) or due to extrinsic dopants (typically a higher-valent metal). The extrinsic dopant concentration of the well-developed TCOs typically varies from 10^{20} to 10^{21} cm^{-3}. Usually, the resistivity, $\rho=1/\sigma$, not the conductivity, σ, is used as the figure of merit which is on the order of 10^{-4} Ω-cm for many TCO materials of practical viability. While the carrier concentration n in TCO is limited by the solubility of dopants, the mobility, μ, is limited by scattering of the charge carriers in the lattice. The detailed discussion of scattering mechanisms will be given later. In short, n and μ cannot be increased simultaneously for heavily doped TCO with homogeneously distributed dopants in the material since they are negatively correlated to each other, which limits the conductivity of TCO.

The transmission window of TCOs is defined by two imposed boundaries. One is in the near-UV region determined by the effective band gap E_g, which is blue shifted due to the Burstein–Moss effect[14]. Owing to high electron concentrations involved the absorption edge is shifted to higher photon energies. The sharp absorption edge near the band edge typically corresponds to the direct transition of electrons from the valence band to the conduction band. The other is at the near-infrared (NIR) region due to the increase in reflectance caused by the plasma resonance of electron gas in the conduction band. The absorption coefficient α is very small within the defined window and consequently transparency is very high.

The positions of the two boundaries defining the transmission window are closely related to the carrier concentration n. For TCOs, both boundaries defining the transmission window shift to shorter wavelength with the increase of carrier concentration n. The blue shift of the onset of absorption in the near UV region is associated with the increase in the carrier concentration blocking the lowest states (filled states) in the conduction band from absorbing the photons. The plasma frequency at which the free carriers are absorbed has a negative correlation with the free carrier concentration. Consequently, the boundary in the near IR region also shifts to the shorter wavelength with increase of the free carrier concentration, as shown in Figure 2.1.

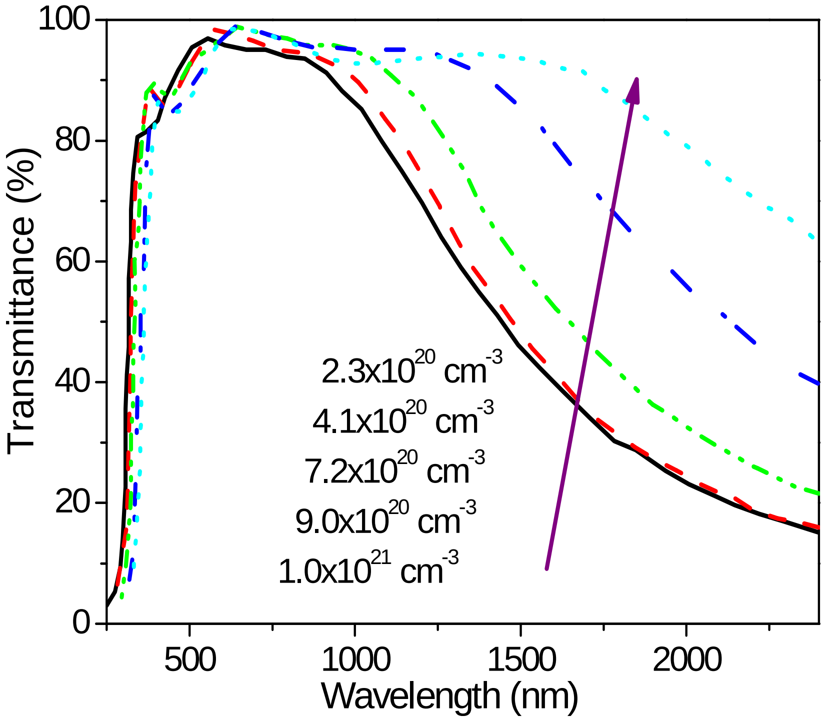

Figure 2.1 Transmittance spectra for GZO films with various carrier concentrations (2.3×10^{20} cm^{-3} to 10×10^{20} cm^{-3}). The two boundaries (in the near-UV and IR-regions) shift to shorter wavelength with the increase of carrier concentration, making the transmittance window narrower (After Shirakata et al. [26**).**

The shift in the near IR region is more pronounced than that in the near UV region. Therefore, the transmission window becomes narrower as the carrier concentration increases. This means that both the conductivity and the transmittance window are interconnected since the conductivity is also related to the carrier concentration as discussed above. Thus, a compromise between material conductivity and transmittance window must be struck, the specifics of which being application dependent. While for LED applications the transparency is needed only in a narrow range around the emission wavelengths, solar cells require high transparency in the whole solar spectral range. Therefore, for photovoltaics, the carrier concentration should be as low as possible for reducing the unwanted free-carrier absorption in the IR spectral range, while the carrier mobility should be as high as possible to retain a sufficiently high conductivity.

2.2 Doped ZnO for n-type TCO

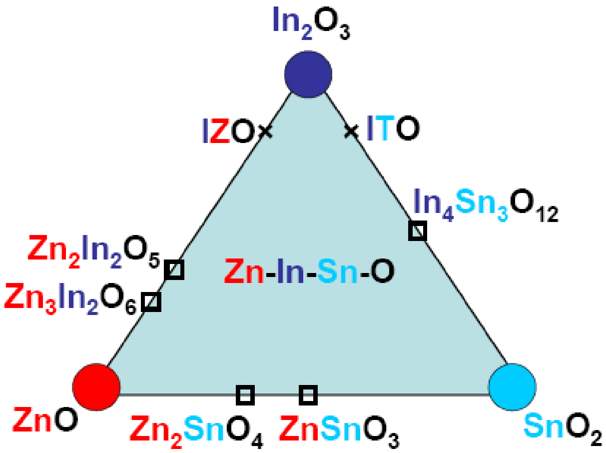

Figure 2.2 TCO semiconductors for thin-film transparent electrodes. (After Minami et al. [15])

Figure 2.2 summarizes the widely recognized n-type TCOs encompassing the In_2O_3-SnO_2-ZnO system for practical applications. ITO is the most widely used In_2O_3-based binary TCO and fluorine-doped tin oxide (FTO) is the dominant in SnO_2-based binary TCOs. In comparison to ITO, FTO is less expensive and shows better thermal stability of its electrical properties [16] as well chemical stability in dye sensitized solar cell. FTO is the second widely used TCO material, mainly in solar cells due to its better stability in hydrogen-containing environment and at high temperatures required for device fabrication. The typical value of FTO's average transmittance is about 80% [17-20]. However, electrical conductivity of FTO is relatively low[17] and it is more difficult to pattern via wet etching as compared to ITO [21].

ZnO with an electron affinity of 4.35 eV and a direct band gap energy of 3.37 eV is typically a n-type semiconductor material with the residual carrier concentration of ~10^{17} cm^{-3} [22]. However, doped ZnO films have been realized with very attractive electrical and optical properties for electrode applications. The dopants that have been used for the ZnO based binary TCOs are Ga, Al, B, In, Y, Sc,V, Si, Ge, Ti, Zr, Hf, and F.[23] Among the advantages of the ZnO-based TCOs are low cost, abundant material resources, and non-toxicity.[24] At present, GZO and ZnO heavily doped with Al (AZO) have been demonstrated to have low resistivity and high transparency in the visible spectral range, which are the most promising ones to replace ITO. The typical transmittance of AZO and GZO is easily 90% or higher[25-27] which is comparable to the best value reported for ITO when optimized for transparency alone and far exceeds that of the traditional semitransparent and thin Ni/Au metal electrodes with transmittance below 70% in the visible range [28]. The high transmittance of AZO and GZO originates from the wide band gap nature of ZnO.[29,30] On the resistivity side, Agura et al.[31] reported a very low resistivity of ~8.5×10^{-5} $\Omega\cdot$cm for AZO, and Park et al.[32] reported a resistivity of ~8.1×10^{-5} $\Omega\cdot$cm for GZO, both of which are similar to the lowest reported resistivity of ~7.7×10^{-5} $\Omega\cdot$cm for ITO[33]. However, most of the reported resistivities for AZO and GZO (particularly prepared by large area coating methods like magnetron sputtering) are in the range of ~$2\text{-}4\times10^{-4}$ $\Omega\cdot$cm which are slightly higher than the typical values for ITO.[12] As compared to ITO, ZnO-based TCOs also show better thermal stability of resistivity[34-36] and better chemical stability at higher temperatures[37,38], both of which bode well for the optoelectronic devices in which this material would be used. Among GZO and AZO, GZO is more stable when subjected to moisture than

AZO[39]. GZO is also more stable with respect to oxidation due to gallium's greater electronegativity in comparison to that of aluminum[40,41]. In addition, the Ga–O covalent bond length (1.92 Å) is very close to the Zn–O bond length (1.97 Å), as compared to those of Al–O (2.7 Å) and In–O (2.1 Å) [42]. The comparable bond length of Ga–O to that of Zn-O allows minimizing deformation of the ZnO lattice even in the case of very high Ga concentrations[43]. From the cost and availability and environmental points of view, AZO appears to be the best candidate to replace ITO. This conclusion is also bolstered by batch process availability for large area and large-scale production of AZO.

Table 2.1 lists the basic properties including the band gap, carrier concentration, mobility, resistivity, and transmittance for ITO, FTO, and AZO/GZO achieved by different deposition techniques. The averaged resistivity of ITO by different techniques is ~1×10^{-4} Ω-cm, which is much lower than that of FTO. For FTO, the typically employed technique is spray pyrolysis which can produce the lowest resistivity of ~3.8×10^{-4} Ω-cm. For AZO/GZO, the resistivities listed here are comparable to or slightly higher than ITO but their transmittance is slightly higher than that of ITO. Obviously, AZO and GZO are promising to replace ITO for transparent electrode applications in terms of their electrical and optical properties. More detailed information regarding the comparisons among them can be found elsewhere[11] and will not be repeated. It must be reiterated that among all the dopants for ZnO-based binary TCOs, Ga and Al are thought to be the best candidates so far.[11]

Table 2.1 Basic properties for ITO, FTO, and AZO/GZO achieved by different depositions techniques. ∗ means unavailable and SP means Spray pyrolysis [reference 11].

TCO	Deposition techniques	Band gap (eV)	Carrier concentration (10^{20} cm^{-3})	Mobility (cm^2/V-s)	Resistivity (10^{-4} Ω-cm)	Transmittance (%) at the wavelengths of interest
ITO	Commercial	∗	∗	∗	1-1.9	∗
ITO	PLD	∗	13.8	53.5	0.845	>80
ITO	SP	∗	18	40	0.95	81
ITO	Sputtering	3.78-3.80	14.6-18.9	25.7-32.7	1.28-1.29	≥80
FTO	SP	4.12-4.18	1.02-9.59	11.1-18.9	∗	≥75
FTO	SP	∗	24.9	6.59	3.8	∗
FTO	SP	3.15-3.57	4.5-7	12-24	3.85-7.51	~80
FTO	CVD	∗	3.05	19	10.9	~80
AZO	MBE	∗	2.1	57	∗	∗
AZO	CVD	3.59	8.7	∗	∗	∗
AZO	Sol-gel	∗	2.5	31	1.2	>90
AZO	Sputtering	∗	~5.5	67	1.4	∗
AZO	Sputtering	∗	15	22	1.9	>80
AZO	Sputtering	∗	9	25	2.7	>85
AZO	Sputtering	3.18-3.36	∗	∗	980	>85
AZO	PLD	∗	13.1	36.7	1.3	89-95
AZO	PLD	∗	15	47.6	0.85	>88
AZO	PLD	3.51-3.86	20.2	16.2	1.91	75-90
GZO	MBE	∗	8.1	42	1.9	>80
GZO	CVD	∗	∗	∗	1.2	>85
GZO	Sputtering	3.37-3.43	1-6	5-35	5.3	~90
GZO	PLD	3.51	146	30.96	0.812	>90
GZO	PLD	∗	64	4.9	2.6	>90

2.3 MBE growth of GZO

It was found that the influence of MBE growth conditions on electrical and optical properties of GZO is scarcely studied. Only the effect of Ga/Zn supply ratio has been reported so far for MBE growth[22,44,45]. Kato *et al.*[44] only investigated ZnO/a-sapphire lightly doped with Ga (n~10^{18} cm^{-3}) which is not applicable as transparent electrodes. Ko *et al.* [22] reported Ga-dped ZnO grown on GaN templates but the maximum carrier concentration achieved is 1.13×10^{20} cm^{-3}, which is still much lower than required for transparent electrode applications. Only Muranaka *et al.* [45] has reported MBE-grown GZO films with a sufficiently low resistivity of 3×10^{-4} Ω-cm and transmittance of >85% in the visible range, which was grown on glass substrate. However, a saturation of carrier density near $4\text{-}6\times10^{20}$ cm^{-3} was observed. In fact, both the carrier concentration and transmittance reported by Muranaka *et al.*[45] are lower than those of GZO/AZO by other deposition techniques. The lack of the reported results from MBE techniques as well as the detailed studies of MBE growth parameters effects requires further investigation towards transparent electrode applications.

2.4 Application of GZO as transparent electrode in GaN-based LEDs

In order for LEDs to be used for general lighting and pave the way for reduced energy consumption, it is imperative for them to produce high luminous fluxes. This necessitates high injection currents, preferably while retaining high power conversion efficiencies. The external quantum efficiency (EQE) of an LED is a convolution of the internal quantum efficiency (IQE) and the photon extraction efficiency[46] as well as another term having to do with the voltage conversion efficiency. The latter term represents the fraction of photons generated that end up escaping the device in the desired direction. Several methods such as textured surfaces, transparent p-contact layers[47] and proper substrate design for reflecting the photons heading in the wrong direction in certain packaging techniques[48] can be employed individually and or in unison to improve the extraction efficiency[49].

TCOs come into play as transparent contacts and have been used in GaN-based LEDs and organic LEDs as transparent electrodes to improve the extraction efficiency and hence the external quantum efficiency. The enhanced lateral conductivity afforded by TCO has added advantages as well. As can be imagined, the performance degradation of LED at high injection levels can in part be due to the poor conductivity of p-type GaN subcontact region which contributes to the so-called “current crowding” or “filamentation” process (formation of regions with relatively higher current densities). Because of the ensuing local heating and increasingly non uniform current injection, the emission efficiency and operation voltage as well as the device reliability are adversely affected. In the early stages of development of GaN based LEDs, a thin Ni/Au layer with a transparency below 70%, which depends on the metal thickness as well as the wavelength, has been investigated extensively as the semi-transparent contact layer [28,50]. In this approach, a compromise must be struck between the need to increase the photon extraction (requires a thinner and well separated contact fingers) and the need for low series resistance of the LEDs (requires the opposite). This undesirable compromise can be avoided by using TCOs. The ohmic-contact technologies on p-GaN layers for GaN-based LEDs with a comprehensive treatment can be found elsewhere[51].

As mentioned earlier, ITO is the dominant TCO in industries which also applies to InGaN-based LEDs. Even beyond the scarcity of In, AZO and GZO are more attractive as transparent electrodes in GaN-based LEDs than ITO, since ZnO and GaN share the same wurtzite crystal structure with a small lattice mismatch of ~1.8%. These favorable structural properties help lay the groundwork for epitaxial growth of ZnO electrodes on GaN LEDs with improved carrier mobility and optical transparency. As the most promising TCO replacing ITO, AZO /GZO was not extensively studied in InGaN-based LEDs. The available reports for AZO[30,36,52] and GZO[53-55] as p-side transparent electrodes are quite few. In the case of GZO which seems more promising as discussed earlier, the three available reports were from two groups, one of which reported a relatively high resistivity of ~5.3×10^{-4} Ω-cm[53] and the other of which reported a relatively low transmittance of ~80% in the near UV and visible wavelength ranges[54,55]. Due to the lack of more detailed information such as the effects of underlying GaN on GZO properties and the effect of activation conditions for n-side ohmic contact on the properties of GZO as well as the LED performance, further studies are still needed.

2.5 Controversy in explaining electron transport in heavily doped ZnO

The reported mobility for GZO and AZO films grown by different techniques scatters from as low as ~5 to as high as 70 $\mathrm{cm^2/V\cdot s}$ for electron carrier concentrations exceeding 10^{20} $\mathrm{cm^{-3}}$.[11] It is generally accepted that the wide dispersion in the mobility is due to the differences in materials quality since the substrate temperature, film thickness, annealing conditions and reactant compositions all affect the electrical properties[56]. However, explanations of electron transport in heavily doped ZnO are still controversial. From a theoretical point of view, the grain-barrier model employed by Seto et al.[57], followed by Bruneaux et al.[58] suggests that the grain boundary scattering is negligible for heavily doped TCOs since the barriers at the grain boundaries are thin enough for electrons to tunnel. The contribution of the grain boundaries to the electron scattering is believed to be entirely screened out by the contribution of the bulk of the crystallites in heavily doped TCOs.[58] The fact just mentioned is supported by Ellmer et al.[59], Minami et al.[60], Steinhauser et al.[61] and Ruske et al.[62]. Minami et al. [60] have concluded that grain boundary scattering is mainly dominant in AZO films with carrier concentrations in the range of 10^{19}-10^{20} cm^{-3} while the ionized impurity scattering is dominant in layers with carrier concentrations in the range of 10^{20}-10^{21} cm^{-3}. Steinhauser et al. [61] concluded that the grain boundaries do not limit the conductivity for carrier concentrations exceeding 1×10^{20} cm^{-3} based on the comparison between Hall mobility and optical mobility for boron-doped ZnO. By comparing the Hall mobility and the optical mobility, Ruske et al. [62] have found that grain boundaries do not limit the conductivity only for ZnO:Al films with a carrier concentration above ~5×10^{20} cm^{-3}. It has to be pointed out that one criterion used to evaluate if grain boundary scattering is important is to compare the mean free path of the carriers and the grain size. The mean free path l can be calculated as [63]

$$l = \left(\frac{h}{2e}\right)\left(\frac{3n}{\pi}\right)^{\frac{1}{3}}\mu$$

Equation 1

which was derived based on free electron degenerated gas. Base on this method, Chen et al.[63] concluded that grain boundary scattering is not important for conductive ITO and AZO. On the other hand, Robbins et al.[64] concluded for nanocrystalline GZO with a carrier concentration of 5.5×10^{20} cm^{-3} and an average grain size of 80 nm that the grain boundary scattering and ionized impurity scattering contribute nearly equally to the overall mobility. Ahn et al.[65] suggested that the grain boundary scattering limits the mobility in GZO with carrier concentrations above 10^{20} cm^{-3} in the temperature range of 190-300 K. The main, and arguably the remaining, issue is the nature of mechanisms that limit the mobility in heavily doped ZnO, which is one of the motivations of this dissertation. Theories regarding the scattering mechanisms and the analyses of experimental data will be discussed later.

2.6 Development of SZO for p-type conductivity

Reliable p-type doping is the major bottleneck limiting the development of high-efficiency devices[66] due to the self-compensating effect from native defects (V_o and Zn_i)[67] and/or H incorporation[68] as well as the well-known low solubility and the deep acceptor levels of the dopants[69].

A few groups have investigated the group-V elements of P, As, Sb with larger ionic radii as compared to O to find better p-dopant. Surprisingly, the group-V elements of P, As, Sb with larger ionic radii as compared to O have also been reported to be p-type dopants in ZnO. Their p-type behaviors are claimed due to complexes such as V_{Zn}-P_O-V_{Zn} complexes[70], As_{Zn}-$2V_{Zn}$ complexes[71,72] , Sb_{Zn}-$2V_{Zn}$ complexes[66]. However, reports of p-type ZnO have been controversial.[73] For examples, in the case of P, it was experimentally proved as a deep acceptor[74] or a donor-like defect of P_{Zn}^{3+}[6]; In the case of As, the majority of As atoms were found to reside on Zn sites which is probably determined by its atomic size and electronegativity rather than its position in the periodic system[71]. Consequently, more careful studies are needed for ZnO doped with large-size-mismatched group-V elements.

Very few studies of SZO were found in literature, which will be discussed below. The first p-type SZO layer with hole concentration of ~5×10^{20} cm^{-3} were reported by Aoki et al.[75] , which were widely questioned due to its high hole concentration. Based on the means of β^- emission channeling from the radioactive ^{124}Sb isotope, Wahl et al.[76] found that the majority of Sb occupy Zn sites, with the possible fraction on O sites being at maximum 5%-6%. Consequently, Wahl et al.[76] doubt whether Sb_O acceptors are responsible for the reported p-type character in SZO layers. Based on the first principle calculation, Limpijumnong et al. [77] proposed that As or Sb occupies Zn position which forms a complex with two spontaneously induced Zn vacancies in a process that involves fivefold As or Sb coordination. Xiu et al.[69] reported reproducible SZO layers grown by electron-cyclotron- resonance-assisted MBE on n-Si (100) substrates, which hole concentration and mobility were $\sim 1.7\times 10^{18}$ cm^{-3} and 20 cm^2/V·s. They claimed that the high hole concentration and mobility are probably due to the Sb_{Zn}-$2V_{Zn}$ complexes. Guo et al.[66] reported p-type SZO layers epitaxially grown by PLD under high oxygen pressure on (0001) sapphire substrates without post-deposition annealing. The electrical properties of their best layers (1.0 at. % SZO) are as follows: hole concentration $\sim 1.9\times 10^{17}$ cm^{-3}, mobility ~7.7 cm^2/V·s, and resistivity ~4.2 ohm-cm. As Guo et al.[66] pointed out, the p-type conductivity closely correlates to the high density of defects which facilitate the formation of acceptor complexes (proposed Sb_{Zn}-$2V_{Zn}$ complexes) and the compensation of native shallow donors. Mandalapu et al.[78] reported homojunctions of n-type ZnO:Ga/ p-type SZO/*p*-Si but the small turn on voltage of 2V for this structure was widely questioned. Yang et al. [79] also reported p-type SZO/n-type ZnO:Ga homojunction grown on 400-nm-ZnO buffered c-plane sapphire substrate and claimed the improvement in output power for this LED is due to the high quality of ZnO grown on *c*-plane sapphire substrate. However, the measured full-width-at-half-maximum (FWHM) of the rocking curve of ZnO (0002) by Yang et al.[79] is only 44 arcseconds, which could be measured from the ZnO buffer instead of SZO layer. If it is really 44 arcseconds, it contradicts with the model of Sb_{Zn}-$2V_{Zn}$ complexes for p-type character as discussed above, which is closely related to high density of defects. Samanta et al.[80] recently reported an excellent p-type SZO (5% Sb in ZnO) with a very high mobility of 57.44 cm^2/V-s along with a hole concentration of 6.25×10^{18} cm^{-3}.

The high mobility of 57.44 cm^2/V-s for p-type ZnO makes itself less convincible since that value is even good for n-type ZnO. Friedrich et al.[81] reported SZO films with different [Sb] grown on MgO (100) substrates by PLD which revealed that the Sb-related phase precipitations such as Sb_2O_4, $Zn_7Sb_2O_{12}$, and $ZnSb_2O_6$ is disadvantageous to achieve p-type doping via Sb_O and/or Sb_{Zn}-$2V_{Zn}$ complexes because most of the Sb atoms is accommodated in large precipitates. There are several more reports for p-type SZO with either low mobility (≤ 2 cm^2/V-s)[82-85,] or low hole concentration (10^{16} cm^{-3})[83, 86] or high resistivity[82,86].

As we can see from the above reports, the reported p-conductivity is achieved for SZO directly or indirectly grown on either Si or sapphire (0001) or glass substrates, which could lead to high interface defect densities and consequently may be responsible for p-type conductivity in some experiments[73]. Meanwhile, Hall-effect measurements on inhomogeneous samples can yield wrong carrier type[87], which need to be carefully examined. To shed more needed light on the dopant behavior of Sb in ZnO, more comprehensive studies are needed.

To use Hall method to evaluate the p-type character, we have to understand the Hall method very well. Look et al.[4] summarized the basics for Hall studies, which will be repeated below for reader's convenience.

Before embarking on a detailed analysis of p-type ZnO, we must first point out that "type" is typically measured in either of two ways, by the Hall effect or the Seebeck effect. The latter arises from a temperature gradient, and will give a p-type response if $p \cdot \mu_p > n \cdot \mu_n$. The Hall effect, on the other hand, requires $p \cdot \mu_p^2 > n \cdot \mu_n^2$ for a p-type indication, which is a more difficult condition to satisfy, since usually $\mu_p = \mu_n$. Thus, a Hall-effect measurement is considered to be a more definitive measure of type. Unfortunately, the Hall voltages measured in p-type ZnO are very small, because the measured hole mobility is often < 1 cm^2/V-s. Also, ohmic contacts to p-type ZnO are difficult to fabricate, and thus noise spikes during one or more of the eight Van der Pauw switching configurations can easily produce an “n-type” result. This problem can sometimes be dealt with by averaging several measurements. Even if the p-type nature can be established, it is still not likely that the mobility and hole concentration can be accurately determined in such samples. Thus, the resistivity becomes the most important factor, and that is what we will use for comparative purposes in this paper. To be more quantitative, caution must be exercised when a Hall analysis gives a mobility > 10 cm^2/V-s, or a hole concentration > 10^{19} cm^{-3}.

2.7 ZnO: [N+Te] for p-type conductivity

One possible strategy for solving the p-type problems could be the use of co-doping.[88] Gallium and aluminum, for example, have been suggested as possible co-dopants for nitrogen-doped ZnO films.[89,90] The reactive III-element was proposed to enhance the incorporation of N acceptor in p-type co-doped ZnO because n-type doping using III-element species reduces the Madelung energy.[91] However, the typical problems such as reduction of emission intensity and/or limits of hole concentration (10^{16} cm^{-3}) still remain, in spite of a high concentration of N atoms (10^{20} cm^{-3}).[92] Recently, the isoelectronic impurity, tellurium (Te), was chosen as a co-dopant.[10,93-97] The anion-rich nature of ZnTe suggests that by mixing with the cation-rich ZnO, a more stoichiometrically balanced material could be achieved. (ZnTe tends to be rich in Te which leads to p-type behavior in the as grown material, whereas, ZnO tends to be rich in Zn which leads to n-type behavior.)[93] Porter et al.[93] proved the strategy of co-doping of N and Te can produce ZnO with resistivity increased by several order of magnitudes, which exhibited the potential to achieve p-type conductivity with further optimization of growth conditions. Park et al. [10,95,96] demonstrated that N and Te co-doping is helpful to improve the crystallinity and N incorporation efficiency simultaneously, which produced p-type conductivity in comparison with ZnO doped with only N.

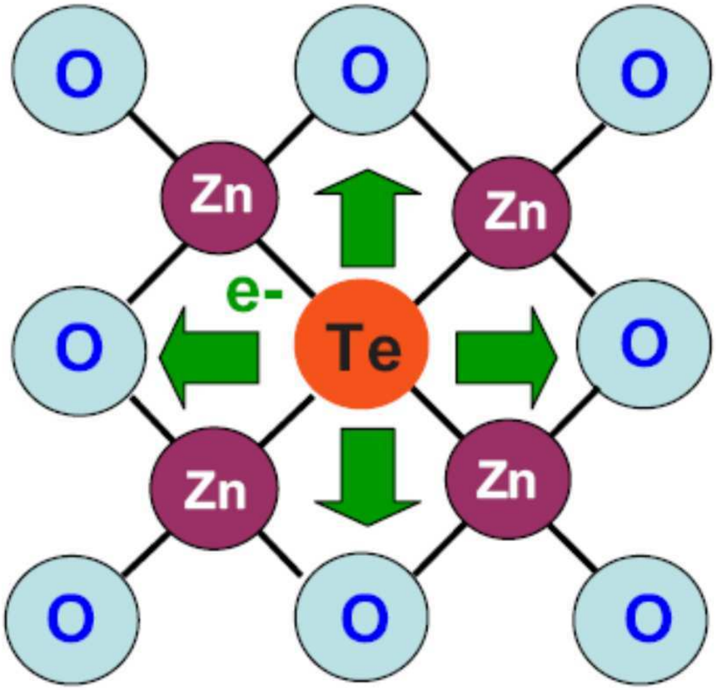

Figure 2.3 The illustration of isoelectronic reaction for Te atoms incorporated into ZnO (after Park et al. [10])

The realization of high quality p-type ZnO with high N concentration by MBE on ZnO substrates could be due to the reduction of Madelung energy when the strategy of N and Te co-doping was used. As given by Park et al.[10] the enhancement of nitrogen solubility by irradiating Te can be understood in terms of a difference in electronegativity. As shown in Figure 2.3, if the Te atoms are incorporated into O atom, they will be positively charged because the electronegativity of Te is relatively smaller than that of O (2.1 vs. 3.44), which consequently makes Te atom an isoelectronic donor. The ZnO:Te films exhibited higher electron concentrations than un-doped ZnO as shown in Table 2.2, which could prove that the explanation of Te atom being an isoelectronic donor is reasonable.[10]

Table 2.2 Electrical properties and N concentration for un-doped, N doped, Te-doped, and N and Te co-doped ZnO films by MBE on ZnO substrates (After Park et al. [95]).

#		N2 flow (SCCM)	J_{Te} (A/S)	[N] (cm^{-3})	n_c (cm^{-3})	Carrier type	μ (cm^2/Vs)	ρ (Ω cm)
A	u-ZnO	-	-	-	4×10^{16}	n	94	1.73
B	ZnO:Te	-	0.01	-	3.6×10^{17}	n	69	0.25
C	ZnO:Te	-	0.03	-	2.4×10^{18}	n	11	0.23
D	ZnO:N	0.5	-	3×10^{20}	2.5×10^{17}	n	8	3
E	ZnO:[N+Te]	0.5	0.03	2×10^{21}	5.8×10^{15}	p	21	49
F	ZnO:[N+Te]	0.5	0.06	1×10^{21}	4×10^{16}	p	11	13

The improvement of crystal quality in the co-doping case is probably due to two reasons. Firstly, the bond lengths of Zn-N (0.201 nm) and Zn-Te (0.263 nm) are different.[96] It is likely that the incorporation of N into ZnO induces contraction of lattice, while Te incorporation would cause expansion of lattice. Thus, the co-doping of both Te and N would help incorporation of N with minimum lattice strain. Secondly, Te may act as a surfactant[96,97] because of the large difference of atomic radii between O (0.066 nm) and Te (0.132 nm)[10], which may partially explain that the co-doping method favors the two-dimensional growth characterized by reflection high energy electron diffraction (RHEED).

It has to be pointed out that the hole concentrations achieved by Park et al.[10,95,96] using the co-doping method are still lower than 10^{17} cm^{-3}. For some layers with lower hole concentrations (~10^{15} cm^{-3}), the mobility is as high as 51 cm^2/V-s.[10] While Tang et al.[97] reported much higher hole concentrations for ZnO:[N+Te] by metal organic chemical vapor deposition, which are

~5×10^{17}- 4×10^{18} cm^{-3} with corresponding mobilities of ~ 10-2 cm^2/V-s. The reports mentioned here could cover all the works related to ZnO co-doped with N and Te available in public literature and the lack of extensive studies makes it still difficult to judge whether this strategy of co-doping are promising as compared with other techniques for p-type ZnO.

Chapter 3: Effects of MBE Growth Parameters on GZO Properties

The growth parameters discussed in this chapter include oxygen pressure during growth, Ga flux controlled by adjusting the Ga effusion cell temperature, and substrate temperature.

3.1 MBE system and preparation of substrates

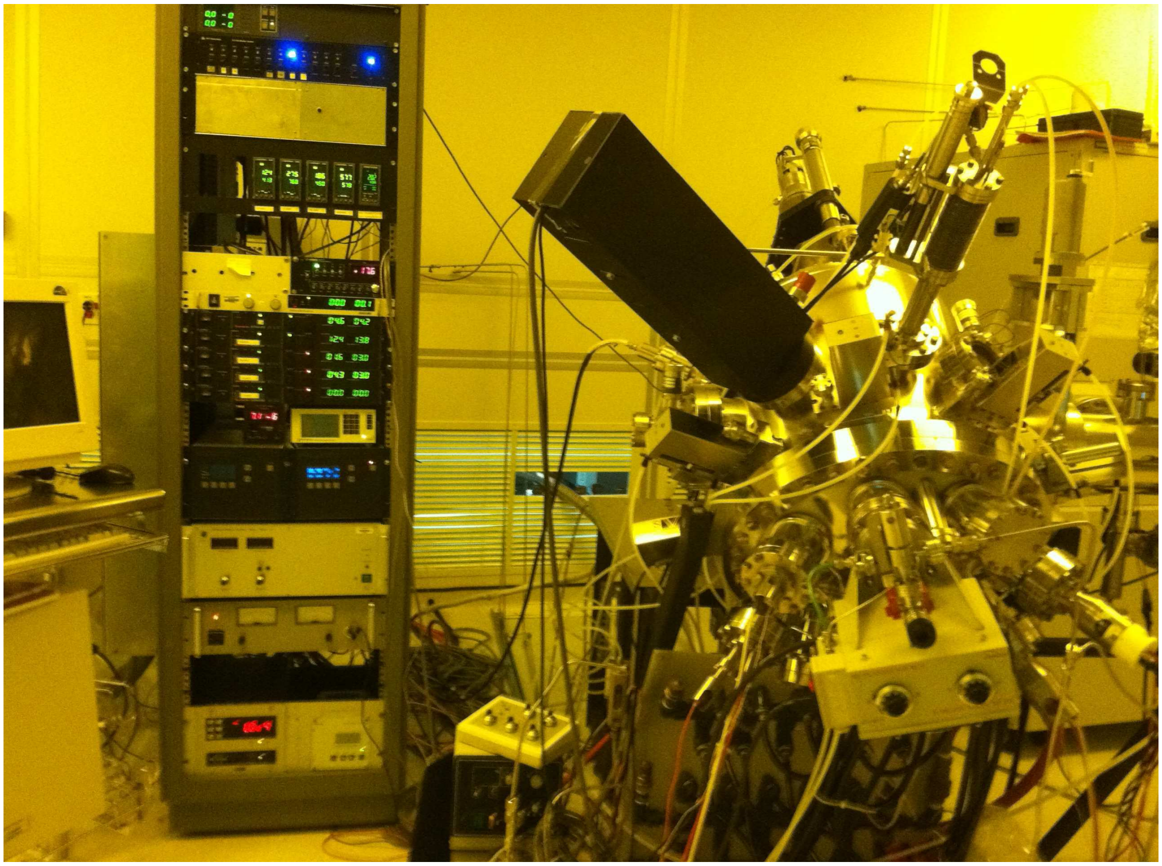

Figure 3.1 MBE manufactured by SVT Associates Inc. equipped mainly with RHEED by Staib Instruments for monitoring the growth of the epitaxy layer, effusion cells with different materials (Zn, Ga, Mg, Te) for elementary sources, and an oxygen RF plasma power supply (Addon Inc).

The MBE system used in the work was manufactured by SVT Associates Inc. with a typical background pressure of 10^{-10} Torr in the growth chamber which is maintained by a turbo pump.

As shown in Figure 3.1, it is equipped mainly with RHEED (Staib instruments) for monitoring the growth of the epitaxy layers *in situ*, Knudsen effusion cells with different materials (Zn, Ga, Te, and Mg) for elementary sources, an oxygen plasma power supply with a RF frequency of 13.56 MHz and a maximum power of 600 W (Addon Inc.). The desired temperatures of effusion cells and substrate heater can be achieved by DC power supplies (Sorensen Inc.) through the feedback of temperature controllers (Eurotherm Inc). The flux of reactive oxygen is controlled by supplying O_2 through a mass-flow controller (MFC) and a pressure gauge installed in the main chamber. For each cell, a computer controlled shutter is used to allow precise control of the thickness of each layer down to a single layer of atoms.

Typically, a-plane sapphire substrates were used and the cleaning procedures are as follows: they were ultrasonically cleaned with acetone, methanol, and deionized (DI) water in sequence for 5 minutes; and then were degreased in piranha (the mixture of H_2SO_4 and H_2O_2) for 10 minutes; were finally rinsed in DI water for 3 minutes and then were dried by nitrogen.

3.2 Oxygen effects on the properties of GZO

GZO layers were grown on a-plane sapphire substrates by MBE as shown in Figure 3.1. First, a ~10-nm-thick ZnO buffer layer was grown at a substrate temperature of 300°C to provide better nucleation. Then, GZO films with thickness varying in the range from 100 nm to 750 nm were deposited at a substrate temperature of 400°C. During the growth, the temperatures of Ga and Zn cells were kept constant, 600°C and 350°C, respectively. An RF plasma source operated at 400 W acted as a source of reactive oxygen. The flux of reactive oxygen was controlled by supplying O_2 through a mass-flow controller, and different mass flow rates resulted in different oxygen pressures in the growth chamber during growth. Three series of GZO films were grown under three different oxygen pressures P_{O2} = 4.5×10^{-6}, 8.0×10^{-6}, and 1.5×10^{-5} Torr, corresponding to metal (Zn+Ga) rich (reactive oxygen to incorporated Zn ratio < 1:1), intermediate or near stoichiometric (reactive oxygen to incorporated Zn ratio ≈ 1:1), and oxygen-rich (reactive oxygen to incorporated Zn ratio > 1:1) conditions, respectively. The reactive oxygen to incorporated Zn ratio was assessed from growth rate *vs.* oxygen pressure dependence. The corresponding growth rates were ~2.1 nm/min for the near-stoichiometric and oxygen-rich conditions and ~1.7 nm/min for the metal-rich conditions. Rapid thermal annealing (RTA) at a temperature of ~650 °C in N_2 atmosphere for 3 mins was performed to activate Ga donors and increase conductivity of the GZO films.

Surface morphology and crystal quality of the GZO films were characterized by RHEED, XRD, and TEM. Electrical properties were studied by Hall effect measurement using the van der Pauw configuration, and optical properties were investigated by photoluminescence (PL) and transmittance measurements. For transmittance measurements, after the spectrum of the light from a tungsten lamp passing through the sample was measured, the GZO film was completely etched away using a 10% aqueous HCl solution and the measurement was repeated under exactly the same experimental conditions and on the same region of the sample to obtain the reference transmission through the substrate.

Figure 3.2 shows the typical RHEED patterns of (a) a-plane sapphire, (b) LT ZnO before annealing, and (c) LT ZnO after annealing and before GZO growth recorded along the ZnO [11-20] azimuth. The streaky lines in (c) indicate the flat ZnO buffer surface which is desired for the following GZO growth.

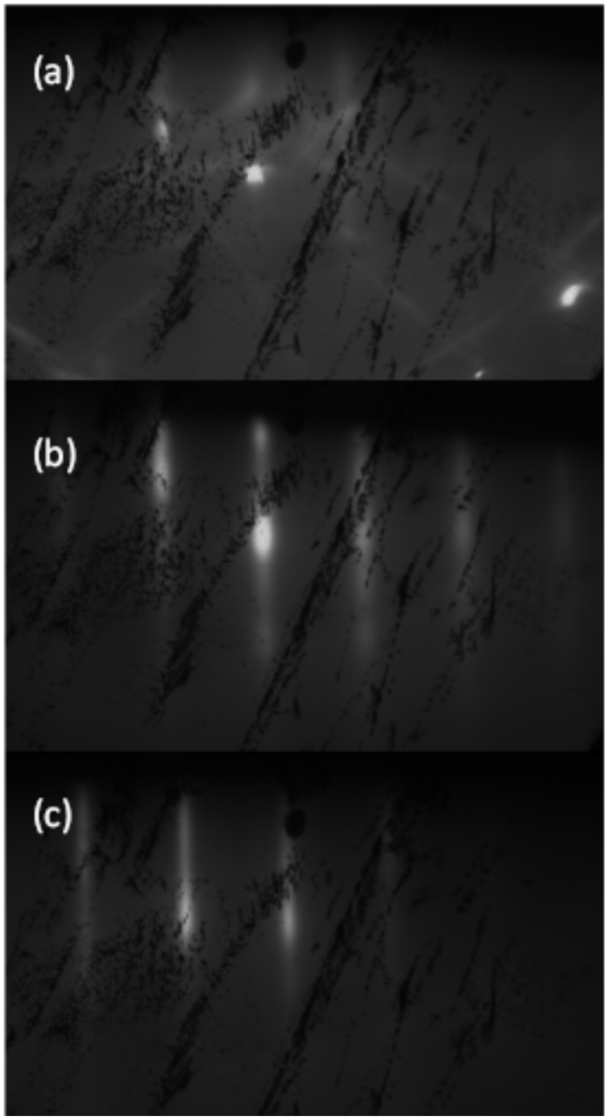

Figure 3.2 Typical RHEED patterns of (a) a-plane sapphire, (b) LT ZnO before annealing, and (c) LT ZnO after annealing and before GZO growth recorded along the ZnO [11-20] azimuth.

3.2.1 Oxygen effects on structural properties of GZO

In situ monitoring of RHEED patterns during the growth of GZO films revealed a strong effect of oxygen pressure on the growth mode. For the films grown under the metal-rich conditions, streaky RHEED patterns were observed throughout the growth, indicating two-dimensional (2D) growth mode [Figure 3.3 (a)]. The films grown under the stoichiometric conditions showed a gradual change from streaky RHEED patterns in the beginning of deposition to spotty ones, characteristic of three-dimensional (3D) growth [Figure 3.3 (b)], as film thickness reached ~100 nm. For the layers grown under the oxygen-rich conditions, the RHEED pattern transformed into a spotty one after growing the first 10-15 nm of GZO, and short arcs superimposed on the spotty diffraction became visible in the RHEED pattern recorded from the 300-nm-thick film, which indicates the presence of polycrystalline material at the film surface [Figure 3.3 (c)]. Further increase in P_{O2} resulted in polycrystalline layers.

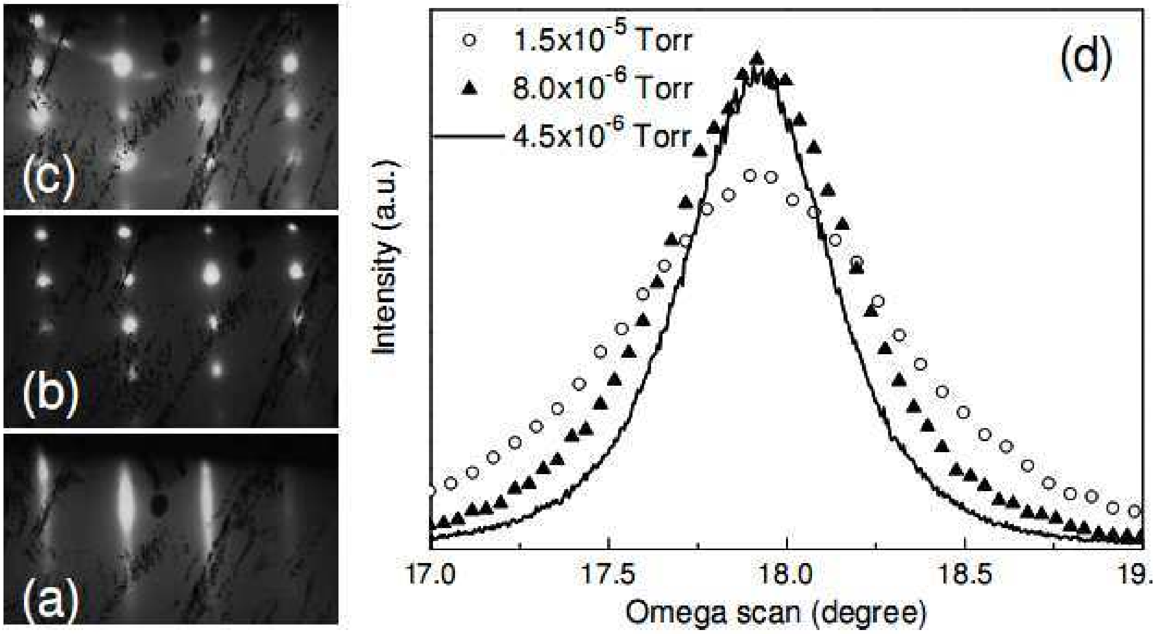

Figure 3.3 Typical RHEED patterns recorded for the [11-20] azimuth of GZO films grown at P_{O2} = (a) 4.5×10^{-6} (630-nm film), (b) 8.0×10^{-6} (300-nm film), (c) 1.5×10^{-5} Torr (300-nm film), respectively and (d) rocking curves of (0002) XRD reflection measured from GZO films grown at different P_{O2} with comparable film thickness of 300 nm.

The effect of oxygen pressure on the crystal perfection of the GZO films was revealed by XRD: the full width at half maximum (FWHM) of the (0002) rocking curves measured for the ~300-nm films grown at P_{O2} = 1.5×10^{-5}, 8.0×10^{-6}, and 4.5×10^{-6} Torr are 0.907°, 0.623°, and 0.488°, respectively [Figure 3.3 (d)]. Thus, the films grown under the metal-rich conditions exhibit better crystal quality in terms of FWHM.

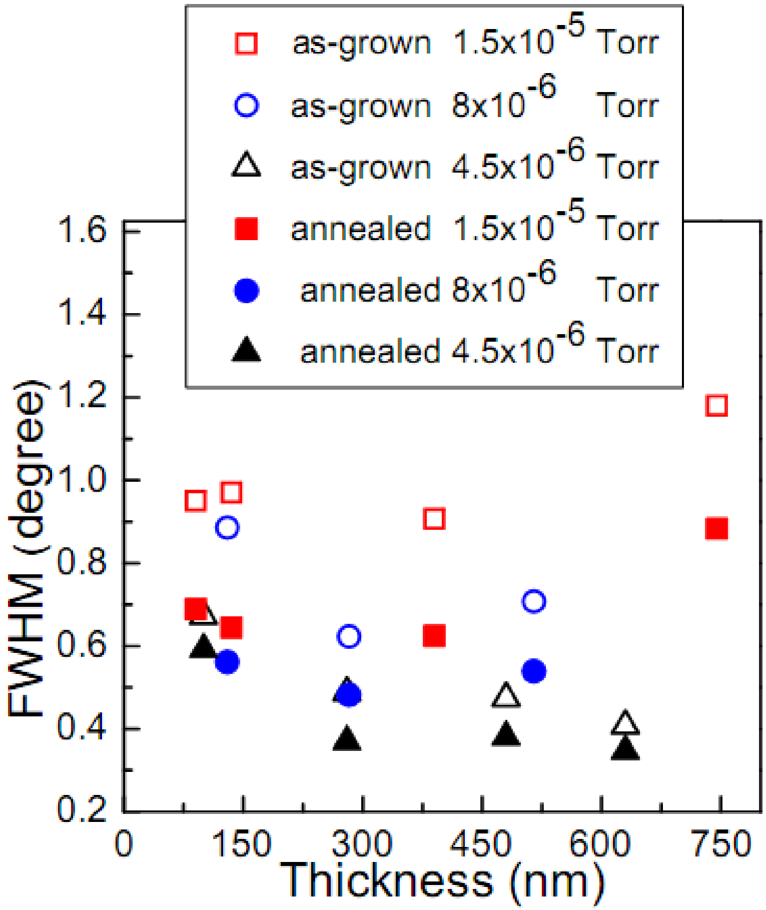

Figure 3.4 FWHM of (0002) XRD rocking curves measured for GZO layers grown at different P_{O2} (4.5×10^{-6}, 8.0×10^{-6}, 1.5×10^{-5} Torr, respectively) as a function of film thickness. Open symbols are for as-grown films, and filled symbols are for annealed films.

Figure 3.4 shows the variation in FWHM of the (0002) XRD rocking curve as a function of layer thickness for the as-grown and annealed samples deposited at different P_{O2}. Note that the optimum rapid thermal annealing (RTA) conditions are ~600°C in nitrogen environment for 3 mins in terms of resistivity. In general, the films grown under the metal-rich conditions show narrower XRD lines than their counterparts deposited under the near-stoichiometric and oxygen-rich conditions, indicating the improving crystallinity with reducing P_{O2}. The crystal quality of the as-grown GZO films prepared at $P_{O2} = 4.5\times10^{-6}$ Torr improved further with film thickness increasing from 100 nm to 630 nm, as evidenced from the gradual decrease of the rocking-curve

FWHM from 0.67° to 0.41°. To the contrary, for the films grown at higher P_{O2}, the rocking-curve FWHM first decreases with increasing layer thickness and then increases as the film thickness exceeds 300-400 nm, in agreement with the RHEED data, suggesting increasing disorder in these films as the growth progresses [Figure 3.3 (b)-(c)]. The XRD rocking-curve widths for all the GZO samples decreased upon RTA, insignificantly for the layers grown under the metal-rich conditions and substantially for the films deposited under the near-stoichiometric and oxygen-rich conditions. Nevertheless, as seen from Figure 3.4, the crystal quality of the annealed and even the as-grown layers deposited under the metal-rich conditions is superior to that of the annealed samples prepared at higher P_{O2}.

The effect of oxygen pressure on the crystal perfection of the GZO films was confirmed by TEM. Figure 3.5 compares cross-sectional TEM images of the samples grown under different oxygen pressures. One can see that the layer deposited under the metal-rich conditions [Figure 3.5 (a)] is grown epitaxially with a columnar structure composed by slightly misoriented domains (smaller than 0.5º). Selective area diffraction (SAD) reveals very strong epitaxial relationship between the sapphire substrate and the GZO layer. Predominant extended defects in this film are dislocations, which concentration decreases drastically from interface to the surface of the structure, since most of the dislocations recombine near the interface and do not penetrate further than 100 nm in depth of the GZO layer. The film grown under the oxygen-rich conditions has a textured structure [Figure 3.5 (b)], as evidenced by moiré pictures observed in the vicinity of the interface. High-angle boundaries are predominant extended defects in this film. SAD confirms this observation and reveals the arc structure typical for textured materials.

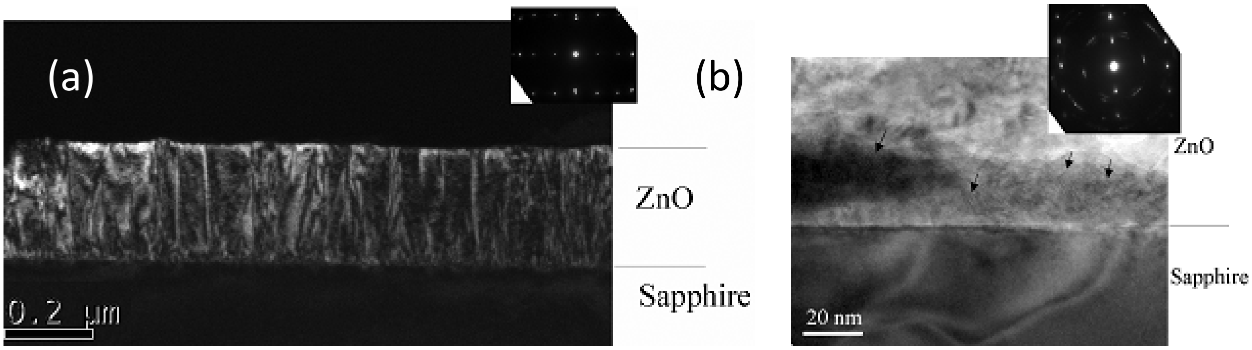

Figure 3.5 Cross-sectional dark-field TEM image of the GZO films grown under (a) metal-rich (P_{O2}=4.5×10^{-6} Torr) and (b) oxygen-rich (P_{O2}=1.5×10^{-5} Torr) conditions. Arrows indicate positions of moiré contrast due to overlapping of small grains with different orientation.

3.2.2 Oxygen effects on electrical properties of GZO

Electrical properties of the films were studied by the Hall-effect method in the van der Pauw configuration. The as-grown films deposited under the oxygen-rich conditions showed very high sheet resistance, R_S, typically in the kΩ/□ range, whereas the sheet resistance of the layers deposited under the near-stoichiometric reduces to values of about 100 Ω/□. The as-grown films deposited under the metal-rich conditions had the lowest values of the sheet resistance, ranging from 4.6 to 30 Ω/□, depending on film thickness [see Figure 3.6 (a)]. Upon annealing, the sheet resistance of the layers grown at higher P_{O2} (1.5×10^{-5} and 8.0×10^{-6} Torr) reduced drastically, down to values varying from ~20 Ω/□ to several Ω/□ depending on film thickness [see Figure 3.6 (a)]. In contrast, RTA had virtually no effect on the electrical properties of the GZO films grown under the metal-rich conditions which remained very conductive.

Figure 3.6 compares the electrical parameters of the as-grown films deposited at P_{O2} = 4.5×10^{-6} Torr with those measured on the annealed layers grown at P_{O2} = 8 ×10^{-6} and 1.5 ×10^{-5} Torr.

Figure 3.6 (b) shows resistivity, ρ, of the GZO films deduced from the measured values of

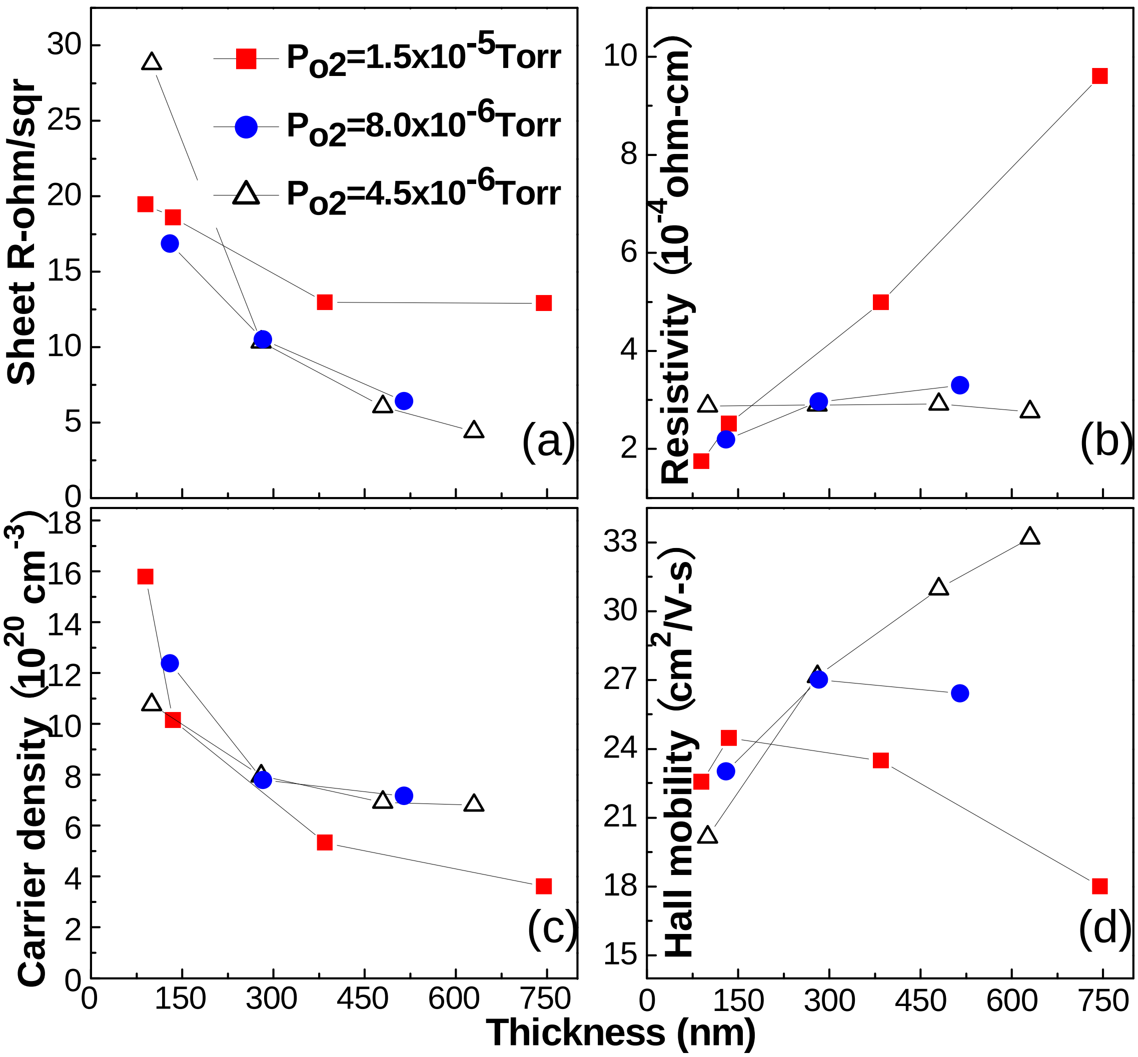

Figure 3.6 Thickness dependences of electrical properties of GZO films grown under different oxygen pressures: (squares) annealed films grown under oxygen-rich conditions (1.5×10^{-5} Torr), (circles) annealed films grown under near-stoichiometric conditions (8.0×10^{-6} Torr), and (open triangles) as-grown films deposited under metal-rich conditions (4.5×10^{-6} Torr).

sheet resistance and film thickness, t, $\rho = R_S \times t$. One can see that ρ of the films grown under the oxygen-rich conditions rises substantially as the film thickness increases, ρ of the layers grown under the near-stoichiometric conditions increases only slightly with the film thickness, while ρ of the films grown under the metal-rich conditions shows virtually no thickness dependence. The lack of thickness dependence in ρ of the films grown under the metal-rich conditions is consistent with the RHEED observation of 2D growth mode through the deposition of whole film with different thicknesses. In contrast, for GZO films grown under higher P_{O2}, RHEED changed either slowly (8 ×10^{-6} Torr) or immediately (1.5 ×10^{-5} Torr) from 2D growth mode to 3D growth mode as discussed earlier, which both indicate the worse crystal quality with the increased film thickness and consequently a film with a non-uniform resistivity is possible. Meanwhile, for a thicker film, the RTA annealing could be insufficient through the whole film thickness and result in a non-uniform resistivity as Look et al.[98] found.

Figure 3.6 (c) shows the average electron concentration calculated using the measured sheet carrier density and the film thickness under the assumption of uniform dopant distribution in the growth direction. The carrier density in the layers grown under oxygen-rich conditions drops drastically with increasing film thickness. Even the films grown at low P_{O2} = 4.5×10^{-6} Torr show a decrease in the average carrier concentration with increasing film thickness. The phenomena could be explained as the followings. Figure 3.7 shows the results of secondary ion mass spectrometry (SIMS) for undoped ZnO grown at near stoichiometric condition, and GZOs grown under metal-rich and oxygen-rich conditions, respectively. The Al concentrations near the interfaces in the three cases above-mentioned are high. The high Al concentration near the interface between a-plane sapphire and ZnO is caused mainly by Al out-diffusion from the substrate while it is not clear why the Al concentration is high near the other interface. Anyway, the thinner the GZO layer is, the stronger the effect of Al due to out-diffusion on the average electron concentration measured in Hall method since Al and Ga are the same as dopants in ZnO. Here it must be pointed out the above-mentioned conclusions assumed the reliability of SIMS results but they may not, which need further studies since the SIMS results themselves are difficult to understand. The other thing is that TEM revealed the thinner GZO layers are more defective due to the ZnO/a-sapphire interface which could result in higher electron

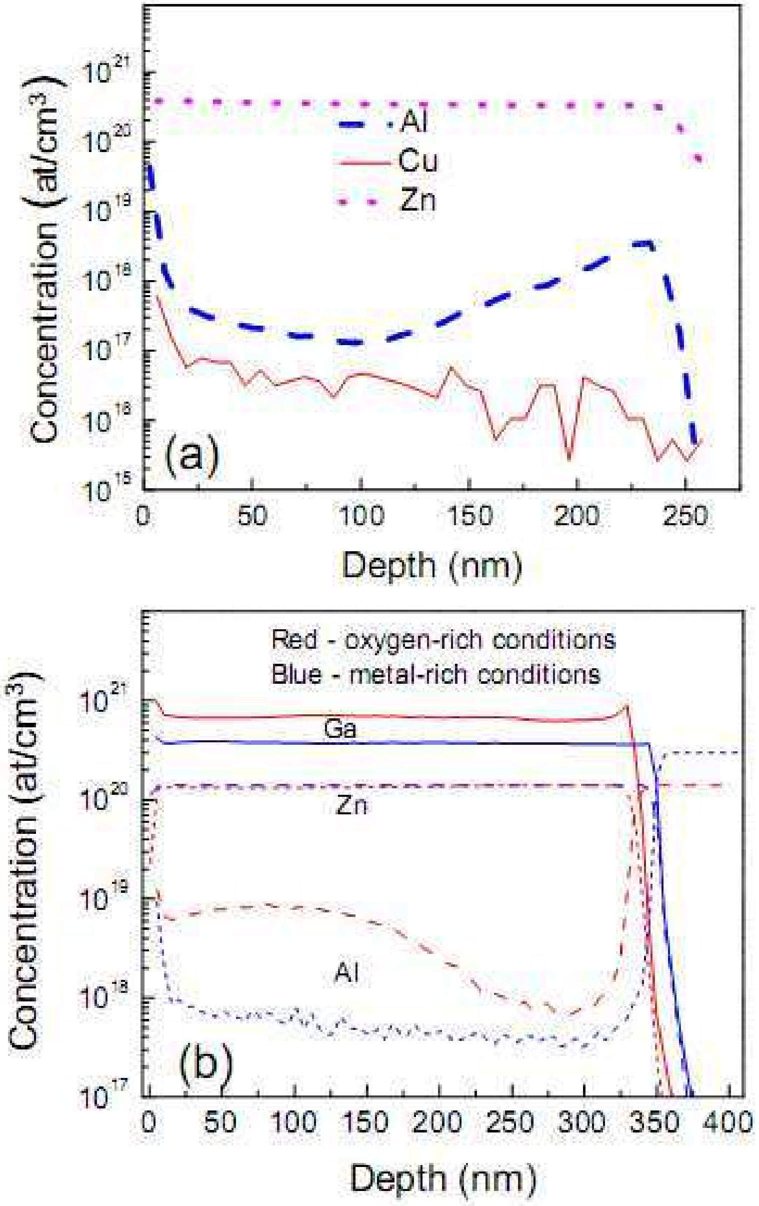

Figure 3.7 SIMS results of (a) nominally undoped ZnO on *a*-plane sapphire grown at near stoichiometric condition (8.0×10^{-6} Torr) and (b) GZO on *a*-plane sapphire grown at metal-rich (blue color) (4.5×10^{-6} Torr) and oxygen-rich (red color) (1.5×10^{-5} Torr) conditions.

concentrations for GZO layers with thicknesses around 100 nm. One more thing is the GZO thickness measurement error which is typically thought to be within ~25 nm. The big error of 25 nm compared with a thin layer of 100 nm for GZO will cause the calculated electron concentration for thin layers to significantly deviate from the real electron concentration while it will not for a thick GZO layer. The slightly different average concentrations for GZO layers with comparable thicknesses but grown under either metal-rich conditions or oxygen-rich conditions could origin from the different P_{O2} during growth.

Electron mobility in the GZO layers grown under metal-rich conditions increases with film thickness [Figure 3.6 (d)] in agreement with the improved crystal quality deduced from the XRD data and the reduced average electron concentration measured from Hall method. The former one indicates the reduced effect on mobility from grain boundary scattering and the latter one indicates the reduced effect on mobility from ionized impurity scattering. In the layers grown at higher P_{O2}, the mobility first increases and then decreases as the thickness increases, which is also consistent with the behavior of the XRD rocking curves exhibiting first a decrease and then an increase of the FWHM [compare Figure 3.4 and Figure 3.6 (d)]. Detailed studies regarding the electron transport in GZO layers will be carry out soon.

3.2.3 Oxygen effects on optical properties of GZO

The transmittance spectra from the as-grown and annealed samples grown at different P_{O2} but having comparable thickness are shown in Figure 3.8. Transmittance below the ZnO band gap was close to 90% in all the studied samples, whereas the position of the transmission was sample-dependent. The highest transmittance (more than 95% above 385 nm) was observed for the annealed sample grown under metal-rich conditions [see Figure 3.8 (b)]. Figure 3.9 shows a real GZO sample grown by MBE under metal-rich conditions on double-sides polished sapphire substrate for transparency illustration. The background is a piece of white paper with letters. As you can see the GZO is very transparent although it has some light pink color, which is highly desired for transparent electrode applications.

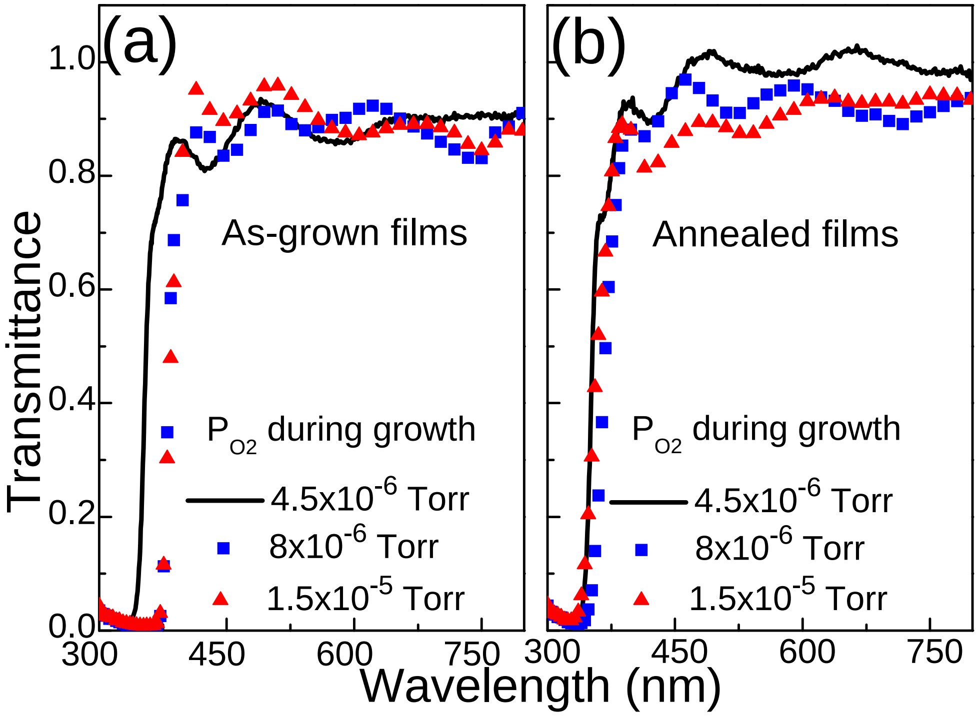

Figure 3.8 Transmittance of (a) as-grown and (b) annealed GZO grown at different oxygen pressures (Note that transmittance higher then 100% is an measurement artifact due to the Fabri-Perrot interference)

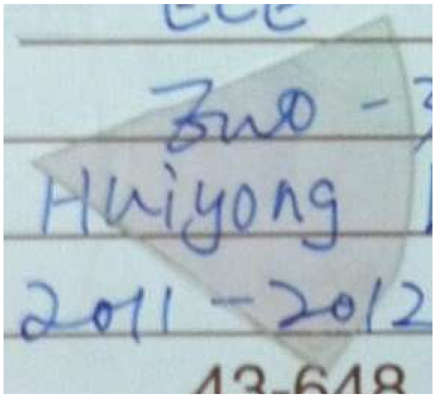

Figure 3.9 A representative of GZO layers (~300 nm thick) grown by MBE under metal-rich conditions on double-sides polished sapphire substrates for transparency illustration. Note the background is a piece of white paper.

The GZO samples grown under the metal-rich conditions demonstrated a strong blue shift of transmission edge, both in the as-grown and annealed samples, which is attributed to the Burstein-Moss shift of the Fermi level deep into the conduction band. This finding is in agreement with the electrical measurements, revealing the high conductivity of these samples. According to the electrical data, the layers grown under oxygen-rich conditions became highly conductive only upon RTA, and supportive of these results the transmission edge shifted significantly to shorter wavelengths after RTA [see Figure 3.8].

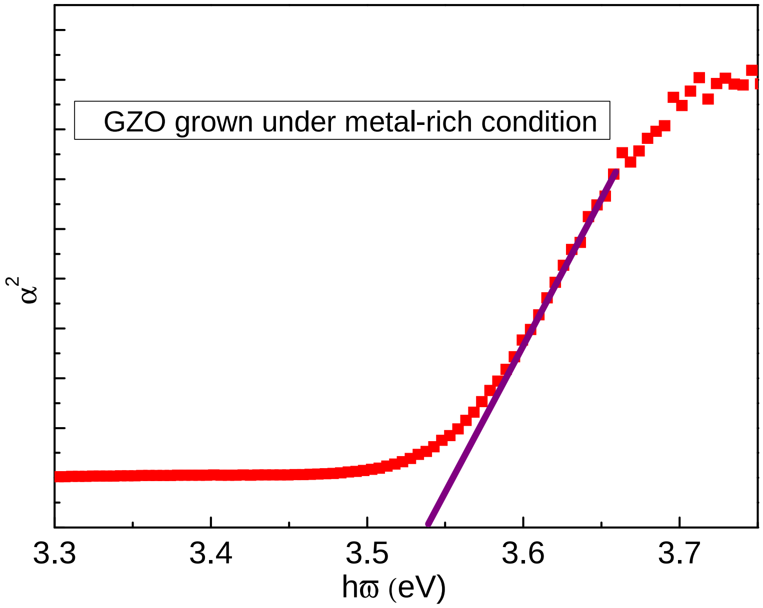

Figure 3.10 Estimated optical band gap of the as-grown GZO layer grown under metal-rich conditions (4.5×10^{-6} Torr) using Tauc's plot method.

The optical band gap of the as-grown GZO grown under metal-rich conditions was estimated using Tauc's plot by plotting $(\alpha h\nu)^2$ versus hn (photon energy) and extrapolating the straight line portion near the onset of the absorption edge onto the energy axis.[99] As shown in Figure 3.10, its optical band gap was estimated to be 3.54 eV which is 0.27 eV larger than that of the ZnO control (3.27eV) grown by our MBE system, corresponding to a strong blue shift.

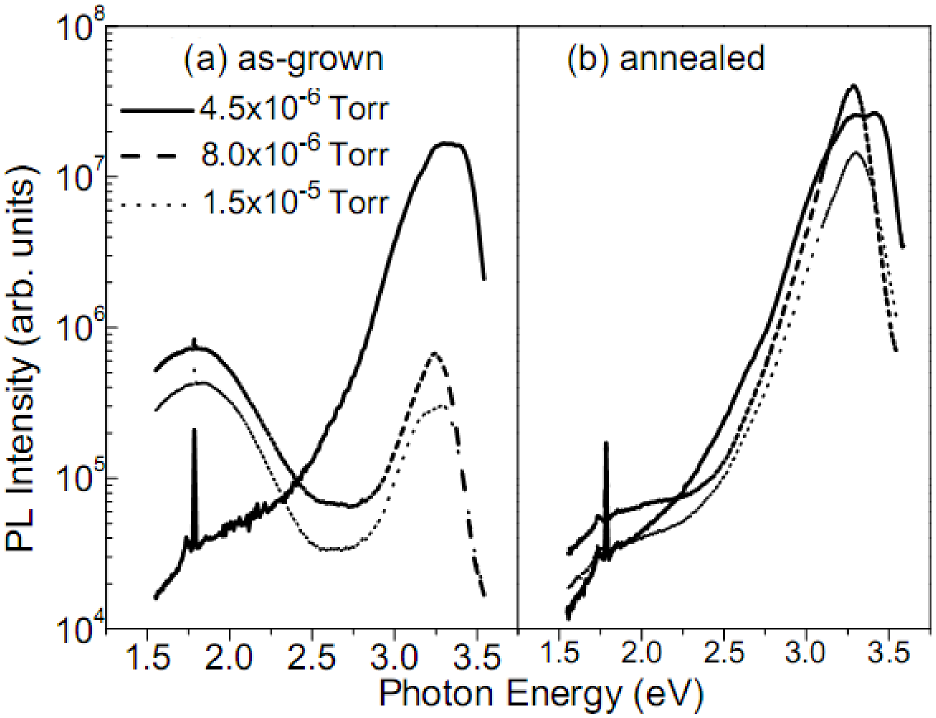

Figure 3.11 PL of as-grown (a) and annealed (b) GZO films grown under different oxygen pressures.

PL spectra of GZO films measured at room temperature before and after annealing are presented in Figure 3.11 (a) and (b), respectively. In both cases, the PL spectra from the film grown under metal-rich conditions (P_{O2}=4.5×10^{-6} Torr) exhibits only strong near band edge (NBE) emission, broadened and shifted to higher energies (maximum at 3.35-3.4 eV), that agrees with the Fermi level position well above the conduction band minimum. To the contrary, the PL spectra of the as-grown GZO films deposited at P_{O2}=8.0×10^{-6} and 1.5×10^{-5} Torr show only weak NBE emission and a strong, broad defect-related emission around 1.75 eV. The nature of the defect-related band needs further studies. After annealing of these two samples, the intensity of the defect-related emission decreases, while the intensity of the NBE emission increases by a factor of ~30 and the peak maximum shifts significantly to shorter wavelengths, indicating improvement of the crystal quality and increase in concentration of free electrons, in a good agreement with the electrical and XRD data. Nevertheless, the NBE line from the sample grown under metal-rich conditions shows the strongest blue shift, indicating higher concentration of free carriers.

In short, P_{O2} has strong effects on the structural, electrical and optical properties of GZO films. To achieve higher conductivity and higher transmittance, metal-rich conditions (reactive oxygen to incorporated Zn ratio<1) instead of oxygen-rich conditions (reactive oxygen to incorporated Zn ratio>1) are required.

3.2.4 Proposed complex defects in GZO layers grown under oxygen-rich conditions

To understand why the GZO layer grown under oxygen-rich conditions exhibited a much higher resistivity, RTA annealing in nitrogen environment were carried out for a GZO layer grown under oxygen-rich conditions (P_{O2}= 1.5×10^{-5} Torr), which is about 740 nm thick. As shown in Figure 3.12 (c), upon the RTA treatment in the temperature range from 400 to 650 ◦C, the resistivity of samples reduced from $\sim4.5\times10^{-2}$ to $\sim5.7\times10^{-4}\Omega\cdot$cm. Compared with the as-grown GZO films grown under oxygen-rich conditions (n $\sim2\times10^{19}$ cm^{-3}, μ ~6 cm^{2}/V·s), the significant improvement in resistivity after RTA annealing is due to the increase in both the electron concentration and the mobility. The increase in both electron concentration and mobility for a GZO layer grown under oxygen-rich conditions could be caused by the reduction in compensation of the free electrons with some acceptors as pointed out by Look et al.[98]. As seen from Figure 3.12 (a), when annealing temperature increased from 400 to550˚C, the electron concentration increased with annealing temperature while the corresponding mobility varied around 20 cm^{2}/V·s. Consequently, in this temperature range (region 1) the reduction in resistivity is mainly due to the increase in electron concentration. When annealing temperature further increased from 550 to 650 ◦C (region 2), the electron concentration gradually decreased which could be due to the decrease in structural quality of the material. The increase in electron concentration in region 1 is likely related to the dissociation of some acceptor-like complex defects. As seen from Figure 3.13, the temperature-dependent electron concentrations of these annealed GZO samples in region 1 follows the Arrhenius law and the binding energy of defect complexes was found to be ~0.57 ± 0.2eV.

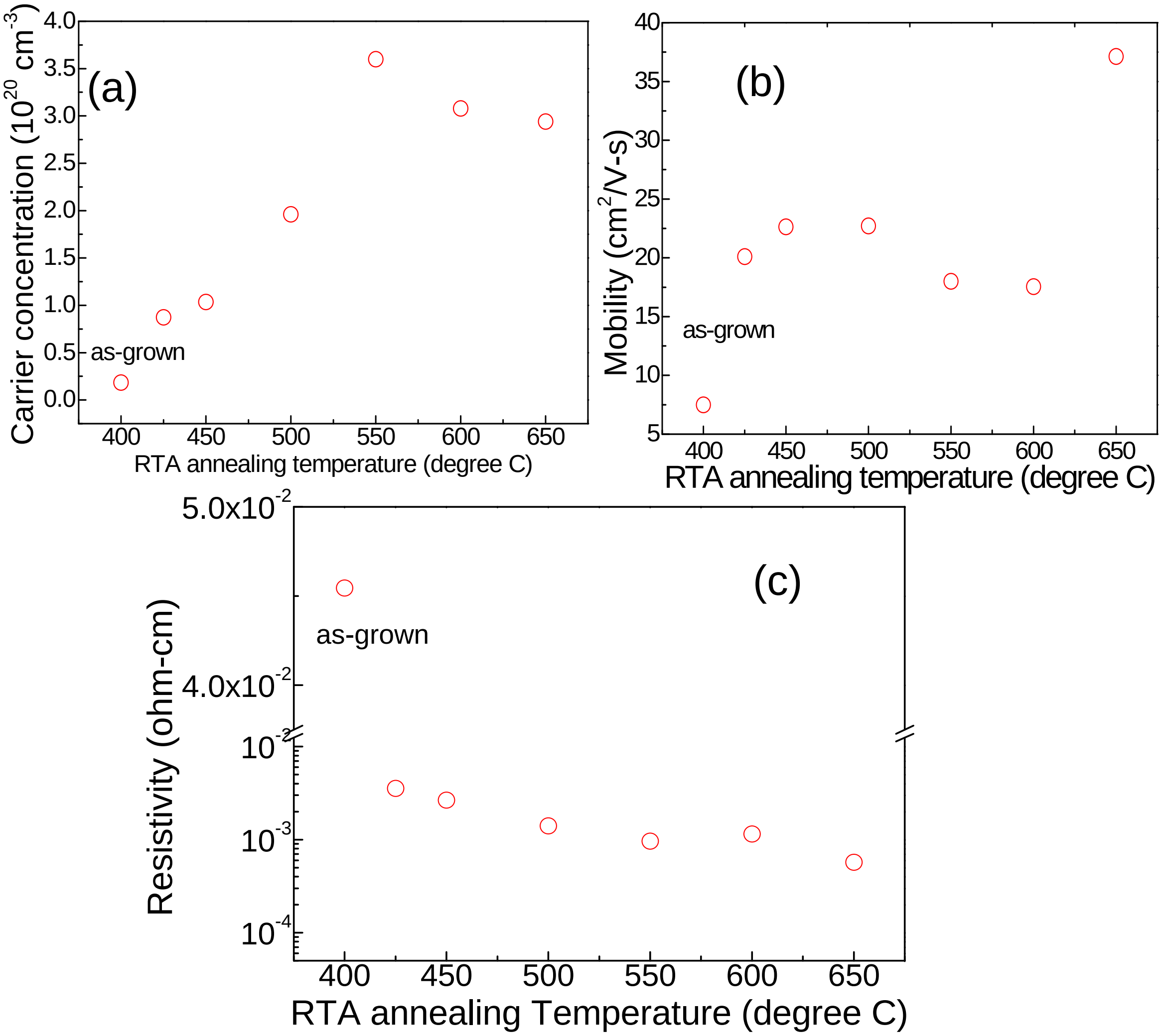

Figure 3.12 RTA annealing temperature effects in nitrogen environment on (a) carrier concentration, (b) mobility, and (c) resistivity of a 740 nm GZO layer grown under oxygen-rich conditions (P_{O2}= 1.5×10^{-5} Torr).

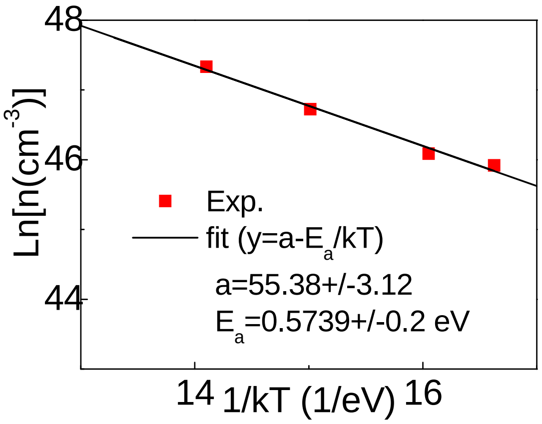

Figure 3.13 Determination of binding energy for GZO sample grown under O-rich condition based on temperature-dependent carrier concentrations.

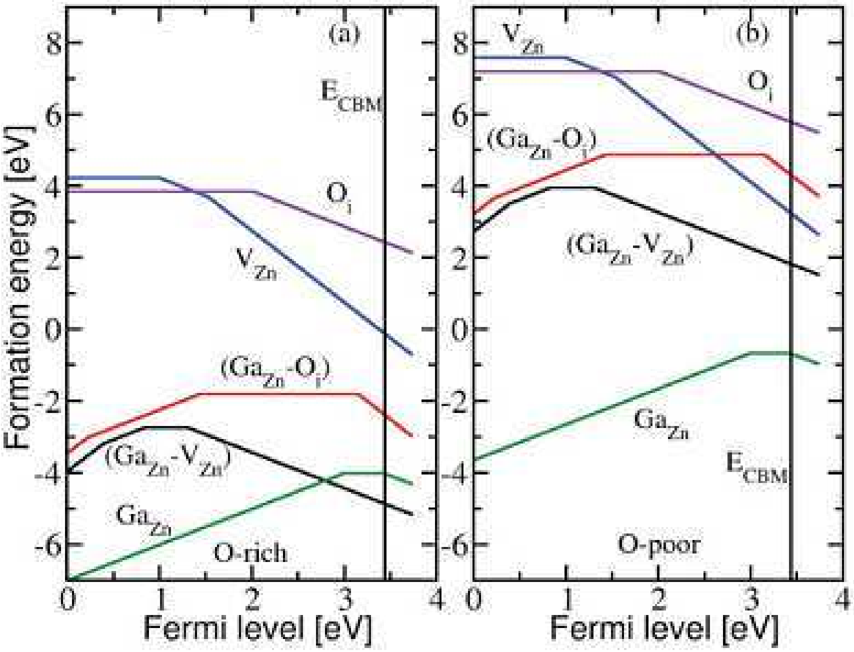

Figure 3.14 Formation energies of defects as a function of the location of Fermi energy (origin is set at the VBM) in (a) oxygen rich and (b) oxygen poor environment. Positive (negative) slope corresponds to positive (negative) defect charge state. The ends of the formation energy lines correspond to the experimental E_F of Ga heavily doped ZnO, 0.3eV above the CBM (vertical line). [100]

Using hybrid functional theory, the defect complexes in GZO layers grown under oxygen-rich conditions were determined to be mainly (Ga_{Zn}-V_{Zn}) acceptor complexes.[100] As seen from

Figure 3.14 (a), the formation energy of (Ga_{Zn}-V_{Zn}) acceptor complexes decreases with increasing electron concentration in GZO grown under oxygen-rich growth conditions and becomes lower than that of the Ga_{zn} donors in the degenerate material (at $n>5\times10^{18}$ cm^{-3}). Consequently GZO films grown under oxygen-rich conditions as shown in Figure 3.13 have lower mobility partially due to higher compensation induced by (Ga_{Zn}-V_{Zn}) acceptor complexes.

Based on the hybrid functional theory, the binding energy of a (Ga_{Zn}-V_{Zn}) acceptor complex was estimated as the formation energy difference of a (Ga_{Zn}-V_{Zn}) complex and its constituents (Ga_{Zn} and V_{Zn}). As in the case of the GZO grown under oxygen-rich conditions with n ~2×10^{19} cm^{-3} [Figure 3.12], placing the Fermi level approximately at 0.1 eV below the conduction band minimum (CBM), the binding energy of a (Ga_{Zn}-V_{Zn}) acceptor complex is about 0.75 eV, which is very close to the one calculated from the experiments (0.57 eV). Therefore, the theoretical calculation should be reliable. While for GZO layers growth under metal-rich growth conditions [see Figure 3.14 (b)], the Ga_{zn} donors have the lowest formation energy within a wide range of electron concentrations including the highly degenerate material. Thus, a low compensation level is expected in GZO layers grown under metal-rich conditions.

In short, to achieve highly conductive GZO compensation must be minimized, which will significantly increase both electron concentration and mobility. Again, to minimize the compensation caused by (Ga_{Zn}-V_{Zn}) acceptor complexes, metal-rich conditions instead of oxygen-rich conditions for growth are needed.

3.3 Ga flux effects on the properties of GZO

Ga flux was varied by changing Ga cell temperature (T_{Ga}) from 400 to 650^{o}C to investigate the Ga flux effects on the properties of GZO layers grown on a-plane sapphire substrate by MBE. During depositions for this group of GZO samples, oxygen pressure, plasma power, Zn cell temperature, and substrate temperature were kept at 4.5×10^{-6} Torr (metal-rich conditions), 400 W, 350°C, and 400°C, respectively. Again, a ~10-nm-thick ZnO buffer layer was grown at a substrate temperature of 300°C to provide better nucleation. The following GZO layer thicknesses are ~300 nm.

Figure 3.15 (a) shows a representative RHEED pattern of undoped ZnO grown under the optimal condition (P_{O2}=9×10^{-6} Torr), which streaky RHEED pattern indicates 2D growth mode and high crystalline quality for this layer. While the RHEED pattern of undoped ZnO grown under the metal-rich condition (P_{O2}=4.5×10^{-6} Torr) as shown in Figure 3.15 (b) indicates that the growth mode and probably the crystalline quality did not change when P_{O2} was reduced from 9×10^{-6} Torr to 4.5×10^{-6} Torr. After Ga was introduced, the growth mode for GZO layers grown under T_{Ga}<=600^{o}C is still 2D growth mode [see Figure 3.15 (c)-(e)] while it is obvious 3D growth mode indicated by the spotty RHEED pattern [Figure 3.15 (f)] when T_{Ga} was further increased to 650^{o}C. Note that the RHEED pattern for the GZO layer grown under T_{Ga}=500^{o}C shows tendency to become 3D growth mode, which could be caused by the variation of the growth conditions during growth since the P_{O2} during growth is not stable. The transition in RHEED patterns from streaky lines to spotty dots when T_{Ga} was increased from 600 to 650^{o}C revealed that the Ga flux at T_{Ga}=600^{o}C is close to the optimal condition and further increase in Ga flux will degrade the crystal quality and produce rougher surface. One interesting phenomenon is that a RHEED pattern like the one in Figure 3.15 (d) for a GZO layer grown under metal-rich conditions along with T_{Ga}=600^{o}C could be recovered to one like in Figure 3.15 (e) with time, which means the surface becomes smoother with doping Ga.

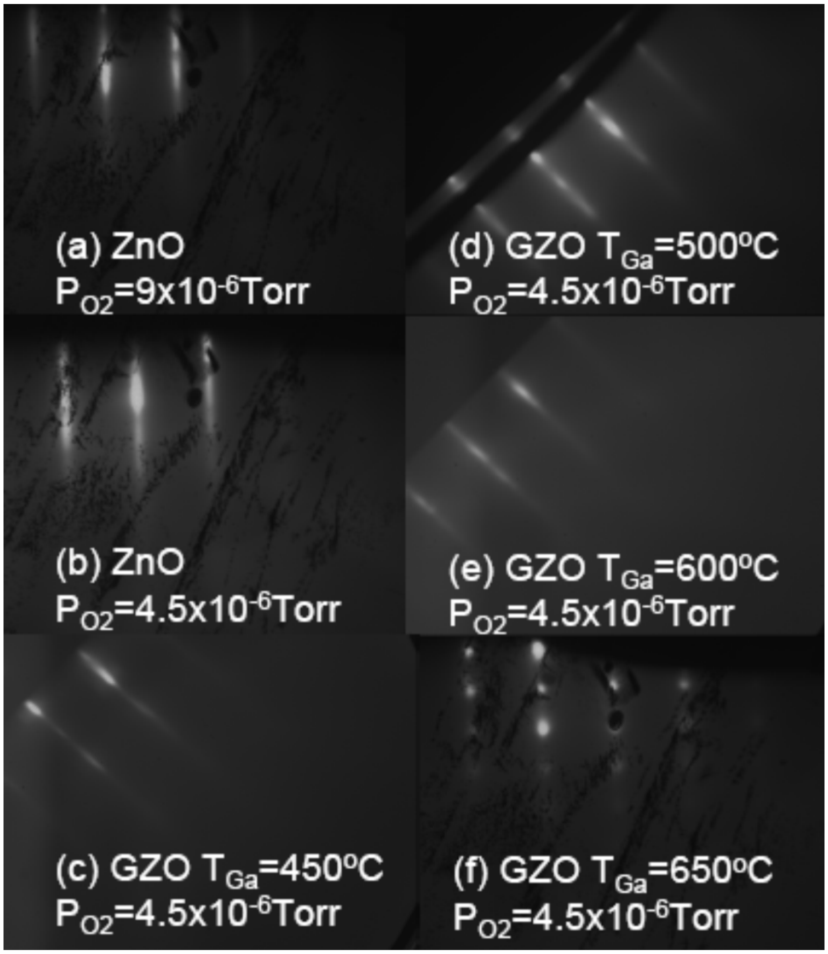

Figure 3.15 RHEED patterns recorded for the [11-20] azimuth of (a) ZnO control grown under P_{O2}=9×10^{-6} Torr (optimal condition for ZnO), (b) ZnO grown under metal-rich conditions (P_{O2}=4.5×10^{-6} Torr), (c) GZO grown under metal-rich conditions and T_{Ga}=450^{o}C, (d) GZO grown under metal-rich conditions and T_{Ga}=500^{o}C, (e) GZO grown under metal-rich conditions and T_{Ga}=600^{o}C, and (f) GZO grown under metal-rich conditions and T_{Ga}=650^{o}C, which all have a thickness ~300nm.

The similar RHEED evolutions with Ga flux discussed above were also observed by Han et al.[101] who varied Ga cell temperatures from 350 ^{o}C to 470 ^{o}C and found the Ga cell temperature of 440 ^{o}C is the highest cell temperature to achieve highly epitaxial single crystalline a-plane ZnO grown on r-plane sapphire substrates by MBE [Figure 3.15 vs. Figure 3.16]. As illustrated in Figure 3.16 (f), when Ga cell temperature was increased to 470 ^{o}C the layers showed strong polycrystalline features. Han et al.[101] also claimed that the surfaces of Ga doped ZnO achieved at Ga cell temperatures below 440 ^{o}C are smoother than the undoped ZnO revealed by both RHEED and AFM. According to Han et al.[101] AFM revealed that the root-mean-square surface roughness of the undoped ZnO is about 2.2 nm while those of Ga-doped ZnO are between about 1.7 and 0.7 nm, which reduces with the increase in Ga cell temperature for T_{Ga} <440 ^{o}C.

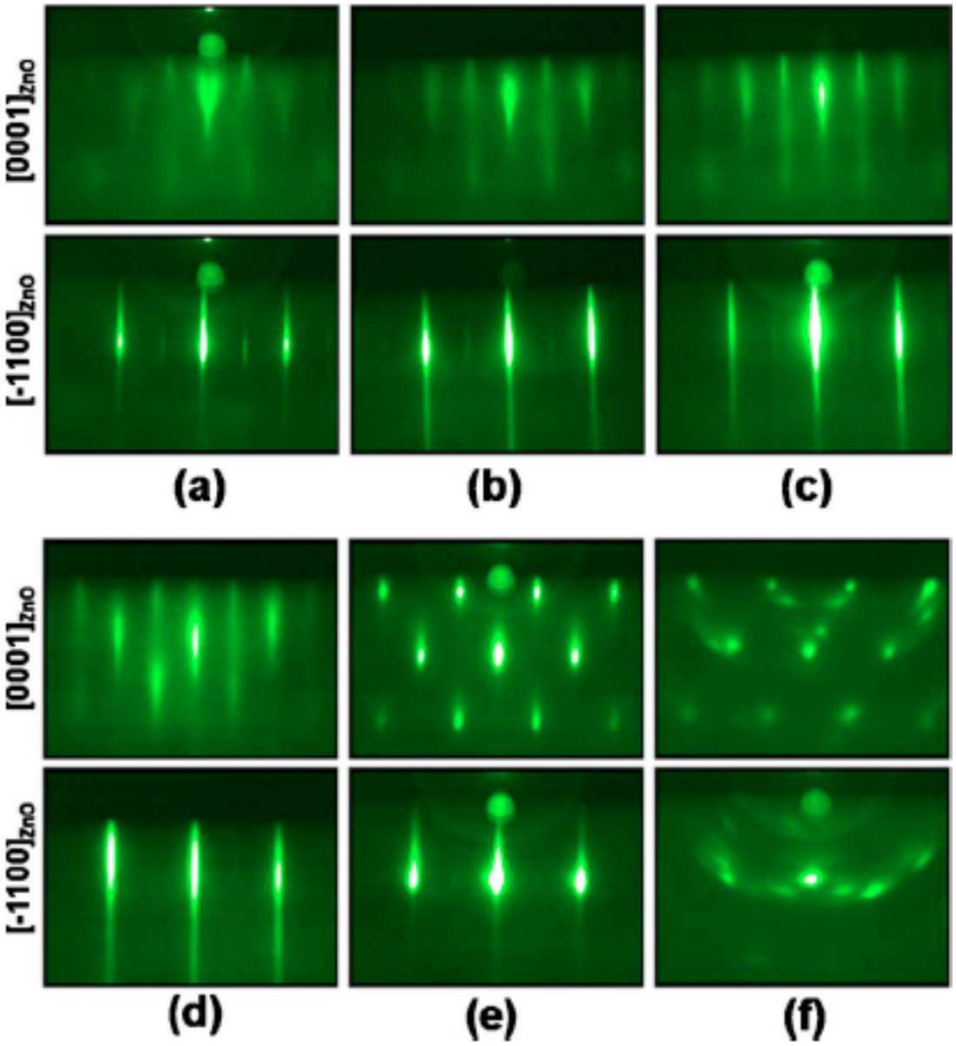

Figure 3.16 RHEED patterns from (a) undoped a-plane ZnO film and Ga-doped ZnO films grown with different Ga cell temperatures of (b) 350 ^{o}C, (c) 380 ^{o}C, (d) 410 ^{o}C, (e) 440 ^{o}C, and (f) 470 ^{o}C. (after Han et al.[101])

Figure 3.17 shows the FWHM of the (0002) XRD rocking curve verses the Ga flux by our MBE system. In general, the layers including both ZnO samples and GZO samples with good streaky RHEED patterns as shown above [Figure 3.15 (a)-(c) and (e)] exhibited relatively smaller FWHM values. The GZO layer grown under T_{Ga}=650°C shows the largest FWHM value of 0.48° while the one grown under T_{Ga}=500°C is the second largest, which are consistent with their RHEED patterns. For other GZO layers, their FWHM values are even smaller than those of the ZnO control samples.

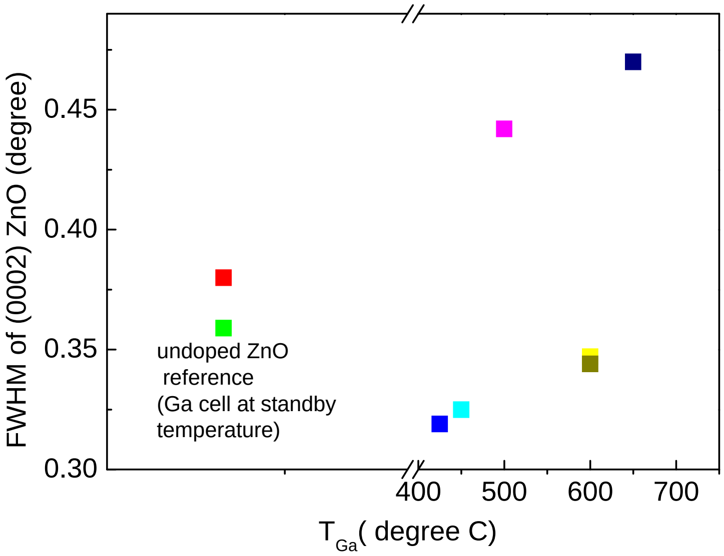

Figure 3.17 FWHM of (0002) XRD rocking curves measured for ZnO control samples grown under P_{O2}=9×10^{-6} Torr (square in green) and P_{O2}=4.5×10^{-6} Torr (square in red) and GZO layers grown under metal-rich conditions (P_{O2}=4.5×10^{-6} Torr) but different T_{Ga} varying from 425°C to 650°C.

With not taking into account the GZO layer grown under T_{Ga}=500°C, the trend for the effects of T_{Ga} on FWHM values was similar to that observed by Han et al.[101], indicating that at lower Ga flux Ga doping helps improve the crystal quality but at a Ga flux higher than some level limited by the Ga solubility in ZnO the extra Ga will degrade the crystal quality, probably due to the defective grain boundaries. The achieved smaller FWHM values of lightly doped GZO or the improvement in their crystalline quality could be explained as the relief of strain in lattice distortion. Figure 3.18 illustrates the epitaxial relationship between ZnO and a-plane sapphire substrate. It is easy to see that along ZnO [11-20] or sapphire [0001] direction the lattice mismatch is almost zero (12.99 Å~4×3.25 Å). While along the [1-100] direction of either ZnO or sapphire, the lattice mismatch is huge (5.63 Å vs. 8.22 Å) which could cause significant lattice distortion. After doping with Ga, the lattice distortion could be reduced since the radius of Ga^{3+} ion is smaller than that of Zn (0.62 Å vs. 0.74 Å). This hypothesis has to be examined carefully because the small difference in FWHM values of doped and undoped ZnO could also originate from the measurement errors.

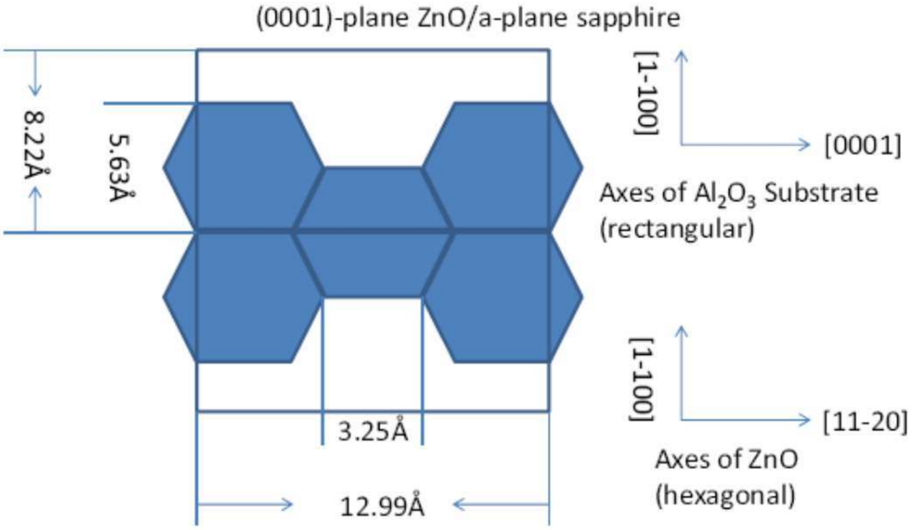

Figure 3.18 Schematic of in-plane epitaxial relationship between ZnO and a-plane sapphire substrate.

Figure 3.19 shows the electrical properties of the above-mentioned samples grown by our MBE system. As seen, the ZnO control sample grown under the optimal conditions (P_{O2}=9×10^{-6} Torr) exhibited a low electron concentration of ~1×10^{17} cm^{-3} and a high mobility of ~72 cm^2/V·s, which both are superior to those for the ZnO sample grown under metal-rich conditions in terms of defects. This observation is consistent with their FWHM values as shown in Figure 3.17. When Ga was introduced, the electron concentration for all GZO layers is much higher than those ZnO samples. When T_{Ga} was increased from 425 to 600°C, the electron concentration and mobility first increased and then virtually saturated. While when T_{Ga} was further increased to 650°C, the electron concentration kept almost unchanged but mobility reduced. The lowest resistivity achieved is at T_{Ga}=600°C, which is slightly lower than 2×10^{-4} Ω·cm, and consequently T_{Ga}=600°C is the best condition for Ga flux. The similar dependences of carrier concentration, mobility, and resistivity on Ga cell temperatures to our experimental data are also observed by Han et al.[101], where the electron concentration saturated at a lower value of ~3×10^{20} cm^{-3}.

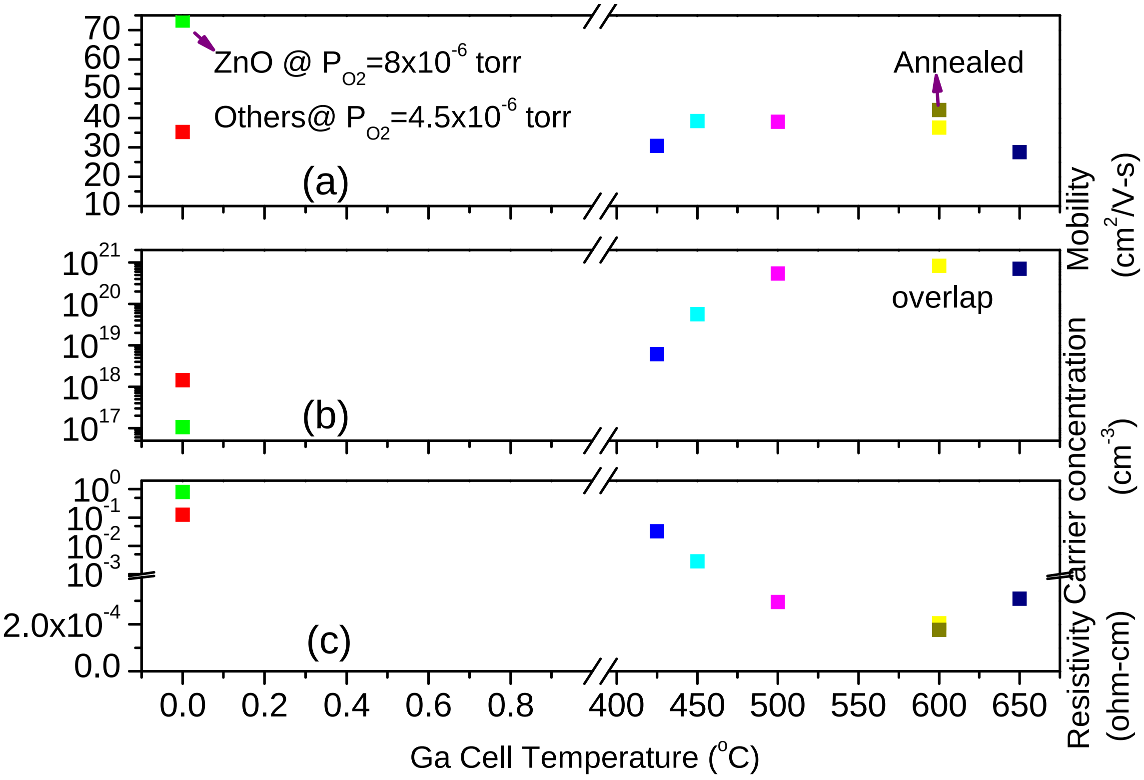

Figure 3.19 Electrical properties of ZnO control samples grown under $P_{O2}=9\times10^{-6}$ Torr (square in green) and $P_{O2}=4.5\times10^{-6}$ Torr (square in red), and GZO samples grown under metal-rich conditions ($P_{O2}=4.5\times10^{-6}$ Torr) but different T_{Ga} varying from 400°C to 650°C.

In order to get some more needed light on the effects of Ga flux, temperature-dependent Hall (TDH) measurements in the van der Pauw configuration were carried out for 3 GZO layers, which were grown under T_{Ga}=425 ^{o}C, 450 ^{o}C, and 600^{o}C, respectively. These layers have smaller FWHM values than those of the control ZnO layers and their electron concentrations are in the range of 10^{18} cm^{-3}, 10^{19} cm^{-3}, and 10^{20} cm^{-3}, respectively. As shown in Figure 3.20 (a), their electron concentrations are temperature-independent in the investigated temperature range of 15K to 330K, indicating of their degeneracy nature. Their electron concentrations are 9.2×10^{20} cm^{-3}, 5.5×10^{19} cm^{-3}, and 6×10^{18} cm^{-3}, respectively. However, their temperature-dependent mobility curves are totally different. Although their RT mobilities are comparable, the LT mobility for GZO layer grown under T_{Ga}=600^{o}C is much higher than that for GZO layer grown under T_{Ga}=450^{o}C while the latter one is much higher than that for GZO layer grown under T_{Ga}=400^{o}C. As shown in Figure 3.20 (c), the GZO layer grown under T_{Ga}=600^{o}C initially shows an increase in mobility with decreasing temperature down to ~150 K which then becomes almost invariant at low temperature (LT). As shown in Figure 3.20 (b), the GZO layer grown under T_{Ga}=600^{o}C shows metallic behavior, which means the resistivity is temperature-independent at LT while it almost linearly increases with temperature at high temperature (HT). In contrast, the GZO layer grown under T_{Ga}=425^{o}C shows semiconductor-like behavior although it is also degenerate since it exhibits a temperature-activated mobility [Figure 3.20 (c)] and a negative temperature coefficient of resistivity [Figure 3.20 (b)]. The GZO layer grown under T_{Ga}=450^{o}C is the transition one between the GZO layer grown under T_{Ga}=400^{o}C and the GZO layer grown under T_{Ga}=600^{o}C. As seen in Figure 3.20 (c), its mobility is almost temperature-independent. Its resistivity first decreases with temperature (semiconductor-like) and then increases with temperature (metallic behaviour). The scattering mechanisms controlling the electron transport in

GZO layers with different electron concentrations grown under different T_{Ga} and P_{O2} will be discussed in more details later.

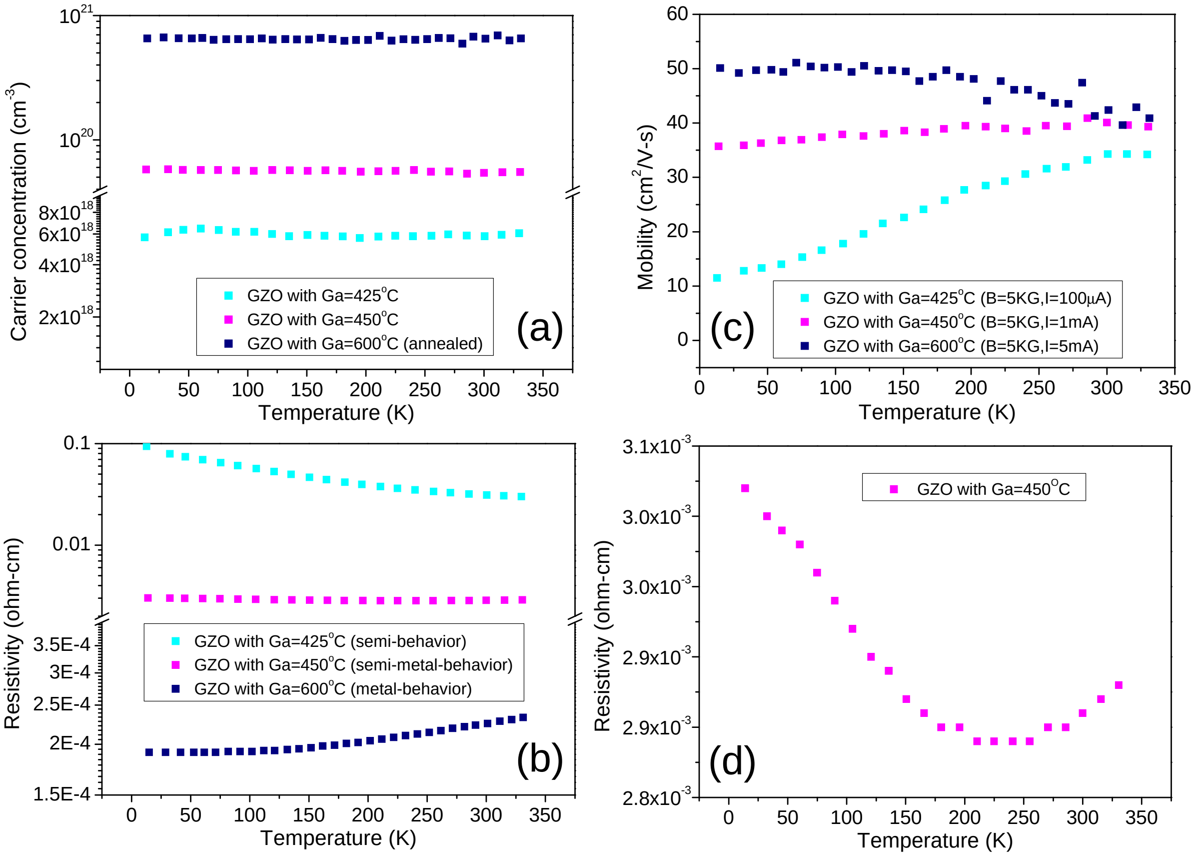

Figure 3.20 Temperature-dependent Hall measurements for selected GZO layers grown under metal-rich conditions (P_{O2}=4.5×10^{-6} Torr) but with T_{Ga}=425°C, 450°C, and 600°C, respectively. [Note: (d) is the enlarged one in (c) for T_{Ga}=450°C.]

3.4 Substrate temperature effects on GZO properties

The effects of substrate temperatures on GZO properties have been investigated on GaN substrates instead of a-sapphire substrates. This is because GZO will be applied in InGaN based LEDs as transparent electrodes later and the surface morphologies of GZO layers which could be closely related to the substrate temperatures have significant effects on light extraction from the inside to the outside of the LEDs. Therefore, it makes more sense to use GaN substrates to investigate the effects of substrate temperatures, which will provide more accurate information to achieve the best device performance.

InGaN LED structures with top p-type GaN layer grown on c-plane sapphire in a vertical low-pressure metalorganic chemical vapor deposition (MOCVD) system were used as substrates to investigate the substrate temperature effects on GZO properties. The top p-type GaN:Mg layers are about 100 nm thick, which were grown at substrate temperature of 950 ^{o}C and MOCVD chamber pressure of 200 Torr. Before loading into the MBE system for GZO growth, p-GaN templates have been activated by rapid thermal annealing in N_2 environment. Hall measurements performed after the activation on a calibration p-GaN layer indicated a hole concentration of ~7×10^{17} cm^{-3}. To prevent oxidation of the GaN surface in MBE chamber before growth, the GaN substrate has been kept under Zn flux before oxygen is allowed into the MBE chamber and plasma source is turned on.

The growth procedure and growth parameter except substrate temperature for GZO growth are the same as those for GZO growth on a-sapphire substrate under metal-rich conditions (P_{O2} = 4.5×10^{-6} Torr and T_{Ga}=600^{o}C). The substrate temperature for GZO growth was varied from 200 to 450 ^{o}C to investigate the substrate temperature effects. The film thicknesses were controlled to be 200-300 nm.

Figure 3.21 shows the effects of substrate temperatures on electrical properties of as-grown GZO layers grown on LED structures under oxygen pressure of ~4×10^{-6} Torr. As seen from Figure 3.21 (a), carrier concentration varied from ~9×10^{20} to ~4×10^{20} cm^{-3} and in general decreases with increasing substrate temperature, mobility increases from ~ 25 cm^2/V·s to ~ 57 cm^2/V·s with the increasing of substrate temperature. The substrate temperature has only a moderate effect on the resistivities of GZO layers. The optimum trade-off between carrier density and mobility resulting in a resistivity as low as ~2.3×10^{-4} Ω·cm has been achieved for the GZO films grown at substrate temperature of 350°C.

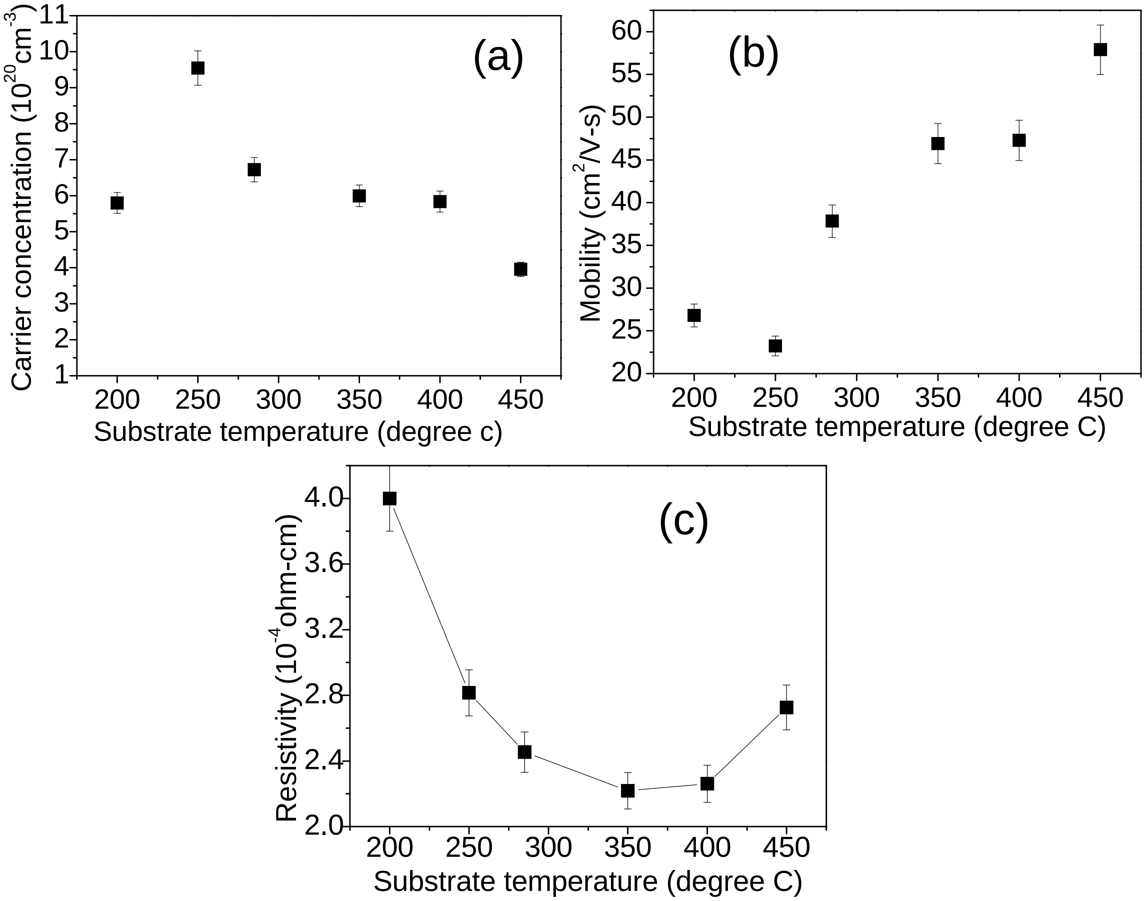

Figure 3.21 Substrate temperature effects on resistivities of as-grown GZO layers grown on 200-Torr p-GaN under oxygen pressure of ~4×10^{-6} Torr by MBE.

Figure 3.22 shows three AFM scans representing surface morphologies of the GZO layers grown at different substrate temperatures. As seen from the figure, the surface morphology changes from relatively smooth one to a rather rough surface with pronounced large islands when substrate temperature increases from 200°C to 450°C. For GZO film grown at the substrate temperature of 200°C [Figure 3.22 (a)], the root-mean-square (RMS) surface roughness is ~5.5 nm. As substrate temperature increased to 285°C, well defined islands typically 200-250 nm in diameter and ~150 nm in height were formed on the top of relatively smooth underlying GZO surface [Figure 3.22 (b)] resulting in RMS ~16.2 nm. Further increase in substrate temperature to 400°C gives rise to the larger density of 3-dimensional islands [Figure 3.22 (c)] and, RMS value increases to ~19.1 nm. The rough surface of GZO layer with the typical island size of the order of light wavelength is desirable for enhancing the light extractions from LEDs as it assists to scatter photons propagating at large angles to the surface normal towards the surface. Therefore, our results indicate that the GZO layers grown at 350-400°C should provide the best performance as electrodes to p-GaN in terms of both of electrical properties and the ability to enhance the photon extraction.

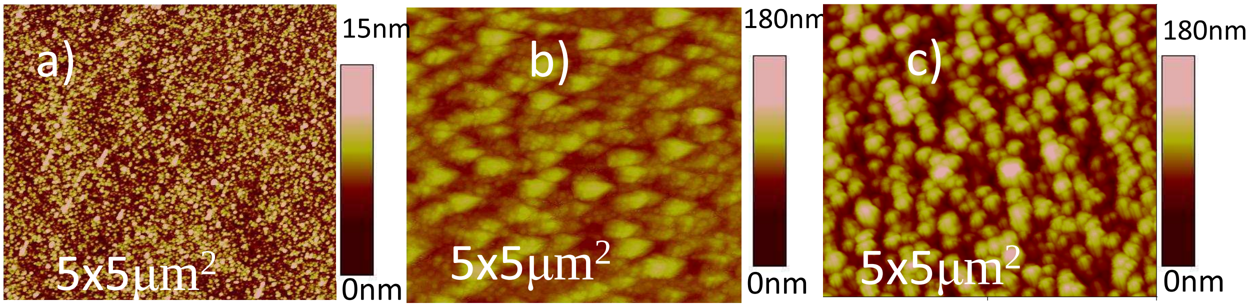

Figure 3.22 Effects of substrate temperatures of (a) 200°C, (b) 285°C, and (c) 400°C on surface morphology of GZO layers grown on 200-Torr p-GaN.

3.5 Summary of MBE growth parameter effects and the thermal stability of highly conductive and transparent GZO grown under metal-rich conditions

In short, the MBE growth parameter effects have been investigated. The highly conductive and transparent GZO layers can be achieved under the conditions of $P_{O2} = 4.5\times10^{-6}$ Torr, T_{Ga}=400^{o}C, and T_{sub}=350-400^{o}C. To achieve highly conductive and transparent GZO, metal-rich conditions instead of oxygen-rich conditions are needed. Moreover, RTA annealing in N_2 environment was found to improve the electrical properties.

One more important thing we have to consider is the thermal stability of GZO for real application. The thermal stability of conductivity of highly conductive GZO ($n=\sim 9\times 10^{20}$ cm^{-3}, RT $\mu=\sim 42$ $cm^2/V\cdot s$) grown under metal-rich conditions was investigated using post-thermal annealing in oxygen environment. Figure 3.23 illustrates the electrical properties of the GZO layer annealed at different temperatures varying from 475 °C to 600 °C. When the annealing temperature increases from 475 °C to 550 °C the electron concentration dramatically drops with temperature while when the annealing temperature further increases the electron concentration virtually saturates. Although the annealing time has some effect, the whole tendencies in the effect of annealing temperatures on the electron concentrations are similar for different annealing times. The mobilities for the GZO layers annealed at higher temperatures are generally lower than those for the GZO layers annealed at lower temperatures as seen in Figure 3.23 (b). The resistivity of the GZO layer annealed at 475 °C even for 2 hours is just slightly higher than that of the corresponding as-grown GZO layer. Therefore, the GZO films grown under metal-rich conditions are thermally stable in conductivity up to 500 °C, which is better than the previously reported ZnO-based TCOs (up to 400 °C)[102,103]. The reduction in electron concentration with annealing in oxygen environment is probably because ZnO based films can absorb the oxygen atoms under high temperature oxidation environment, which prefer to stay at grain boundaries, and thus induces the acceptor-like interface states which trap free electrons.[39,104,105] The high mobilities for the GZO films annealed at a temperature below 520 °C could due to the weak effects from compensation caused by the acceptor-like interface states and grain boundary scattering while they appear to become dominant for GZO films annealed at temperature higher than 520 °C.

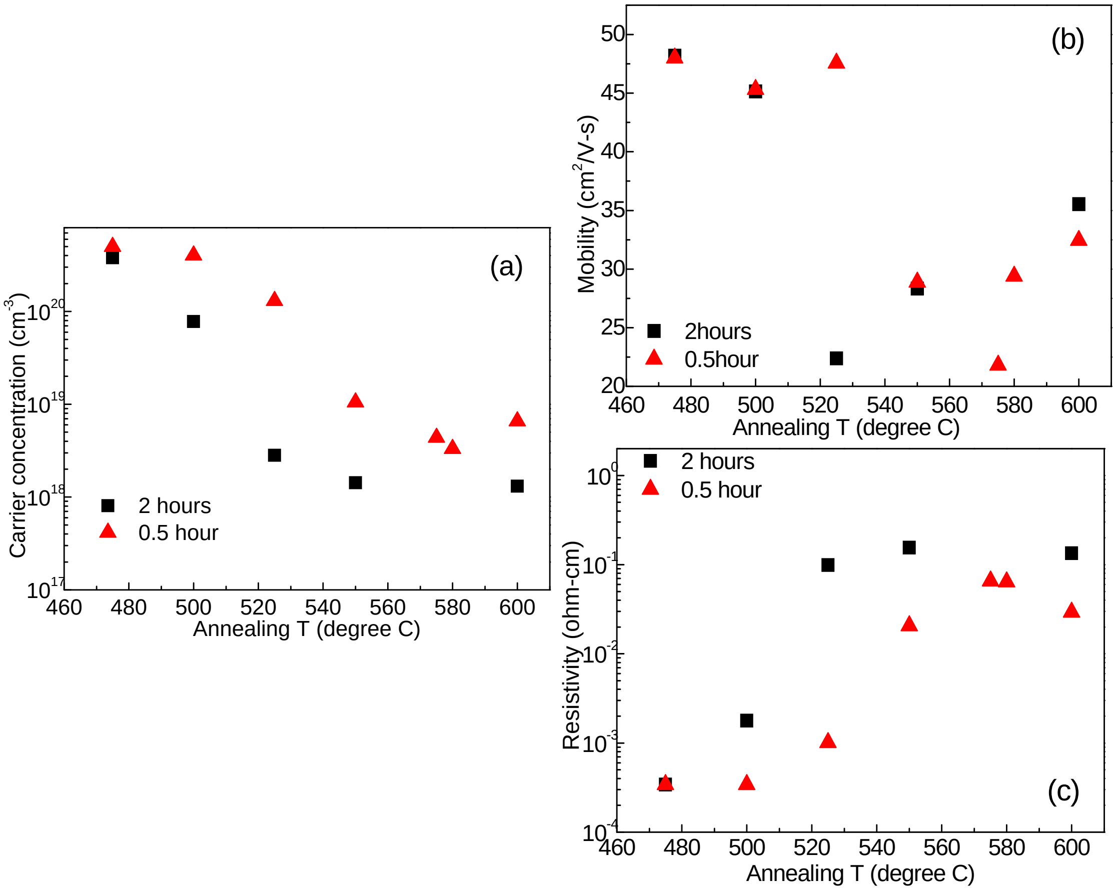

Figure 3.23 Effects of post-growth thermal annealing in oxygen environment on the electrical properties of highly conductive GZO (n=~9×10^{20} cm^{-3}, RT μ=~42 cm^2/V·s)

Chapter 4 Applications of GZO as Transparent Electrodes in InGaN-LEDs and Effects of GaN Templates on GZO Properties

4.1 Applications of GZO as transparent electrodes in InGaN-LEDs

4.1.1 Growth of GZO on LED templates

The InGaN/GaN quantum well LEDs with GZO transparent p-electrode (referred below as GZO-LEDs) have been fabricated as follows [Figure 4.1]. The active-region structures consisting of 6 $In_{0.14}Ga_{0.86}N$ quantum wells 2 nm thick separated with $In_{0.01}Ga_{0.99}N$ barriers, were designed to emit at 400–410 nm were grown on (0001) sapphire substrates in a vertical low-pressure metalorganic chemical vapor deposition (MOCVD) system. The barrier thickness in the multiple quantum well regions was chosen to be 12 nm to encourage efficiency droop at high injection currents for investigative purposes. GZO transparent electrodes were grown epitaxially on the top p-type GaN of the LED structures by plasma-assisted MBE at a substrate temperature of 400^{o}C under metal-rich conditions (metal (Ga+Zn) to oxygen ratio >1). The thickness of GZO films was controlled to be ~400 nm. These conditions are consistent with the best growth conditions for GZO on a-sapphire substrates by MBE, producing resistivities below 3×10^{-4} Ω cm and transparency as high as ~95% in the visible range

For comparison, InGaN-based LED sturcures with 5 nm Ni/5 nm Au transparent p-electrode (referred below as Ni/Au-LEDs) have been fabricated [Figure 4.1]. The detailed fabrication information can be found else and the mesa size is 250 µm in diameter.[106] Again, structural properties were characterized by XRD and surface morphology of the GZO films were assessed from AFM, scanning electron mictroscopy (SEM) measurements. Electrical properties were studied by Hall effect measurements using the van der Pauw configuration and current-voltage (I-V) measurements. RTA was employed to investigate post-annealing effects on GZO properties and LED performance, respectively. Relative EQE of the LEDs with the GZO electrodes and control LED structures with thin Ni/Au top electrodes were assessed from pulsed and CW electroluminescence (EL) measurements.

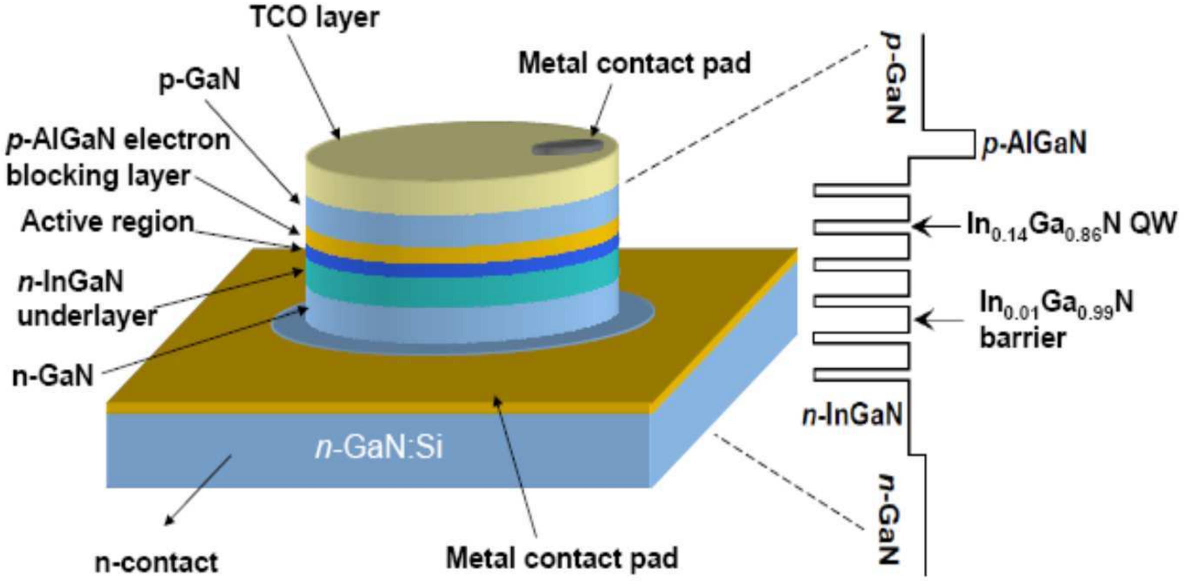

Figure 4.1 The schematic diagram of the InGaN/GaN LED structure with TCO (GZO or Ni/Au) as transparent electrode along with its band structure (GZO also serves as the current spreading layer).

4.1.2 Structural properties of GZO grown on LED templates

As seen from Figure 4.2, GZO grows epitaxially on GaN with GZO [0001]//GaN [0001] and GZO [10-11]// GaN [10-11]. From the symmetric two-theta omega scan as illustrated in Figure 4.2 (a) and using the sapphire substrate as a reference, the *c* lattice constants of GZO films were calculated to be 5.208 Å. While from skew-symmetric two-theta omega scan of (101) reflection shown in Figure 4.2 (b), the *a* lattice constants of GZO were calculated to be 3.256 Å by using GaN as a reference and the *c* lattice constant found from the symmetric scan. The calculated lattice parameters of GZO grown on p-GaN are very close to those of bulk ZnO, indicating very low lattice distortion even in ZnO films with very high Ga concentrations.

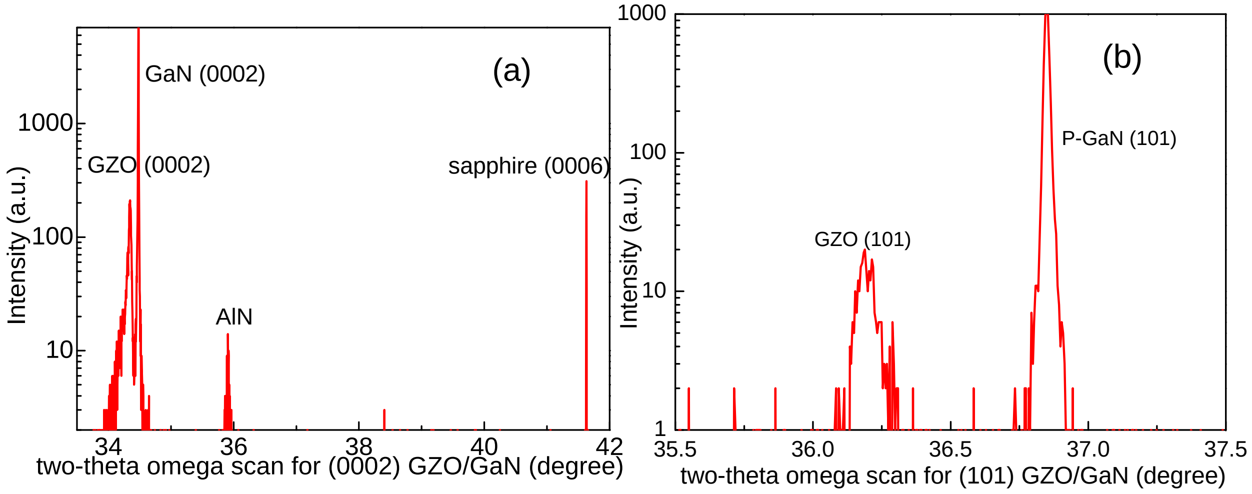

Figure 4.2 Epitaxial relationships between ZnO and GaN templates. (GZO [0001]//GaN [0001] and GZO [10-11]// GaN [10-11]).

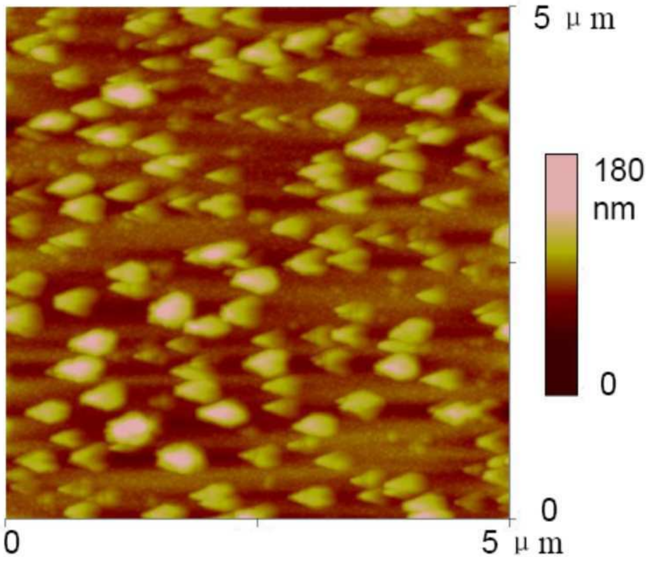

Figure 4.3 Typical surface morphology of GZO layer grown on top p-GaN (0001) by AFM.

AFM measurements showed that the surfaces of the GZO films grown on the top p-GaN are rough and the root mean square (RMS) roughness of these GZO layers varies from 10 to 20 nm.

As an example, Figure 4.3 shows a typical AFM image of these GZO films, which has a RMS of ~17 nm. As seen from Figure 4.3, well defined islands were formed on the relatively smooth GZO surface during growth.

Figure 4.4 shows a bright-field TEM image of one GZO-LED layer with similar surface morphology as shown in Figure 4.3. As seen from this TEM image the GZO surface is rough. These rough surfaces of GZO layers are thought to be helpful in photon extractions from LED active regions since they could scatter more photons out of the LEDs. TEM studies also show that dominating defects in the GZO layers grown in 3-dimensional growth mode are low-angle grain boundaries and threading dislocations. The averaged grain size is 80±40 nm. Grain boundary scattering could be one of the main mechanisms limiting the carrier transport in GZO. Threading dislocations in GZO layer are the direct consequence of the threading dislocations in GaN which originated from the GaN-sapphire interface due to the large lattice mismatch.

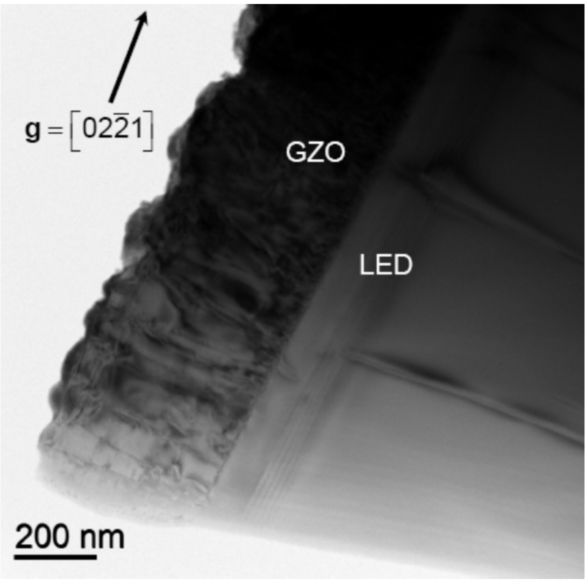

Figure 4.4 TEM image of one GZO-LED in the bright field mode.

<u>4.1.3 Electrical properties and optimization of series resistance of GZO-LEDs</u>

Room temperature Hall measurements show that the as grown GZO layers on p-GaN have a resistivity of below 3×10^{-4} Ω-cm. RTA annealing in nitrogen environment can reduce their resistivity to below 2×10^{-4} Ω-cm. The low resistivity of GZO is the basis for current spreading in LED applications. Typically, the GZO sheet resistance itself was found by RT Hall measurements to be ~5 Ω before the n-type contact (Ti/Al/Ni/Au contacts on n-type GaN) was fabricated in these LED structures.

Figure 4.5 presents the results of transport measurements for the 400-nm-thick GZO films as a function of RTA annealing temperature starting from 625 °C. As the annealing temperature increases, the sheet resistance and, consequently, resistivity first drops reaching the minimum value of ~1.9 x 10^{-4} Ω cm for the samples annealed at 675 °C and then significantly increases.

The carrier density increases initially as the annealing temperature rises, and then reduces dramatically from ~8.6 to ~3.5 × 10^{20} cm^{-3} as annealing temperature increases from 675 to 800 °C, while Hall mobility increased throughout the whole temperature range, from ~27 cm^2/V-s in the as-grown sample to ~40 cm^2/V-s in the sample annealed at 800°C. The increase in mobility is attributable to improvement of the crystal quality of GZO upon high-temperature annealing. Although it is generally believed that scattering on ionized impurities is the main factor determining mobility in heavily doped materials,[107] Minami *et al.* have pointed out that crystallinity can also affect mobility for TCOs with carrier concentration in the range of 10^{20}-10^{21} cm^{-3}.[108] Thus, in terms of electrical properties of the GZO layers, the optimum annealing temperature is 675 °C. However, the optimum temperature for annealing of Ti/Al/Ni/Au contacts used for n-type GaN in the LED structures is 800 °C, which can deteriorate the resistivity and consequently the sheet resistance of GZO transparent electrode. As indicated in the above mentioned example of RTA annealing effects, the sheet resistance of GZO annealed at the temperature of 800 °C is higher than 10 ohms which will definitely reduce the ability of GZO p-electrode to spread current. Therefore, a trade-off between the resistances of p- and n-side contacts should be made to achieve the best performance of the LEDs, unless GZO films are deposited after the n-contact anneal.

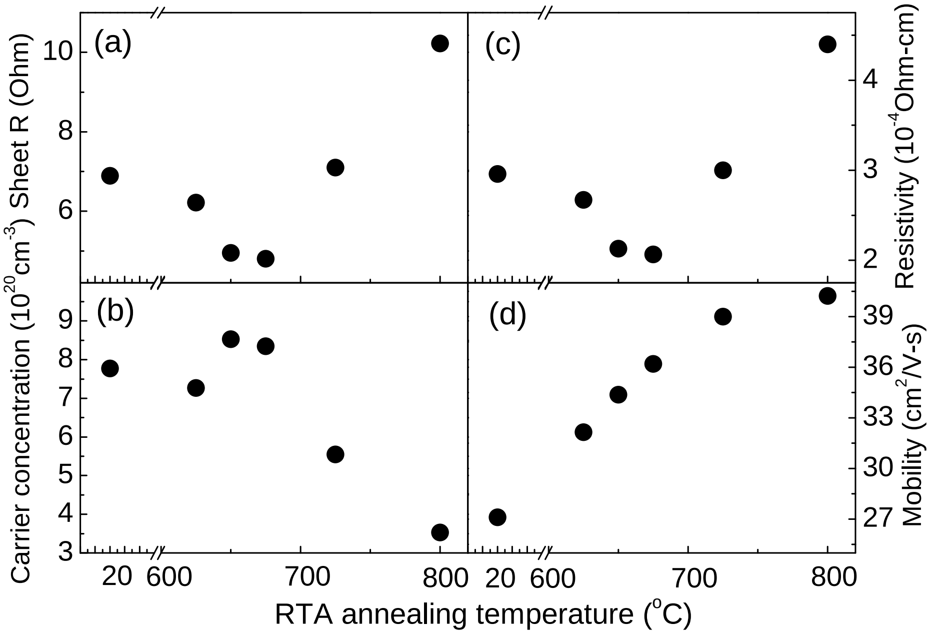

Figure 4.5 (a) Sheet resistance, (b) carrier concentration, (c) resistivity, and (d) electron mobility of 400-nm-thick GZO films vs. RTA annealing temperature.

Prior to electrical characterization of the InGaN LEDs, we evaluated the current-voltage characteristics between the GZO and p-GaN layers. As clearly seen in the Figure 4.6, the as-grown GZO shows ohmic behavior on p-GaN layers without metal contact pads deposited on the top of GZO. The detailed information regarding the I-V characterizations can be found elsewhere.[106] The GZO layer annealed at the optimum condition of 675 °C in nitrogen environment as mentioned earlier should behave more ohmic since the resistivity is considerably reduced compared with the as-grown one and therefore the same I-V characterizations on annealed GZO layers as shown in Figure 4.6 grown on p-GaN template were not repeated.

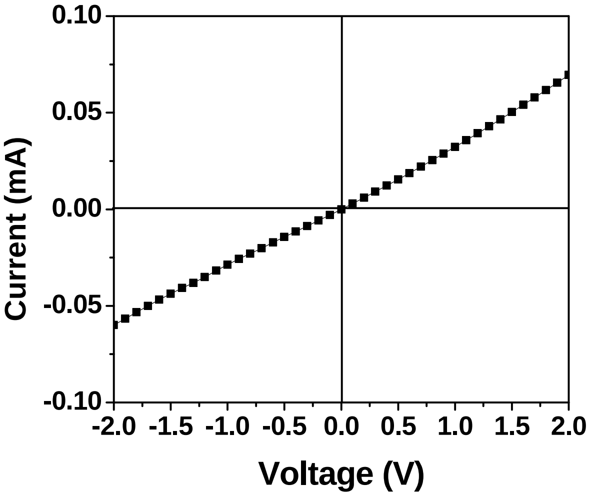

Figure 4.6 Current-voltage (I-V) characteristics of the GZO contacts on p-GaN measured in transmission lines patterns having 40 μm contact spacing.

Figure 4.7 shows I-V and pulsed EL characteristics measured for GZO-LEDs annealed at temperatures of 675, 780, and 800 °C, respectively. One can see that the annealing temperature has a minor effect on the I-V characteristics of the GZO-LED. The operating voltage of the GZO-LEDs is very close to each other, which is ~ 3.2 V. The slope of the I-V characteristics and, consequently, the dynamic series resistances of these GZO-LEDs are also comparable. However, the EL characteristics exhibit a strong dependence on the annealing temperature (Figure 4.7). The GZO-LED annealed at 675 °C shows the highest maximum EQE as compared to those annealed at 780 °C and 800 °C. Even the small difference of annealing temperatures between 780 °C and 800 °C causes a considerable difference in their EQEs. It should be mentioned that three regions of the LED structure, which are n-contact, active region, and p-contact, contribute to I-V characteristics, and annealing can cause drastic changes in their resistances. Therefore, a complex interplay between contributions, first of all, p-contact and n-contact can be responsible for insignificant changes of the resulting I-V curves, whereas the balance between injected electrons and holes can change substantially. In addition, the optical transmittance of the GZO layer could be also changed upon thermal treatment. Further studies are needed to gain insight into the genesis of this dramatic effect of annealing on device performance of GZO-LEDs.

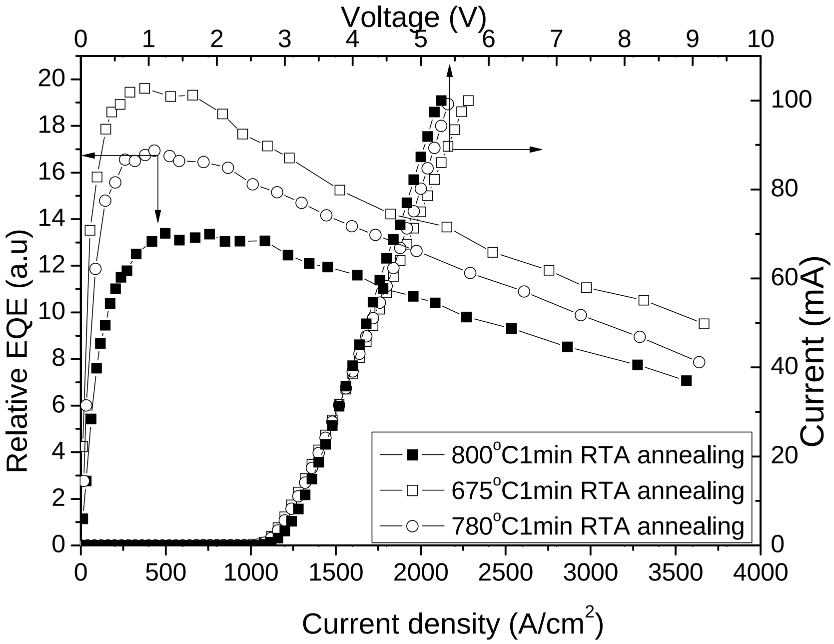

Figure 4.7 RTA annealing effects on current-voltage (I-V) and pulsed electroluminescence (EL) measurements of GZO-LEDs.

4.1.4 Comparisons between GZO-LEDs and Ni/Au LEDs

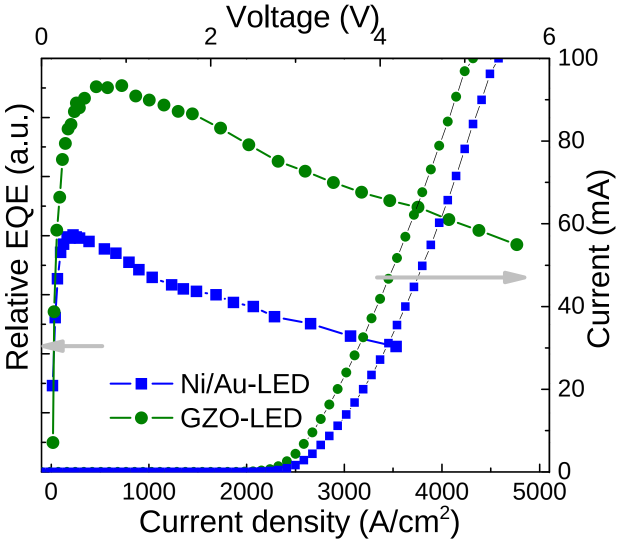

Figure 4.8 Relative external quantum efficiency *vs.* current density and current *vs.* voltage for LEDs with Ni/Au and GZO *p*-contact layers.

Figure 4.8 shows the I-V and pulsed EL characteristics which are very repeatable and thus only one of each curves is shown for clarity. The GZO-LEDs have virtually the same vertical series resistance (typically ~18-22 Ohm) as that of the Ni/Au-LEDs (typically ~17-23 Ohm). It can also be seen that the forward voltage measured at 20 mA is 3.5 V and 3.7 V for GZO-LEDs and Ni/Au-LEDs, respectively. The EQE of the GZO-LED is 1.7-2 times higher than that of Ni/Au-LED at high current densities due to what we believe GZO's relatively higher transparency. In addition, the rough surface as shown earlier could assist photons propagating at high angles to the surface normal to escape from the LED due to multiple scattering, which will increase the extraction efficiency and hence the EQE of the GZO-LEDs. Moreover, as seen from Figure 4.8 GZO-LEDs can withstand much higher current densities (4700 A/cm^2) than that of Ni/Au LEDs (3500 A/cm^2) under pulsed mode.

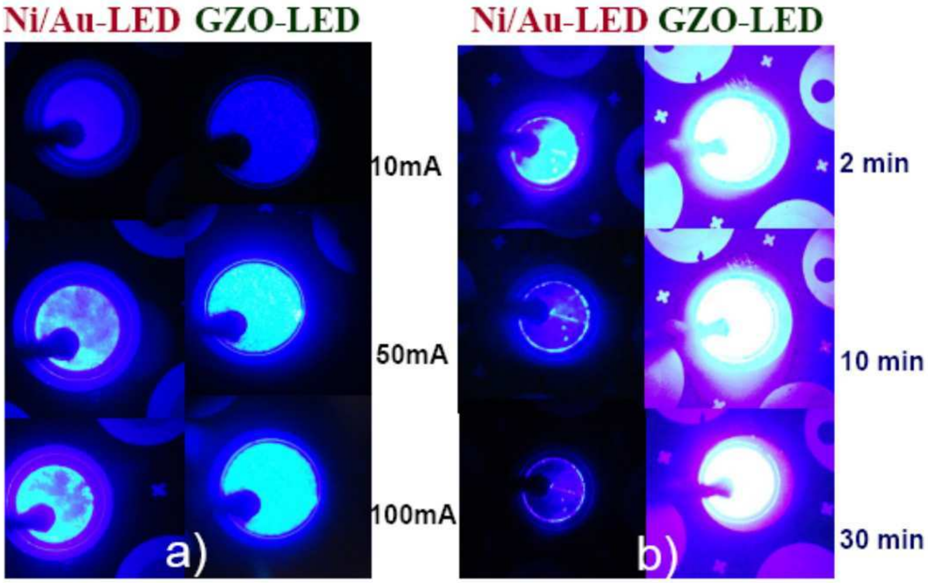

Figure 4.9 Light emission images of GZO-LEDs and Ni/Au-LEDs under different DC currents (a) and under injection current of 100 mA for different times.

Figure 4.9 a) illustrates the light emission of GZO-LEDs and Ni/Au-LEDs under different DC currents. The filamentation phenomenon due to the non-uniform distribution of current is clearly seen for Ni/Au-LEDs at an injection current of 50 mA (159 Acm^{-2}) while it is not seen for GZO-LEDs even at an injection current of 100 mA (318 Acm^{-2}). Figure 4.9 b) compares the time evolution of the light emitting of GZO-LEDs and that of Ni/Au-LEDs under the same injection current of 100 mA. In short, GZO-LEDs have many advantages over Ni/Au-LEDs which can be found elsewhere.[106,109]

So far what I have discussed is related to GZO-LEDs with a mesa size of 250 µm in diameter. To further illustrate that GZO layer is good as a current spreading layer which can eliminate the filamentation phenomenon, GZO-LEDs with a mesa size of 400 µm × 400 µm were fabricated. Figure 4.10 illustrates the uniform light emission of GZO-LEDs with a mesa size of 400 µm × 400 µm but with different metal grids, which clearly shows GZO is a promising TCO as transparent electrodes in LED applications.

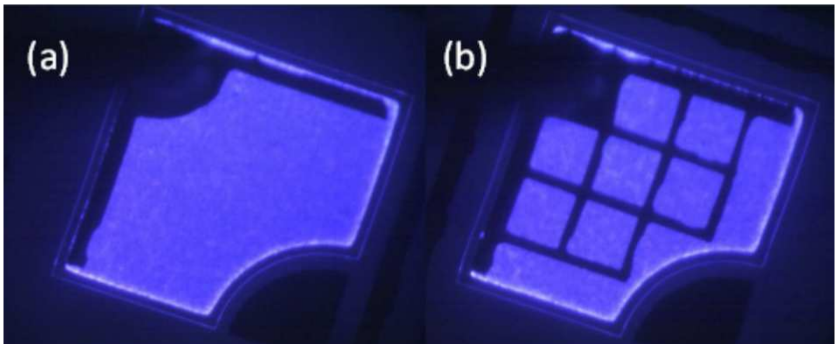

Figure 4.10 Pictures of uniform light emission of GZO-LEDs with a mesa size of 400 µm × 400 µm but with different metal grids (note: the applied injection DC current is 50 mA and the exposure time is 5 ms).

4.2 Effects of morphologies of p-GaN layers on GZO properties

In addition to the high conductivity and high transparency required, the surface morphology of GZO/AZO is also an important factor to be considered, which could have considerable effect on device performance. For example, rough surface is desired to improve the photon extraction efficiency and consequently the external quantum efficiency in GaN-based LEDs. In contrast, very smooth GZO/AZO surface (the surface roughness should be very small compared with the emitting wavelength) is required to reduce the optical loss in GaN-based vertical cavity surface-emitting lasers (VCSELs). It is consequently important to investigate the effects of GaN templates on the properties of GZO/AZO.

Again, InGaN-LEDs with p-GaN on the top as discussed above were used as the bases for GZO growth. However, the p-GaN layers were grown at substrate temperature of 950 °C with 2 different chamber pressures of 200 and 400 Torr, respectively. All procedures for GZO growth are the same as I used before to achieve highly conductive and transparent GZO layers and therefor are not repeated.

4.2.1 Effects of morphologies of p-GaN layers on GZO structural and optical properties

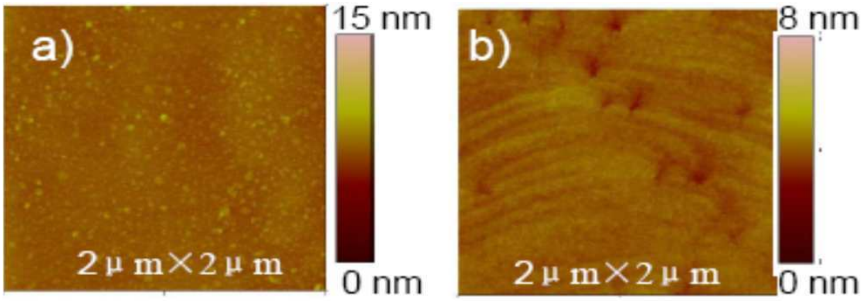

Figure 4.11 Surface morphologies of (a) 200 Torr p-GaN, (b) 400 Torr p-GaN.

Figure 4.11 (a) and (b) show the AFM images of two examples of p-GaN layers grown under substrate temperature of 950°C but different MOCVD chamber pressures of 200 and 400 Torr, respectively. AFM measurements showed the root-mean-square (RMS) surface roughness of 0.6 nm and 0.4 nm for p-GaN grown at 200 Torr and 400 Torr, respectively. Atomic steps are clearly seen for the 400-Torr p-GaN [Figure 4.11 (b)], indicating better quality.

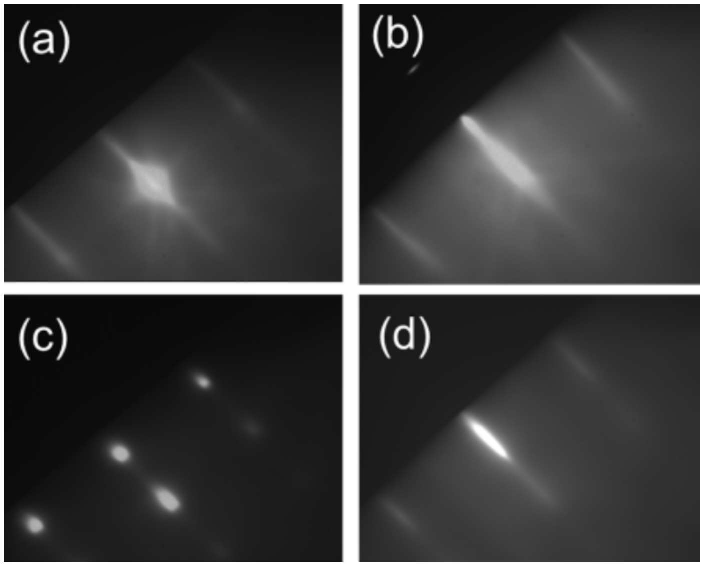

Figure 4.12 RHEED patterns taken along [1-100] azimuth from (a) 200 Torr p-GaN, (b) 400 Torr p-GaN, (c) 3D GZO on 200 Torr p-GaN, and (d) 2D GZO on 400 Torr p-GaN.

The *in situ* monitoring of GZO growth with RHEED revealed a strong effect of the p-GaN surface morphology on the growth mode and surface morphology of the resultant films. Figure 4.12 (a) and (b) shows the RHEED patterns of 200-Torr p-GaN and 400-Torr p-GaN templates, respectively. The GZO layers grew in a 3D growth mode on 200-Torr p-GaN templates, while 2D growth mode was observed for the layers on 400-Torr p-GaN. AFM data are in a good agreement with RHEED observations. Figure 4.13 (a) and (b) show the surface morphologies of two GZO layers grown on the top of 200-Torr p-GaN and 400-Torr p-GaN, respectively. As seen from Figure 4.13 (a), the layer grown on 200-Torr p-GaN is featured by a very rough surface with an RMS surface roughness of 10.7 nm. The GZO layer is composed of dense islands typically 200-250 nm in diameter and 150 nm in height. In contrast, the layer grown on the top of 400-Torr p-GaN with pronounced atomic steps show a smooth surface with an RMS roughness of about 2 nm [Figure 4.13 (b)].

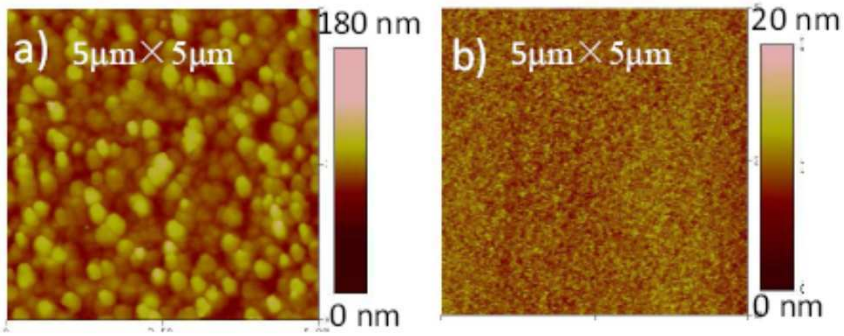

Figure 4.13 Surface morphologies of (a) 3D GZO on 200 Torr p-GaN, and (b) 2D GZO on 400 Torr p-GaN.

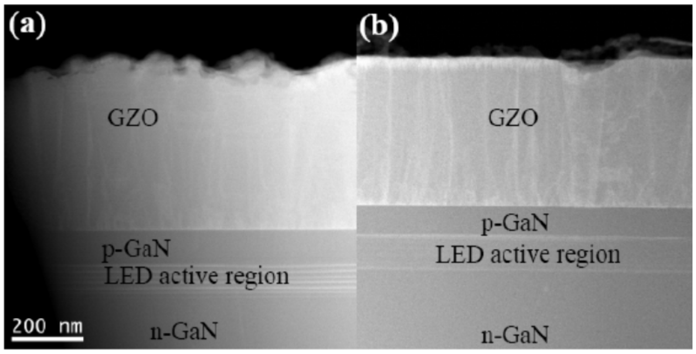

Figure 4.14 TEM data of GZO (a) on 200-Torr p-GaN and (b) on 400-Torr p-GaN.

Figure 4.14 (a) and (b) show STEM data for GZO layers grown on 200-Torr p-GaN and 400 Torr p-GaN, respectively. Grain boundaries are visible in both Figure 4.14 (a) and (b) but the surface morphologies are different. The results of surface roughness are consistent with those from AFM measurements and RHEED characterizations.

Figure 4.15 shows symmetric (0002) XRD two-theta omega scans for GZO layers grown on 200-Torr p-GaN and 400-Torr p-GaN, respectively, as discussed above. As seen clearly from the figure, the GZO layers grown on different p-GaN templates show a large difference in peak positions indicating different *c* lattice parameters. Similar phenomenon was also observed for skew-symmetric $(1\bar{1}01)$ XRD reflections which are not shown here.

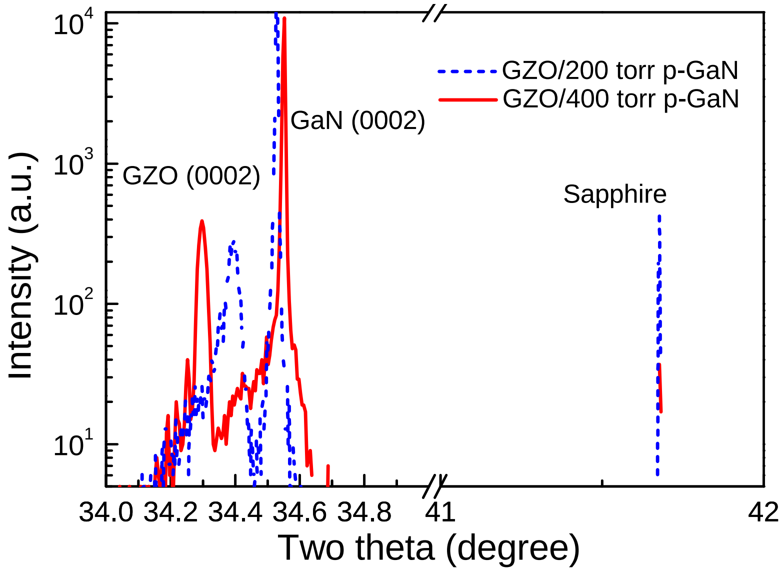

Figure 4.15 XRD 2θ-ω scans of GZO layers grown on 200-Torr (dashed) and 400-Torr p-GaN (solid).

5 GZO layers grown on 200-Torr p-GaN (in 3D growth mode) and 3 on 400-Torr p-GaN (in 2D growth mode) were analyzed. The *c* lattice constants were determined from symmetric XRD scans using the (0006) reflection from sapphire substrate as a reference. The *a* lattice constants were calculated from inter-plane distances found from skew-symmetric two-theta omega scan of $(1\bar{1}00)$ reflection by using the GaN reflection as a reference and the *c* lattice constants found from the symmetric scans. The *c* lattice constants of GZO layers grown on 400-Torr p-GaN (5.220-5.222 Å) are much larger than those of GZO layers grown on 200-Torr p-GaN (5.200-5.210 Å). The *c* lattice constants of GZO on 400-Torr p-GaN are substantially larger than the bulk ZnO *c* lattice parameter equal to 5.206 Å, while the *c* lattice constant of GZO deposited on 200-Torr p-GaN is comparable to or slightly smaller than the bulk value. In-plane *a* lattice constant for the GZO layers grown on different p-GaN templates shows comparable variations as in *c* lattice constant in terms of percentage: $a \approx 3.25$ Å for GZO on 400-Torr p-GaN which is virtually coincide with the bulk *a* lattice parameter of ZnO, while this value is slightly higher (*a*

≈ 3.26 Å) for GZO on 200-Torr p-GaN templates. Full width at half-maximum (FWHM) of the (0002) XRD rocking curves measured on GZO layers on 400-Torr p-GaN layers are ranging from 0.07 to 0.09 degree which is much smaller than FWHM for GZO on 200-Torr p-GaN varying in a range of 0.13-0.2 degree. This finding suggests lower density of extended defects in GZO layers grown on 400-Torr p-GaN. The origin of the observed variations in lattice constants and FWHM of XRD rocking curves induced by underlying p-GaN layers are not fully understood yet.

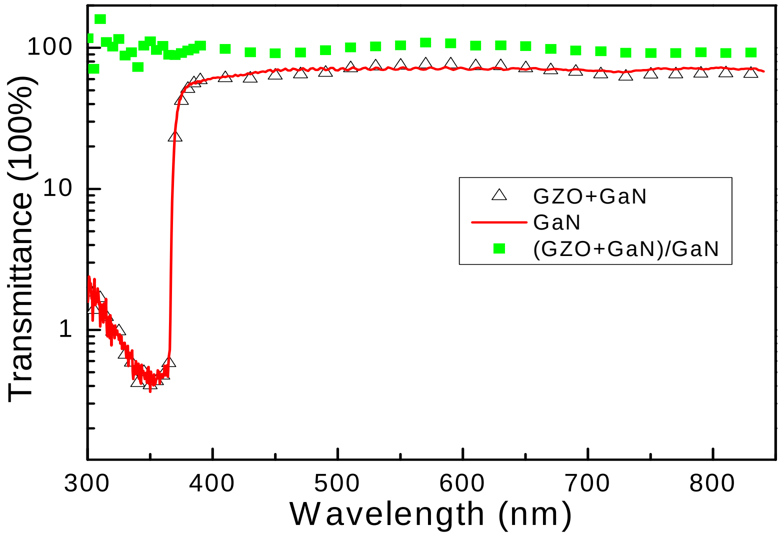

Figure 4.16 Transmittance spectra of GaN/sapphire template, GZO/template, and the ratio of (GZO+GaN)/GaN.

Although the morphologies of p-GaN templates have strong effects on GZO structural properties as revealed by RHEED, SEM, TEM, and XRD, the transmittance of GZO grown on 200-Torr p-GaN is comparable to that of GZO grown on 400-Torr p-GaN, which average value is above 95% in the visible range as shown in Figure 4.16.

4.2.2 Effects of morphologies of p-GaN layers on GZO electrical properties

Carrier concentrations in the GZO layers grown in both 2D and 3D growth modes are 5-to-6 $\times 10^{20}$ cm^{-3}, while Hall mobilities are higher in the layers grown in 2D mode on 400-Torr p-GaN templates (~90 cm^2/V-s *vs.* ~45 cm^2/V-s). As a result, resistivities in the GZO layers grown on 400-Torr p-GaN are ~ 1.5×10^{-4} Ω cm, which is lower than the values of ~ 2×10^{-4} Ω cm obtained for 3D GZO on 200-Torr p-GaN. However, the mobility magnitudes and, consequently, the resistivities are likely overestimated and underestimated, respectively, because of possible parallel conduction through the n$^+$ GaN layer of the LED structure located below p-GaN. To confirm the concern of overestimating the mobility in GZO layers, temperature-dependent Hall measurements were performed for GZO layers grown on LED templates.

Figure 4.17 (a) shows the temperature-dependent electron concentrations measured by Hall method in Van der Pauw configuration, which temperature-dependence is inconsistent with that for degenerate TCOs since the electron concentration is temperature-independent due to the degeneracy. Meanwhile, the temperature-dependence of mobilities for GZO grown on LED templates is also abnormal. For TCOs, the typical temperature-dependent mobility curve has two distinct parts and the part for T below about 150 K is temperature-independent while the other part for T above 150 K exhibits a tendency of decrease with temperature. The abnormal phenomena therefore prove that the measured electrical properties for GZO layers were affected by the underlying LED templates. However, in comparison between GZO grown on 200-Torr p-GaN and GZO grown on 400-Torr p-GaN templates, the effect of 200-Torr p-GaN template is smaller as shown in Figure 4.17. This observation is consistent with PL measurements.

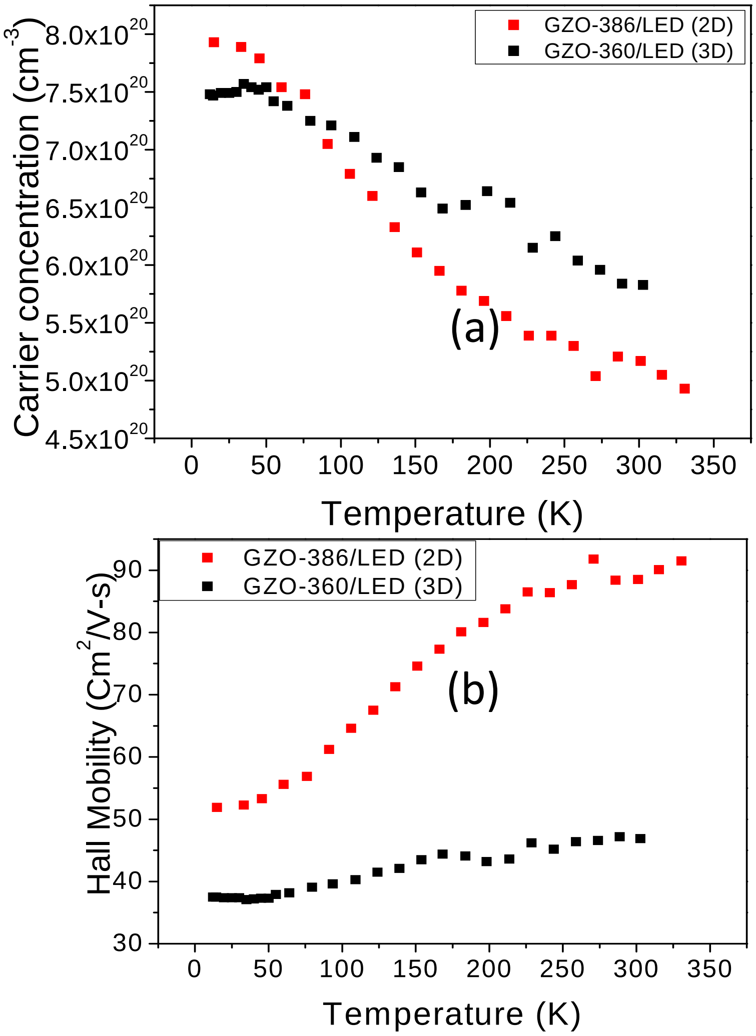

Figure 4.17 Temperature-dependent (a) electron concentrations and (b) mobilities measured by Hall measurements.

As shown in Figure 4.18, the PL profile of GZO layer grown on 200-Torr p-GaN template is similar to that of GZO grown on a-plane sapphire substrate, indicating the effect of 200-Torr p-GaN template on GZO properties is small. In contrast, the PL profile of GZO grown on 400-Torr p-GaN template showed a strong peak around 2.25 eV (Yellow band from GaN), which indicates that the underlying GaN layers (probably p-GaN grown under 400-Torr) are wrong and have strong effects on GZO electrical property measurements.

In an effort to eliminate the effects of the underlying GaN layers and consequently to get accurate GZO electrical properties, RTA annealing in nitrogen environment were employed for GZO layers grown on both 200-Torr p-GaN and 400-Torr p-GaN templates above mentioned. Temperature-dependent Hall measurements indicated that RTA annealing can only eliminate the effect of 200-Torr p-GaN templates on measured GZO electrical properties. This should be due to the high material quality of GaN layers in 200-Torr p-GaN template as compared with 400-Torr p-GaN template as shown in Figure 4.18.

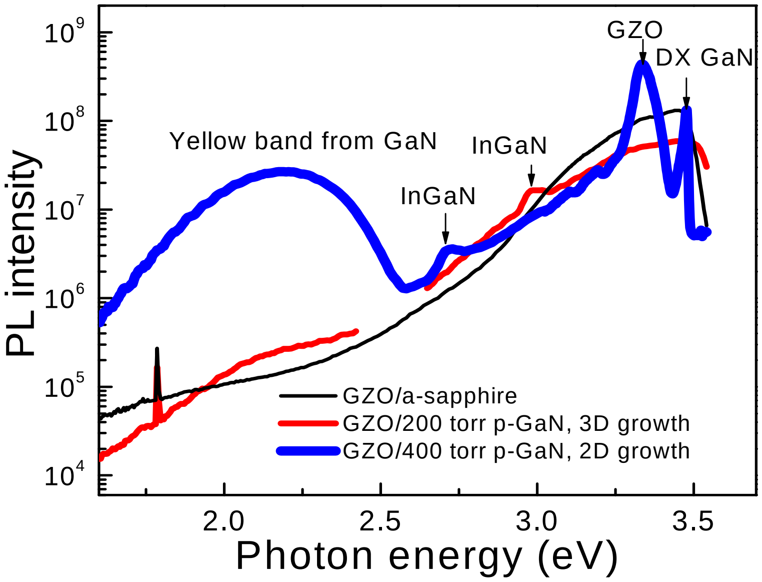

Figure 4.18 Comparisons of PL measurements for GZO grown on 200-Torr p-GaN, 400-Torr p-GaN, and a-sapphire substrates.

Figure 4.19 compares the electrical properties of GZO layer grown on 200-Torr p-GaN before and after RTA annealing in nitrogen environment. After annealing, the electron concentrations are visually temperature-independent with small random variations at some temperatures. At the same time, the temperature-dependent mobility curve exhibits the similar temperature-dependence as those from typical TCOs. For this special GZO layer, the RT electron concentration, mobility, and resistivity are ~5×10^{20} cm^{-3}, ~45 cm^2/V-s, and ~ 2.7×10^{-4} Ω cm, respectively, which are reasonable.

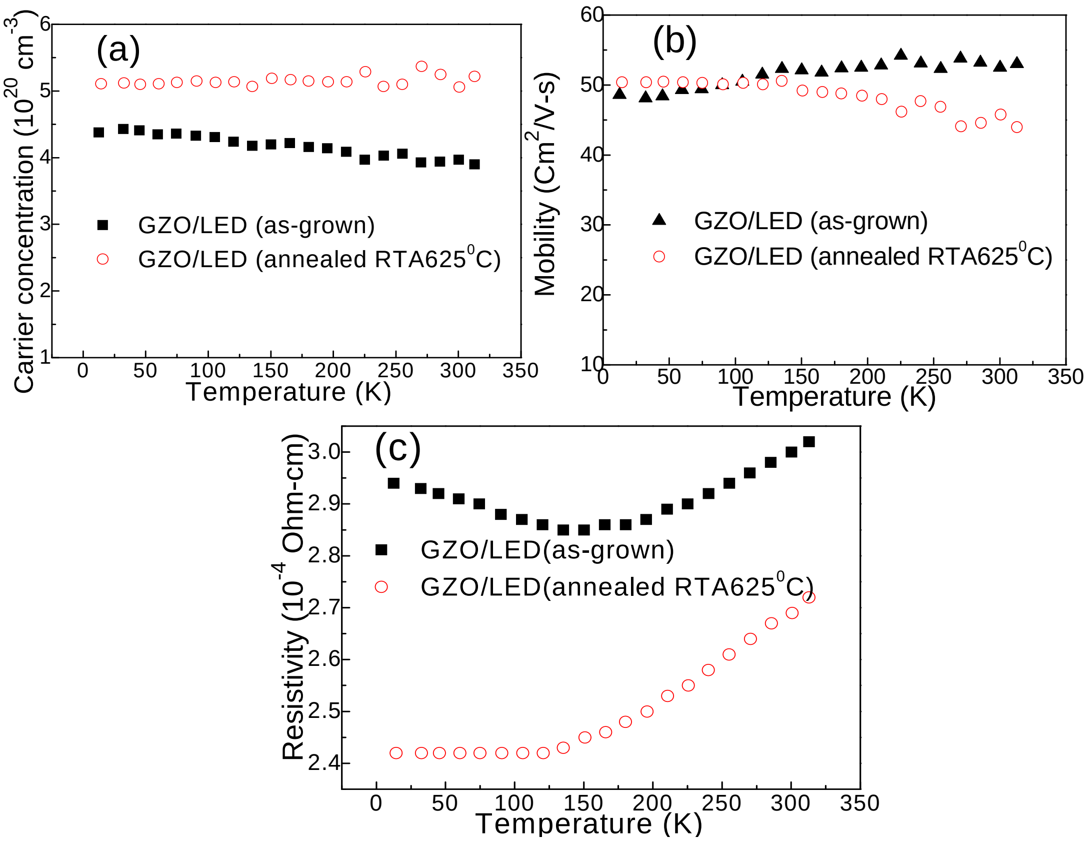

Figure 4.19 RTA annealing effects to eliminate the effects of 200-Torr p-GaN template on measured GZO electrical properties of (a) electron concentration, (b) mobility, and (c) resistivity.

On the other hand, GZO layers were grown again on new LED templates which still used 400 Torr for p-GaN growth but the substrate temperature was increased to 1030^{o}C instead of 930^{o}C (400-Torr-1030 ^{o}C p-GaN templates). The 400-Torr-1030 ^{o}C p-GaN templates were found to have comparable surface roughness to that of previously 400-Torr p-GaN, where atomic steps are clearly seen from AFM measurements. The GZO layers grown on 400-Torr-1030 ^{o}C p-GaN templates have very smooth surface as indicated by the 2D growth mode characterized by

RHEED. Figure 4.20 illustrates the XRD characteristics of GZO with a thick ZnO buffer layer (5 nm LT ZnO+50 nm HT ZnO) grown on the 400-Torr-1030 °C p-GaN template. Noting the small lattice mismatch between ZnO and GaN, the XRD scans were carried out in triple-axis mode in order to distinguish the peaks. Thickness fringes are clearly seen in Figure 4.20, which indicates sharp interfaces and highly epitaxial GZO grown on 400-Torr-1030 °C p-GaN template. Note that no fringes were observed for GZO/200-Torr *p*-GaN template and the (0002) peak intensity is also about one-order lower than what we observe here. For (101) peaks which are not shown here, no obvious difference between GZOs grown on all GaN templates is seen because the peak intensities are very weak.

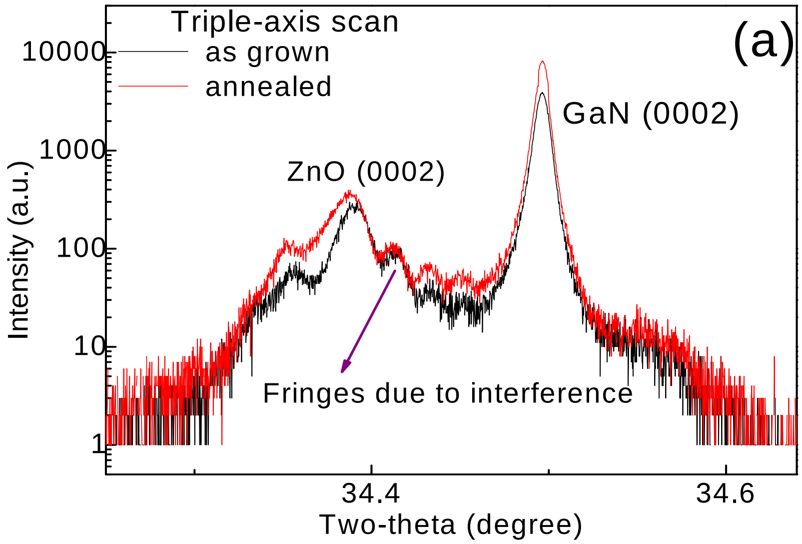

Figure 4.20 XRD 2θ-ω scan of GZO with a thick ZnO buffer layer (5 nm LT ZnO+50 nm HT ZnO) grown on 400-Torr-1030 °C p-GaN template.

Unexpected behaviors similar to the observation for as-grown GZO grown on 200-Torr p-GaN/400-Torr p-GaN templates have also been noted for as-grown GZO grown on 400-Torr-1030°C p-GaN with a 5 nm LT ZnO buffer. Again, post-annealing in N_2 makes it behave like high quality TCOs. Figure 4.21 (a), (b), and (c) show the temperature-dependent electron

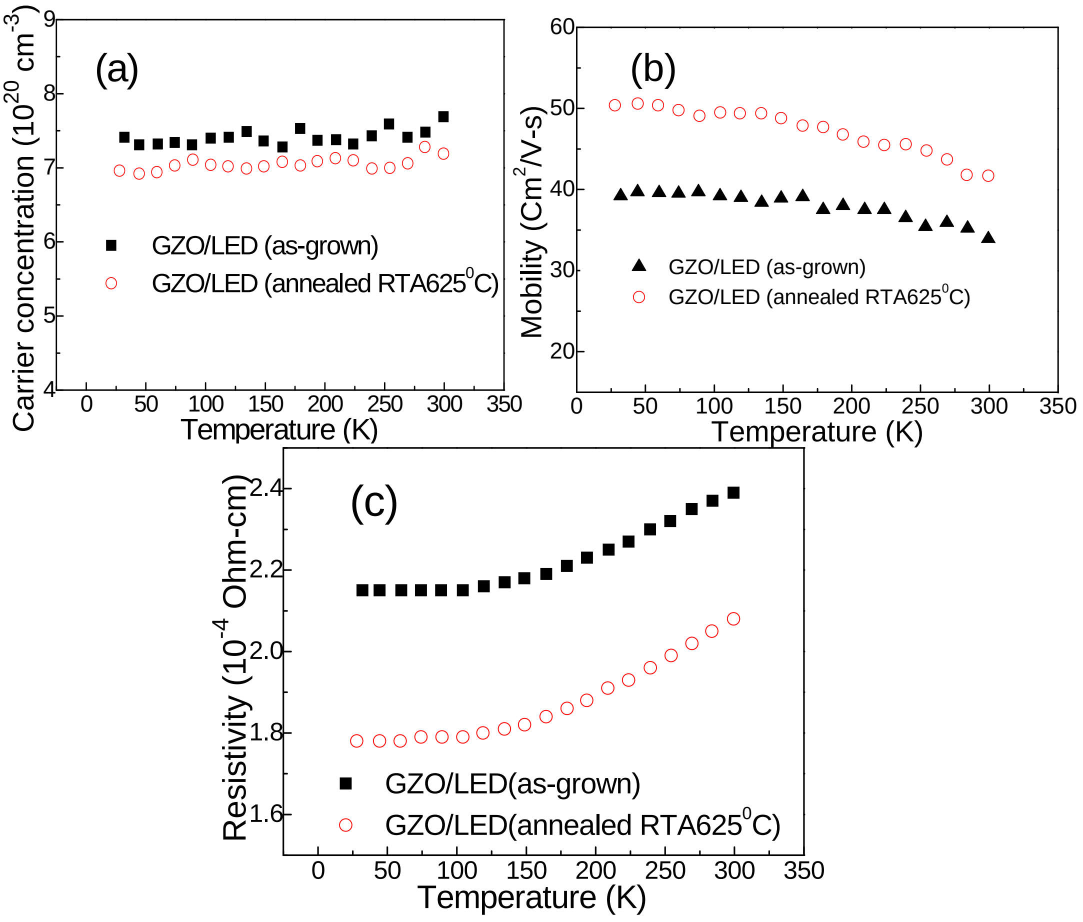

Figure 4.21 Electrical properties measured by temperature-dependent Hall measurements for GZO grown on 400-Torr-1030°C p-GaN template with a thick buffer (5 nm LT ZnO+50 nm HT ZnO). Note: hollow symbols for as-grown sample and solid for annealed sample;

concentrations, mobilities, and resistivities for the as-grown (solid symbols) and annealed (hollow symbols) GZO/400-Torr-1030°C p-GaN template with a thick ZnO buffer (5 nm LT ZnO+50 nm HT ZnO). For the as-grown one here, the effects from the underlying GaNs on the electrical properties are void due to the thicker ZnO buffer. For the annealed one, the electron concentration reduced while mobility increased in the temperature range of 15-330 K as compared with the as-grown one. Although XRD characterizations did not show any obvious difference before and after annealing [see Figure 4.20], the resistivity for the annealed one is much lower than that for the as-grown one [see Figure 4.21 (c)]. In general, the resistivities achieved for GZO/400-Torr p-GaN are much lower than those for GZO/200-Torr p-GaN but are not better than those for GZO grown on a-plane sapphire substrates.

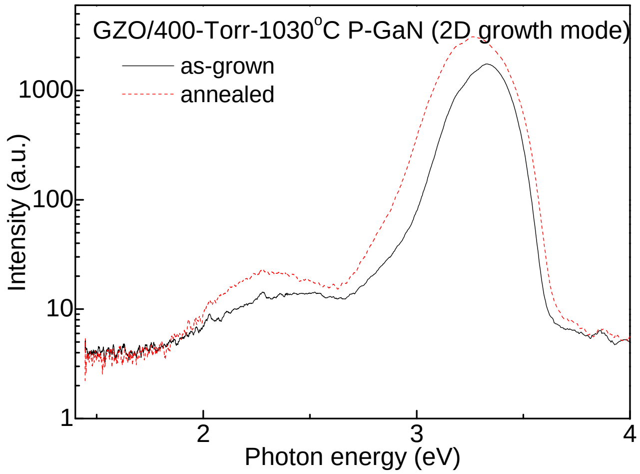

Figure 4.22 PL measurements of as-grown and annealed GZO layers grown on 400-Torr-1030oC p-GaN templates.

Detailed studies regarding the comparisons among GZOs grown on 200-Torr p-GaN and 400-Torr-1030°C p-GaN, and a-plane sapphire substrates can be found elsewhere[110], which are not repeated here. In short, the LED templates have effects on measured as-grown GZO electrical properties, especially the 400-Torr p-GaN grown at substrate temperature of 930°C. This could because there are some pin holes in p-GaN layer and consequently the Hall measurement measures the composite formed by GZO and the underlying thick n-GaN layer. A thicker ZnO buffer (50 nm in this work) or annealing can eliminated the effects from the underlying GaN layers. GZO grown on a rougher GaN surface (200-Torr p-GaN in this work) will lead to a rougher GZO surface which is desired for transparent electrode applications in GaN-LED while GZO grown on a smooth surface (400-Torr p-GaN in this work) will have a smooth surface which is desired for transparent electrode applications in GaN-based VCSEL. It has to be pointed out that the resisitivities of GZO layers grow on both 200-Torr p-GaN and 400-Torr p-GaN are acceptable for electrode applications though there are some differences in their resistivities. The newly grown 400-Torr-1030^{o}C p-GaN has a minor effect on GZO electrical properties due to its higher crystal quality as revealed by the PL measurement as shown in Figure 4.22, where the yellow band emission of GaN is much weaker than that of pervious 400-Torr p-GaN templates grown at substrate temperature of 930^{o}C.

4.3 Summary

In summary for this chapter, I have investigated the applications of highly conductive and transparent GZO layers as transparent electrodes in GaN-based LEDs, which exhibited many advantages over the traditional thin semi-transparent Ni/Au electrodes and the highly conductive and transparent GZOs are promising to replace ITO for practical applications in GaN-based devices. The surface morphologies of GaN were demonstrated to be important in affecting the structural and electrical properties of GZO layers. For applications in LEDs, rougher GZO surface is desired and consequently the rougher GaN template is needed. In contrast, for applications in other GaN-based devices which need smooth surface, smooth GaN surface is needed to grow highly conductive and transparent GZO layers with a smooth surface.

Chapter 5 Electron Transport and Physical Limitation in GZO

The scattering mechanisms governing electron transport will be studied using a comprehensive set of GZO layers grown by MBE mainly on a-plane sapphire substrates with varying oxygen-to-metal-ratio and Ga flux. The analyses were conducted by temperature dependent Hall measurements which were supported by micro structural investigations as well. The physical limitation in GZO conductivity will be discussed in details, which is the main point to be addressed because it will shed light on how to grow GZO layers with desirable mobilities and conductivities.

5.1 Basic theories of scattering mechanisms

As discussed earlier in the Section of 2.5 of Chapter 2, the explanations in electron transport in GZO layers are controversial, it is therefore necessary to briefly introduce the scattering mechanisms first before the analyses are given. These scattering mechanisms include neutral impurity scattering, dislocation scattering, ionized impurity scattering, lattice scattering, and grain boundary scattering which are typically discussed in literature.

5.1.1 Neutral scattering

The neutral scattering limited mobility was first calculated by Erginsoy[111] who scaled the electron scattering at hydrogen atoms to a semiconductor by using the dielectric constant and carrier effective mass, which is

$$\mu_n = \frac{m^* e^3}{A(T) 4\pi\varepsilon\varepsilon_0 \hbar^3 N_n}$$

Equation 2

Here, $A(T)$ is the generally temperature-dependent scattering cross-section factor and N_n is the density of neutral scattering centers. The other symbols have their typical meanings as elsewhere. The detailed discussions regarding the model of neutral scattering can be found elsewhere.[112] Since the shallow donors in ZnO doped with group III elements exhibit ionization energies around about 50 meV[112,113], the concentration of neutral donors at RT is very low and is therefore not considered[112]. It must be pointed out that $A(T)$ was typically treated as a temperature-independent term and a value of 20 was used.[112]

5.1.2 Dislocation scattering

Dislocation scattering is a natural scattering process in polycrystalline materials. However, this process is rarely used in explaining experimental data of carrier transport in polycrystalline semiconductors and especially transparent conducting oxides.[112] Mobility limited by dislocation scattering is given by [112,114,115]

$$\mu_{dis} = \frac{30\sqrt{2\pi}(\varepsilon_0\varepsilon_r)^{3/2} a^2 \sqrt{n}kT}{e^3 f^2 \sqrt{m^*} N_{dis}}$$

Equation 3

where a is the distance between acceptor centers along the dislocation line, f is the occupation rate between 0 and 1 of these acceptors and N_{dis} in the density of dislocations. For ZnO single crystals this scattering process can be neglected since dislocation densities are very low (N_{dis} <300 cm^{-2}). June *et al.*[116] calculated the mobilities of undoped ZnO grown by MBE with the values of N_{dis} =6×10^{8}-3×10^{9} cm^{-2} and n=2.2×10^{17} cm^{-3} and got a RT mobility of ~600-700 cm^{2}/V-s. If the same dislocation density was used for a degenerate GZO layer with an electron concentration above 5×10^{20} cm^{-3}, the RT mobility limited by dislocation scattering would be 30000-35000 cm^{-3} while the mobility limited by dislocation scattering at 10 K would be above 1000 cm^2/V-s. As it will be seen later, the measured mobilities at both 300 K and 10 K are at least 20 times lower than those calculated values and dislocation scattering for heavily doped GZO grown by our MBE system is definitely negligible since TEM characterization revealed the dislocation densities for the GZO layers are below 10^{10}cm^{-2}.

5.1.3 Ionized impurity scattering

Ionized impurity scattering is a very important scattering mechanism in doped materials. According to the Brooks-Herring formula for degenerate materials simplified by Look *et al.*[98], the ionized impurity limited mobility μ_{ii} in partially compensated films can be expressed as

$$\mu_{ii} = \mu_{\max} \frac{1-K}{1+K}$$

Equation 4

where K is the compensation ratio and μ_{max} represents the maximum attainable mobility limited by ionized impurity scattering (mobility at 0 K) in samples with no compensation. μ_{max} as a function of electron concentration n is given in the following equation with Z being the ionization charge in units of e and ε_0 being the dielectric constant.

$$\mu_{\max} = \frac{24\pi^3\varepsilon_0^2\hbar^3}{Z^2e^3m^{*2}} \frac{1}{\ln[1+y(n)] - \frac{\dot{y}(n)}{1+y(n)}} \quad \text{with } y(n) = \frac{3^{1/3}4\pi^{8/3}\varepsilon_0 h^2 n^{1/3}}{e^2 m^*}$$

Equation 5

As seen above for degenerate materials, ionized impurity limited mobility is temperature-independent and compensation in TCO should be minimized since the reduced compensation not only increases its donor concentration but also increases its mobility.

5.1.4 Lattice scattering

In ZnO, lattice scattering includes acoustic phonon scattering, polar-optical phonon scattering, and piezoelectric scattering.

Acoustic phonon scattering is a lattice deformation scattering due to a local energetic shift of the band edges originating from acoustical phonons. The acoustical lattice mode Hall mobility is:[117]

$$\mu_D = r_{Hac} \frac{\sqrt{8\pi}}{3} \frac{e\hbar^4 C_l}{E_1^2 \sqrt{(m^*)^5 (KT)^3}}$$

Equation 6

where C_l is the longitudinal elastic constant, E_1 is the deformation potential (energy shift of the conduction band per unit dilation), r_{Hac} is the Hall coefficient for acoustic phonon scattering[115] which is 3π/8. The deformation potential E_1 is not very well known for ZnO. In literature, its value scattered (1.4 eV[118], 3.8 eV[116,119], 15 eV[120]and 31.4 eV[121]). For the calculation of the overall carrier scattering in ZnO this is not very important since other scattering mechanisms, especially polar-optical and piezoelectric scattering, are dominant.[122] It must be pointed out that recent papers used the deformation energy of 3.8 eV for ZnO, which could be more accurate.

Piezoelectric scattering occurs only in piezoelectric materials, i.e., in crystals without inversion symmetry, and is caused by the electric field associated with acoustical phonons. The piezoelectrically limited mobility is given as:[112]

$$\mu_p = r_{Hpie}\frac{16\sqrt{2\pi}}{3}\frac{\hbar^2}{e\sqrt{m^{*3}}}\frac{\varepsilon_0\varepsilon_r}{P_{\perp,\mathrm{II}}{}^2\sqrt{kT}}$$

Equation 7

where r_{Hpie} is the Hall coefficient and is equal to $45\pi/128$. $P_{\perp,\mathrm{II}}$ is the averaged piezoelectric electro-mechanical coupling coefficients for electrical transport perpendicular or parallel to the c axis. As seen later, piezoelectric scattering is also not important.

Polar optical phonon (POP) scattering is important in polar materials at temperature near or above room temperature (RT). As calculated by Jung *et al.* [116] for high quality undoped ZnO grown by MBE, the effect of POP scattering is much stronger than other scattering mechanisms, including deformation potential scattering, piezoelectric scattering, and dislocation scattering. The temperature dependent mobility limited by POP scattering is given by [116,123].

$$\mu_{pop}[\frac{cm^2}{V\cdot s}] = 0.199\times(T/300)^{1/2}\times(\frac{e}{e^*})^2\times(m_0/m^*)^{3/2}\times(10^{22}M[g])$$
$$\times(10^{23}v_a[cm^3])\times(10^{-13}\omega[s^{-1}])\times(e^{\hbar\omega/k_BT}-1)\times G(\hbar\omega/k_BT)$$

Equation 8

where e^* is the Callen effective charge, M is the reduced mass, V_a is the volume of the unit cell, and m^* is the effective mass of electron. The Ehrenreich's function G ($\hbar\omega/k_BT$) accounting for the screening effect[123] is a slowly varying function of temperature T, with $\hbar\omega$ being the LO phonon energy, which is 72 meV in the case of ZnO. Note that k_B is Boltzmann constant. For degenerate materials, when the Fermi level is located deeply in the conduction band, the POP scattering may become even more important because of increase in the electron effective mass caused by nonparabolicity of the conduction band. As shown later, the strong effect of POP scattering makes both acoustic phonon scattering and piezoelectric scattering negligible.

5.1.5 Grain boundary scattering

Most of the available models for grain boundary-limited mobility refer to the works by Petritz *et al.*[124], Tarng *et al.*[125], and Seto *et al.*[57] These theories are based on the model of a barrier induced by charges trapped by states at grain boundaries where there are many defects due to the incomplete chemical bonds. There are typically three different formulas for grain boundary scattering based on this theory in the literature. The one based on thermionic emission from traps on the grain boundaries was developed by Seto *et al.*[57] for non-degenerate materials which has the form

$$\mu_g = Lq(2\pi m^* k_B T)^{-1/2} \exp(-\Phi_b / k_B T) \text{ or } \ln(\mu_g T^{1/2}) \sim -T^{-1}$$

Equation 9

This model is widely cited but is not suitable for degenerate materials. Note that L is the grain size and k_B is Boltzmann constant. As pointed out by Ellmer *et al.*,[59] the Seto model extended by Werner[126], as shown below, can be used to describe the temperature-dependent mobility at lower carrier concentration.

$$\mu = \frac{\mu_0 \mu_{eff}}{\mu_0 + \mu_{eff}} = \frac{\mu_0 \mu_{grain}}{\mu_0 + \mu_{grain} \exp(-\frac{\phi_b - \frac{\Delta\phi_b^2}{2KT}}{KT})} \exp(-\frac{\phi_b - \frac{\Delta\phi_b^2}{2KT}}{KT})$$

Equation 10

where μ_0 is temperature independent, μ_{eff} is temperature dependent, and μ_{grain} is the mobility inside the grain. That developed by Tarng *et al.*[125] based on the assumption of Schottky thermionic emission and then followed by Bruneaux *et al.*[58] for degenerate materials is

$\boldsymbol{\mu_g = BT\exp(-\Phi_a/k_BT)}$ or $\ln(\mu_g / T) \sim -T^{-1}$

Equation 11.

Note that B is a constant related to the grain size and electron concentration and Φ_a is the activation energy given by $\Phi_b-(E_F-E_C)$. If we assume Schottky barrier, the barrier should be high for which a value of 0.5eV was given by Tarng *et al.*[125] for polycrystalline-Si. That probably first used by Zhang *et al.*[127] for grain boundary scattering is $\mu_g=BT^{-1}\exp(-\Phi_a/k_BT)$ or $\ln(\mu_gT)\sim-T^{-1}$, which has been widely used in the literature.[64,65] With my careful examination, reference 127 directly refers to the work by Bruneaux et al.,[58] in which $\mu_g=BT\exp(-\Phi_a/k_BT)$ or $\ln(\mu_g/T)\sim-T^{-1}$. However, the temperature dependence of mobility appears in a different form ($\ln(\mu_gT)\sim-T^{-1}$) from the original work by Bruneaux et al. [58] Therefore, the expression used by Zhang *et al.*[127] is possibly problematic since it is not physically meaningful and they did not mention its inconsistency with the original reference.

When considering grain boundary scattering, we must consider two other physical phenomena. Although they are different in formulism, both they are temperature independent. The first one is electron reflection by grain boundaries, which gives the strength of the potential and thickness of the grain boundary. The model for grain boundary scattering based on reflection can be found elsewhere.[59,128,129] The second phenomenon is quantum mechanical tunnelling. If we consider a simple rectangular barrier of height U and width W, the tunnelling probability[130] can be expressed as

$$T_{tunn} \approx \frac{16E(U-E)}{U^2}\exp(-2\sqrt{\frac{2m^*(U-E)}{\hbar^2}}W)$$

Equation 12

Following Holm[131] for a rectangular barrier of height E_B and width l_2, when a very small applied voltage V is across a barrier the conductivity by the tunnel effect σ_{tun} can be expressed as[132]

$$\sigma_{tun} = [Lq^2(2m^*E_B)^{1/2}/(h^2 l_2)]\exp[-4\pi l_2(2m^*E_B)^{1/2}/h]$$

Equation 13

where L and h are the grain size and Planck constant, respectively. This equation indicates that, for a given free-carrier concentration, the mobility ($\mu=\sigma/qn$) limited by the tunnel effect is temperature independent but is proportional to the grain size. It should be mentioned, however, that while pure tunnelling is temperature independent in and of itself, but the effective tunnelling-governed electron flow across grain boundaries is temperature-dependent, because the energy distribution of electrons is temperature dependent and electrons with different energies experience barriers of different heights. The last consideration dramatically complicates the theoretical study of grain-boundary scattering for the tunnelling limit (low barriers). Recently, Look et al.[98,119] provided a formula of grain-boundary-scattering limited mobility for degenerate TCOs, which is temperature-independent too and is given as:

$$\mu_g = \frac{e}{m^*}\tau_g = \frac{d/C}{v_{Fermi}(n)} = \frac{e}{\hbar}\frac{d/C}{(3\pi^2 n)^{1/3}}$$

Equation 14

where d is the film thickness, C is a fitting factor, v_{Fermi} is the Fermi velocity for a degenerate material. It must be pointed out that the fitting factor C is not well known, which varied from paper to paper. For example, ZnO layers grown on SiO_2 by PLD produced a C value of 4 [98] while PLD grown ZnO layers on sapphire substrates produced a C value of 2.5[133]. Look et al.[119]

concluded that although there are some fluctuations in *C* values, the mobility limited by grain boundary scattering for heavily dope GZOs must be very high (527 $cm^2/V\cdot s$ for *C*=2.5 and $n=1.1\times10^{20}$ cm^{-3}) and can be neglected. Note that based on this theory, for layers with smaller n but still degenerate, the mobility limited by grain boundary scattering should be higher since it is inversely proportional to carrier concentration.

5.2 Results and analyses

The detailed studies of electron transport in two sets of GZO samples were performed using TDH measurements in the van der Pauw configuration.

In the first series, we compared electrical properties of the samples grown under metal-rich and oxygen-rich conditions with T_{Ga} = 600^oC. Note that the GZO layers discussed in the first series are actually the GZO layers grown for investigation of effects of oxygen pressures on GZO properties, and consequently the details which can be found in Chapter 3 will not be repeated here.

In the second series, we varied Ga flux by changing T_{Ga} from 425 to 600^oC, while oxygen pressure was kept at 4.5×10^{-6} Torr (metal-rich conditions). Note that the GZO layers discussed in the second series are actually the GZO layers grown for investigation of effects of Ga fluxes on GZO properties, and consequently the details which can also be found in Chapter 3 will not be repeated here.

Rapid thermal annealing (RTA) at a temperature of ~600^oC in nitrogen environment for 3 mins was used for some GZO layers to improve their properties. The structural properties of the GZO layers were characterized by XRD. For the representatives of GZO layers, STEM/TEM, electron energy loss spectroscopy (EELS), and energy dispersive X-ray spectroscopy (EDX) measurements were done on cross-section specimens using an aberration-corrected STEM microscope Titan S-Twin operated at 200 kV. The TEM/STEM investigations were focused on characterization of structural defects that could be responsible for carrier scattering and limitation of electron mobility in GZO.

5.2.1 Electron transport in GZO grown under oxygen-rich and metal-rich conditions

First, the general relationship between the microstructure of GZO layers grown under various reactive-oxygen-to-metal ratios and their transport properties at room temperature (RT) have been studied. Then, the electron concentration and mobility were investigated in order to gain insight into electron scattering mechanisms governing the transport in GZO.

5.2.1.1 Correlation between crystal structure and room-temperature electron mobility in GZO

STEM and TEM studies revealed that the microstructure of GZO layers strongly depend on P_{O2},. *i.e.*, oxygen-to-metal ratio. Inclined grain boundaries (12^{o} from the polar *c*-direction indicated by the two arrows) are the dominating extended structural defects in the GZO layers grown under oxygen-rich growth conditions [Figure 5.1 (a)]. It was conjectured that they should have strong polar field in ZnO because the polarization vector pointing into the *c*-direction will have a substantial projection on them and as a consequence, coulombic interaction between free carriers and grain boundaries will reduce electron mobility. The grain size in these GZO films varies in the range from 10 to 30 nm. Unlike the GZO layers grown under oxygen-rich conditions, the GZO films grown on a-sapphire under metal-rich growth condition have high crystal quality but albeit with some porosity and porous GZO grows on top of the non-porous ZnO seed layer. Investigation of the nature of pores revealed that these defects form due to nucleation of multiple open-core dislocations in GZO layer. Open-core dislocations have a minor effect on the width of the XRD rocking curves. However, the high concentration of pores masks the position of low-angle grain boundaries in STEM images and consequently makes it difficult to use STEM technique to visualize the grain boundaries by varying electron channelling effect for grains oriented at different angles with respect to the probe direction.

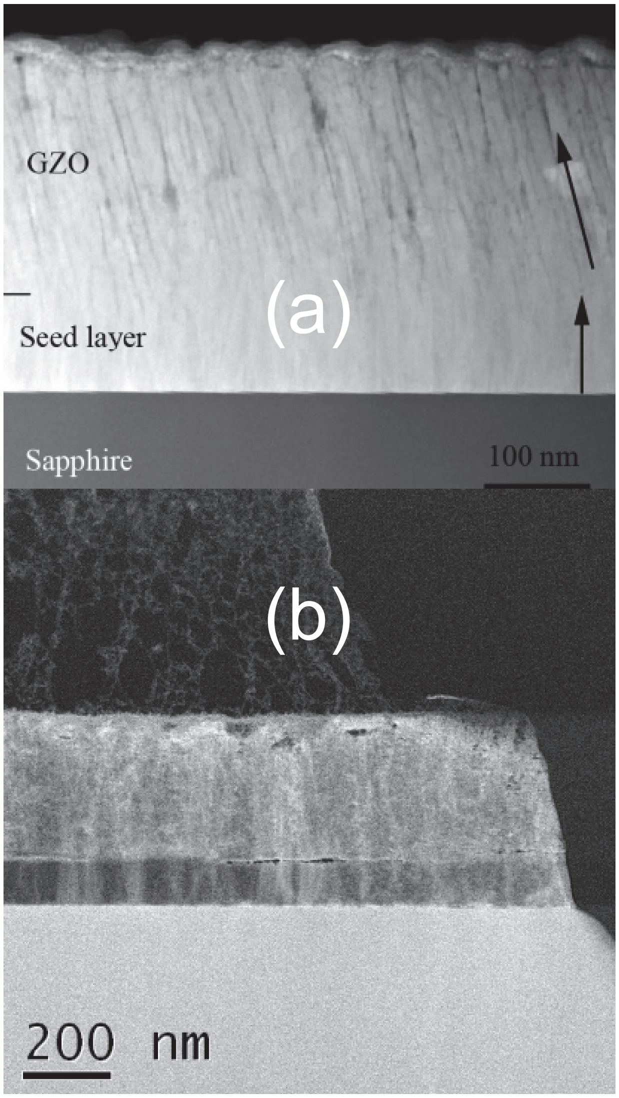

Figure 5.1 (a) A representative of STEM images of GZO layers grown under oxygen-rich conditions and (b) Low angle annual dark field (LAADF) TEM image of a representative GZO layer grown under metal-rich conditions (GZO-1 as shown later). Note: arrows indicating inclined grain boundaries (12^o from the polar *c*-direction).

In order to gain accurate information regarding the grain boundaries and grain sizes for GZO layers grown under metal-rich conditions, low angle annual dark field (LAADF) technique was employed. Also the special care was taken about specimen preparation in order to minimize the effect of ion milling on the sample microstructure. As shown in Figure 5.1 (b), the low-angle grain boundaries in the GZO layer grown under metal-rich conditions mainly propagate from the ZnO seed layer normally to the substrate plane (parallel to the polar *c*-direction), which is totally different from that for GZO layers grown under oxygen-rich conditions as discussed above [Figure 5.1 (a)]. Therefore, the grain boundaries in GZO grown under metal-rich conditions are parallel to the *c*-direction that results in much smaller polarization field at the interfaces. The average grain sizes in these layers were determined to vary from 30 nm to 50 nm, which are larger than those for GZO layers grown under oxygen-rich conditions. Owing to the larger grain size and the smaller charge accumulation on low-angle grain boundaries, the mobility limited by grain boundaries in GZO layers grown under metal-rich conditions should be higher than that in GZO layers grown under oxygen-rich conditions.

Figure 5.2 shows the Hall electron mobility versus either electron concentration [Figure 5.2 (a)] or grain size [Figure 5.2 (b)] for the as-grown and annealed GZO layers, for which carrier concentrations varied from 3×10^{20} to 12×10^{20} cm^{-3}. Note that the grain size was extracted from the (0002) XRD rocking curves using the Scherrer equation[134] except the two points with error bars (one for the GZO layer grown under metal-rich conditions and the other one for the GZO layer grown under oxygen-rich conditions), for which grain sizes were determined from STEM/TEM cross-section measurements. The error bar in the mobility is due to the spatial non-uniformity of electrical properties over the wafer. As seen from Figure 5.2 (a), there is no clear correlation between the electron mobility and the concentration. However, the mobility *vs.* grain size plot reveals a nearly linear relationship between these two parameters. At a first glance, the data appear to indicate as if mainly the grain boundary scattering limits the electron transport. However, one should keep in mind that the full picture is quite complicated, which was caused by the differences in oxygen pressures during growth and film thicknesses, *etc.* The detailed discussion regarding the effects of oxygen pressures, film thickness, and annealing on GZO electrical properties as well as grain sizes can be found in Chapter 3. In short, annealing in nitrogen environment significantly improved the electrical properties of GZO grown under oxygen-rich conditions while only minor increase in mobility and electron concentration observed for GZO grown under metal-rich conditions. The difference in the annealing behavior is tentatively attributed to the lower concentration of compensating defects in GZO grown under metal-rich conditions.[100] For highly conductive GZO with electrical properties comparable to our best GZO grown under metal-rich conditions, Look *et al.*[119] reported the existence of Zn-vacancy-related acceptors causing self-compensation based on positron annihilation measurements and secondary-ion mass spectroscopy (SIMS). This seems consistent with the observation of slight increase in both the electron concentration and mobility upon annealing for one GZO layer grown under metal-rich conditions ($n=8.33\times10^{20}$ cm^{-3} and $\mu=36.7$ $cm^2/V\cdot s$ in the as-grown sample *vs.* $n=9.23\times10^{20}$ cm^{-3}, $\mu=42.4$ $cm^2/V\cdot s$ in the annealed one). Note that the annealed sample is actually GZO-1 which will be discussed in more details later. Since the grain size remains virtually unchanged (~25 nm) before and after annealing as shown in Figure 5.2, the increase in both the electron concentration and mobility is unlikely due to the reduced effect of grain boundary scattering but possibly due to the decrease in concentration of Zn-vacancy defects, which is consistent with the increased carrier concentration upon annealing. It must be reiterated that the concentration of compensating defects in our GZO layers grown under

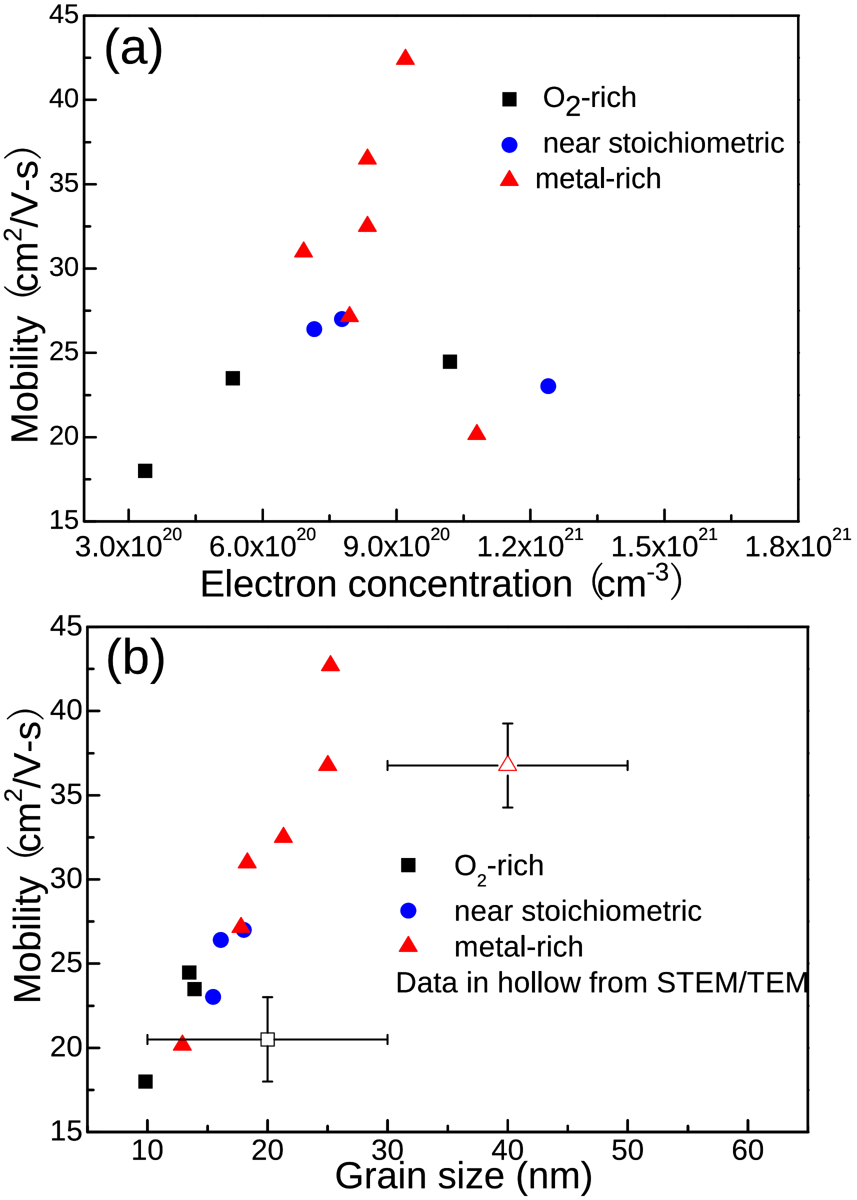

Figure 5.2 Hall mobilities *vs.* (a) electron concentrations and (b) grain sizes for annealed GZO layers with different thicknesses grown under oxygen-rich conditions (squares), annealed GZO layers with different thicknesses grown under near stoichiometric conditions (circles), and as-grown GZO layers with different thicknesses grown under metal-rich conditions (triangles). [Symbols in hollow from STEM/TEM for comparisons; an annealed GZO grown under metal-rich condition (highest μ) was also added to see RTA treatment effect].

oxygen-rich conditions should be much higher than that in GZO layers grown under metal-rich conditions, resulting in a serious compensation in GZO grown under oxygen-rich conditions.[100] As discussed earlier, grain boundary scattering governed by quantum-mechanical tunneling is virtually temperature-independent, which is the same as that of ionized impurity scattering in the degenerate material. Therefore, the large variation in electron concentrations from 3×10^{20} cm^{-3} to 9×10^{20} $cm^{-3}$and/or in growth conditions could mask the real phenomenon and lead to a wrong conclusion.

5.2.1.2 Electron transport in GZO grown under oxygen-rich and metal-rich conditions

The electron transport was studied in greater details using TDH measurements in the van der Pauw configuration for 4 selected GZO layers. Table 5.1 summarizes the growth details and sample characteristics.

Table 5.1 Basic information for 4 selected GZO layers used for TDH measurements

No	Thickness (nm)	P_{O2} (10^{-6} Torr)	ZnO buffer Thickness (nm)	Annealed?	FWHM of (0002) ZnO (degree)	RT μ ($cm^2/V\cdot s$)	*n* ($10^{20}cm^{-3}$)
GZO-1	290	4.5	~100	Yes	0.34	42.4	9.2
GZO-2	523	4.5	~ 10	No	0.39	32.5	8.35
GZO-3	745	15	~ 10	Yes	0.88	18.2	3.37
GZO-4	745	15	~ 10	No	1.15	7.5	0.2

Figure 5.3 clearly shows that the carrier concentration is temperature independent for all four samples, indicating their degeneracy. It is worth nothing that the layers with higher carrier concentrations also have higher mobilities in the entire temperature range investigated (the order is GZO-1, GZO-2, GZO-3, and GZO-4). GZO-4 has the lowest carrier concentration of around 2×10^{19} cm^{-3} and the lowest mobility of 5-7 $cm^2/V\cdot s$ for temperatures ranging from 15 to 330 K. Upon annealing in nitrogen, this layer (denoted as GZO-3 in Table 5.1) exhibits much higher carrier concentration and mobility of $\sim3.4\times10^{20}$ cm^{-3} and 18-to-21 $cm^2/V\cdot s$, respectively, but

these figures are still well below those for the GZO layers grown under metal-rich conditions (GZO-1 and 2). GZO-1 has a slightly higher carrier concentration and mobility possibly because of the thicker undoped ZnO buffer layer grown at 600^{o}C and/or possibly the lower concentration of defect-related compensating acceptors as compared to GZO-2. Note that the thicker ZnO buffer layer grown at 600^{o}C enhances the structural perfection giving rise to a slightly narrower FWHM of XRD (0002) peak. From the temperature dependent resistivities (not shown here), GZO-1 and GZO-2 showed the metallic behavior. The lowest resistivity achieved at low temperatures is ~1.3×10^{-4} Ohm·cm. GZO-3 exhibited a similar temperature dependence as GZO-1 and GZO-2 but its resistivity is much higher (~9.2×10^{-4} Ohm·cm), while GZO-4 showed a semiconductor-like behavior (negative temperature coefficient of resistivity).

I have fitted the measured temperature dependent mobilities for samples GZO 1-4 as shown in Figure 5.3 (b). The un-annealed GZO layer grown under oxygen-rich conditions (GZO-4 sample with the lowest carrier concentration of 2×10^{19} cm^{-3} among the samples considered in this Section) exhibits a μ~$T^{0.24}$ temperature dependence [Figure 5.3 (b)]. Temperature-activated mobility of GZO-4 can be considered as a characteristic of grain boundary scattering based on thermionic effect[57,59], representing a higher barrier at grain boundaries in the material with lower electron concentration.

Samples GZO-1, GZO-2, and GZO-3 show the temperature dependences of mobility which drastically different from that for the GZO 4 layer. Their mobilities initially increase when temperature decreases down to ~150 K. At lower temperatures (LT), mobility in these samples becomes virtually invariant. The temperature dependent mobilities measured in GZO-1, GZO-2, and GZO-3 were theoretically fitted based on Matthiessen’s rule as $1/\mu = 1/\mu_{\mathrm{Ti}}+1/\mu_{\mathrm{pop}},$ where μ_{Ti} is a constant representing temperature-independent scattering events, which include ionized impurity scattering μ_{ii} and grain boundary scattering μ_{gb} governed by the tunnel effect, and μ_{pop} is the temperature dependent POP scattering (see Figure 5.3 (b)). The results of fitting are summarized in Table 5.2.

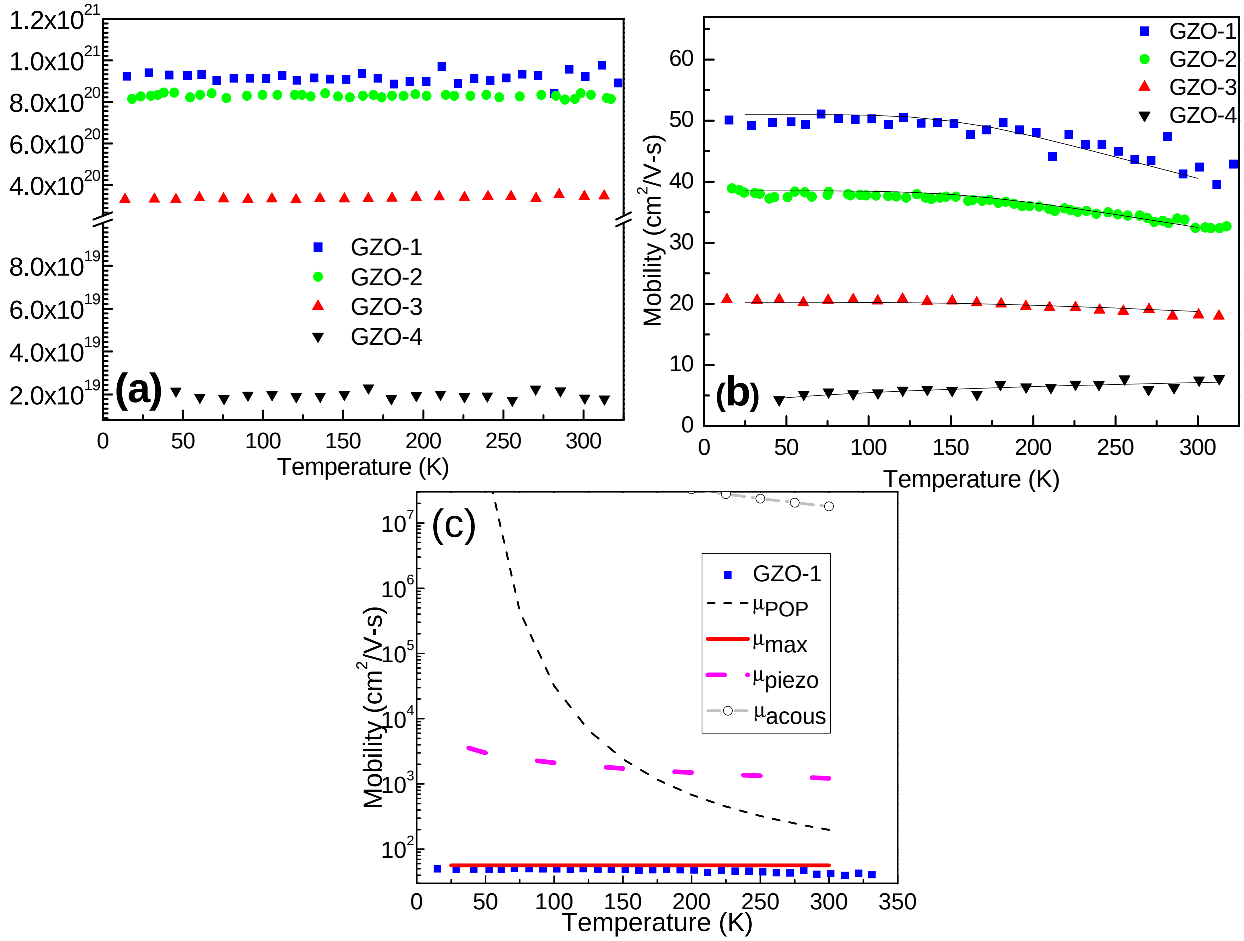

Figure 5.3 Temperature dependence of a) carrier concentration and b) mobility for GZO-1, GZO-2, GZO-3 and GZO-4 (From top to bottom in both). Note: solid lines in (b) are fittings. For GZO 1-3, the fittings used a constant for mobility limited by temperature-independent scatterings, and polar optical phonon scattering for temperature-dependent scattering while for GZO-4, it was fitted with power dependence. (c) effects of different scattering mechanisms in GZO-1 indicating ionized impurity scattering and POP scattering is the first and the second dominant mechanisms limiting the RT mobility

Table 5.2 Results of fitting to the temperature-dependent mobility for GZO 1-3 based on Matthiessen's rule $1/\mu = 1/\mu_{Ti}+1/\mu_{pop.}$

No	μ ($cm^2/V\cdot s$)	μ_{Ti} ($cm^2/V\cdot s$)	μ_{max} ($cm^2/V\cdot s$)	RT μ_{pop} ($cm^2/V\cdot s$)
GZO-1	~40.6	51	56.7	198
GZO-2	~32.5	38.5	61.5	210
GZO-3	~18.7	20.3	87.5	250

Using the values equal to ~$0.39m_0$, $0.37m_0$, and $0.33m_0$ measured by Ruske *et al*.[62] for electron effective mass in ZnO-based TCO with carrier concentrations similar to those in the GZO 1, GZO 2, and GZO 3 layers, based on Equation 8 I calculated room temperature (RT) μ_{pop} to be ~198, 210, and 250 $cm^2/V\cdot s$ in GZOs 1 to 3, respectively. (Note: e^*/e=0.62, M=2.135×10^{-23} g, V_a =2.38×10^{-23} cm^3 in Equation 8 for POP scattering) The calculated values for POP scattering-limited mobility at RT are comparable to the reported mobility limited by lattice scattering (~200 $cm^2/V\cdot s$[59]) and consequently demonstrate that other phonon scatterings which are temperature-dependent are negligible compared with POP scattering in ZnO due to its highly polar nature as discussed earlier. Note that the mobility limited by other phonon scatterings including both acoustic phonon scattering and especially piezoelectric scattering must be one order of magnitude higher than that by POP scattering. Otherwise, the fittings as shown in Figure 5.3 cannot be done. Since other mechanisms used in the simulations are to a first extent temperature-independent in these very highly doped samples, POP scattering is suggested to be the mechanism responsible for the temperature-dependence, which further reduces the mobility for GZO 1-3 at T>150 K.

Based on the Brooks-Herring formula for degenerate materials, the μ_{max} (Equation 5) representing the maximum mobility limited by ionized impurity scattering with no compensation (mobility at 0 K) were calculated to be 56.7, 61.5, and 87.5 cm^2/V·s for GZO 1-to-3 layers, respectively. Note that the dielectric constant ε_0 and ionization charge Z are 8.12 and 1.[98] However, the simulated mobilities limited by temperature-independent scattering events are 51, 39, and 20 cm^2/V·s for GZO 1-to-3, respectively. Based on Matthiessen's rule, the mobilities limited by both compensation if present and grain boundary scattering based on tunnelling can be calculated as 507.3, 106.6, and 27.6 cm^2/V·s for GZO 1-to-3, respectively. We should mention here that it is extremely difficult to separate out the contribution from grain-boundary scattering governed by tunnelling and compensation.

If Equation 14 is used to calculate the mobility limited by grain boundary scattering, the mobility is 585 cm^2/V·s for C=2.5 and 366 cm^2/V·s for C=4, which are close to the value of 507.3 cm^2/V·s and could indicate that there is almost no compensation and other temperature-independent scattering in GZO-1. The mobility of 507.3 cm^2/V·s limited by grain boundary scattering and compensation if compensation present in GZO-1 is ~9 times higher than the mobility limited by ionized impurity scattering in the whole investigated temperature range and consequently the grain boundary scattering and compensation have a relatively minor effect and thus both can be neglected. In this case, ionized impurity scattering and POP scattering is the first and the second dominant mechanisms limiting the RT mobility, respectively. As seen in Figure 5.3 (c) other scatterings have very minor effects limiting the mobilities for GZO-1 and can be neglected. For GZO-2, the calculated mobilities based on Equation 14 are 1090 cm^2/V·s for C=2.5 and 681 cm^2/V·s for C=4, which are much higher than the value of 106.6 cm^2/V·s and could indicate that compensation has a stronger effect than grain boundary scattering in limiting the mobility. Note that the uncertainty of the C value could lead to a wrong conclusion too although the possibility is small. However, it is really not necessary to separate them because the mobility set by grain boundary scattering based on tunnelling and compensation if present (106.6 cm^2/V·s) is larger by a factor of ~1.73 times higher than the mobility limited by ionized impurity scattering (61.5 cm^2/V·s) in the whole temperature range investigated. The stronger effect of grain boundary scattering and compensation in GZO-2 is consistent with its slightly larger rocking-curve width (0.39^o *vs.* 0.34^o) and slightly lower electron concentration of ~8.4×10^{20} cm^{-3}, indicating a somewhat smaller grain size and, plausibly, a higher compensation ratio as well. By comparing GZO-2 with GZO-1, the probability of existence of compensation caused by defects such as Zn-vacancy acceptors is greater. If we assume no compensation in GZO-2, the grain boundary scattering would have a larger effect than POP scattering at RT (106.6 vs. 210 cm^2/V·s) although the assumption could be not right because it is not consistent with the results from Equation 14. However, no matter which one is stronger, ionized impurity scattering is still the first dominant mechanisms limiting the mobility in the entire temperature range of 15-330 K, which effect is stronger than that from all other scatterings. The grain boundary scattering may compete with POP scattering in the practically important temperature range around RT depending on the GZO film quality (the higher the structural quality, the smaller the contribution of grain boundaries).

For GZO-3, the mobility limited by the grain boundary scattering and compensation (27.6 cm^2/V·s) is much lower than that limited by ionized impurity scattering (87.5 cm^2/V·s), which is consistent with the predicted higher compensation by Demchenko *et al.*[100] and smaller grain size revealed by STEM and XRD characterization in the GZO layers grown under oxygen-rich conditions. However, it is difficult to delineate and quantify the contributions from grain boundary scattering and compensation in GZO-3. But it is obvious that, when the grain size becomes smaller and electron concentration reduces, the effect of grain boundary scattering becomes stronger, while the contribution of POP scattering weakens. To make the situation worse, the donor compensation provides a "positive feedback" to the grain boundary scattering. For a given Ga concentration and a given average grain size, the higher the compensation is the lower the Fermi energy is, *i.e.* the higher the barriers are and consequently the stronger the grain boundary scattering is. Note that the smaller grain sizes for GZO grown under oxygen-rich conditions are definitely caused by excess oxygen during growth compared with that for GZO grown under metal-rich conditions. In other words, the smaller the grain sizes are, the larger the volume ratio of grain boundaries is and consequently more defects could be trapped in the boundary regions. As the measured electron concentration is much lower in GZO grown under oxygen-rich conditions, compensation caused by the increased defects is more likely. Wong *et al.*[135] reported that excess oxygen will lead to compensation while more excess oxygen will lead to structural changes which increase the grain boundary scattering. This reasoning is consistent with our observations and analysis. In short, metal-rich conditions instead of oxygen-rich conditions are the must to achieve high mobility and high electron concentration in GZO. However, as suggested by data presented in Figure 5.2, in order to push the mobility to the value limited by scattering only on ionized impurities and polar optical phonons, large grain size is required even for the material grown under metal-rich conditions.

5.2.2 Effect of Ga flux via changing Ga cell temperature (T_{Ga})

Table 5.3 lists the growth conditions and major structural and electric properties of GZO layers discussed in this Section. These samples were grown under metal-rich conditions (P_{O2}=4.5×10^{-6} Torr) with varying Ga cell temperatures. As seen from the table, when T_{Ga} was increased from 425 to 600 ^{o}C, the carrier concentration increases from ~6×10^{18} cm^{-3} to 9×10^{20} cm^{-3}. RT mobility first increases from ~34 to 40 cm^{2}/V·s, when T_{Ga} was increased from 425 to 450 ^{o}C and then the RT mobility remains virtually unchanged, when T_{Ga} was further increased to

600 ^{o}C. The detailed information can be found in Chapter 3.

Table 5.3 Basic information for 3 selected GZO layers used for TDH measurements

No	Thickness (nm)	T_{Ga} (^{o}C)	ZnO buffer Thickness (nm)	Annealed?	FWHM of (0002) ZnO (degree)	RT μ ($cm^2/V\cdot s$)	n ($10^{20}cm^{-3}$)
GZO-1	290	600	~100	Yes	0.34	42.4	9.2
GZO-5	350	450	~ 10	No	0.325	40.1	0.55
GZO-6	290	425	~ 10	No	0.319	34.3	0.06

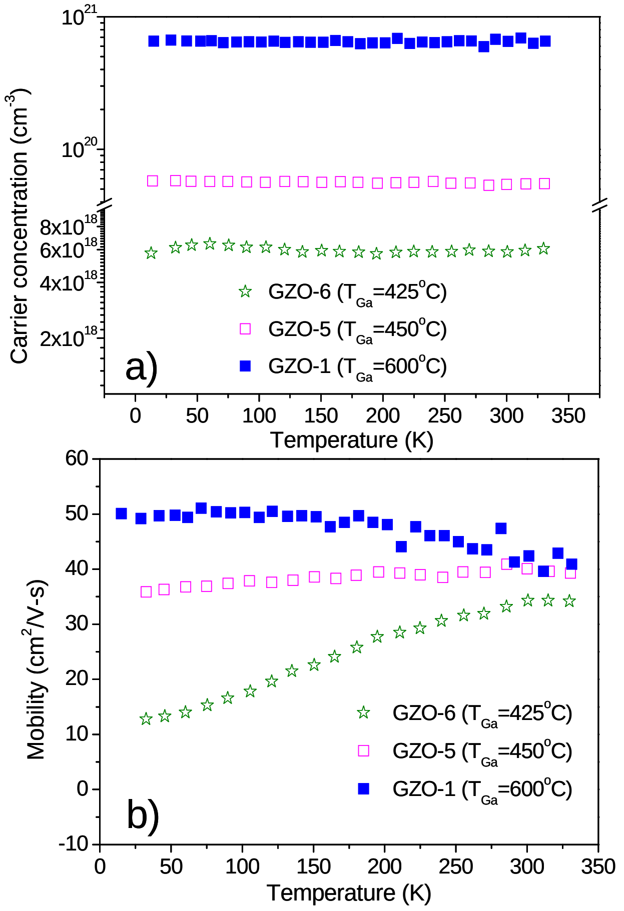

Figure 5.4 Temperature dependence of a) carrier concentration and b) mobility for GZO-1, GZO-5, and GZO-6.

The results of TDH measurements for 3 selected GZO layers listed in Table 5.3 are shown in Figure 5.4, which are also given in Figure 3.20. Figure 5.4 clearly shows that, as the electron concentration reduces, the signature of the grain-boundary scattering governed by the thermionic effect (mobility increases with temperature) emerges in the temperature dependence of mobility. As the grain boundary scattering governed by the quantum tunnelling (temperature-independent) contributes more for GZO with higher electron concentration, the temperature dependence for GZO-5 is much weaker than that for GZO-6. GZO-6 exhibits a $\mu \sim T^{0.62}$ temperature dependence. While in GZO-1, only grain boundary scattering governed by quantum tunnelling contributes and therefore it is temperature-independent. Note that we have previously demonstrated that grain boundary scattering is negligible in GZO-1. It must be pointed out that dislocation scattering has a similar temperature-dependence as that for grain boundary scattering governed by the thermionic effect but the mobility limited by dislocation scattering is much higher (at least one order of magnitude higher) than the experimental data based on Equation 3. Dislocation scattering is thereby not considered here. Since GZO-1, GZO-5, and GZO-6 have comparable FWHMs of (002) XRD rocking curves and thus comparable grain sizes, the change in the behavior of temperature-dependent mobility can be mainly attributed to different barrier heights in the layers with different electron concentrations. The barrier heights for GZO-5 and GZO-6 were estimated using Equation 10 based on the Seto[57] model extended by Werner[126] to be 0.3 meV and 8 meV (see Figure 5.5), respectively. Although the values of barrier heights, especially the one for GZO-5, may not be very accurate, it offers a viable explanation for the observed evolution of temperature dependences of mobility with electron concentration. Note that for fittings, a constant barrier height was assumed for simplicity, which caused some unsatisfied results for GZO-6 when T is below 75 K. This is because the value of KT becomes smaller at lower temperature which is comparable to the change in the barrier height and consequently the change in barrier height cannot be neglected for T below 75 K.

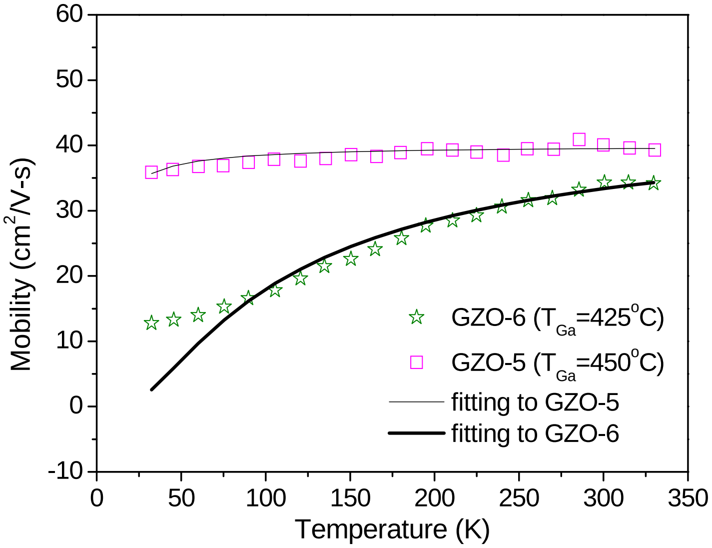

Figure 5.5 Fittings to the temperature dependent mobility for GZO 5 and 6 with grain barrier scattering with the assumption of a constant barrier.

One interesting observation is that the GZO-5 layer having a slightly higher carrier concentration than that in GZO-4 shows similar temperature dependence of mobility to that of GZO-4 [compare Figure 5.4 (b) and Figure 5.3 (b)] but with a much higher mobility value within the entire temperature range studied. The narrower rocking curve, by a factor of ~3.5, and the expected lower compensation ratio in GZO-5 grown under metal-rich conditions are consistent with this observation and the above discussion, indicating that the mobility limited by grain boundary scattering and compensation in GZO-5 grown under metal-rich conditions should be higher than that in GZO-4 grown under oxygen-rich conditions.

5.3 Conclusions

In conclusions, for heavily doped GZO with carrier concentrations above 10^{20} cm^{-3}, the temperature dependence of mobility measured in the range of 15-330K is well described by the Matthiessen's rule with mobility being limited by polar optical phonon (POP) scattering, and a temperature-independent mobility limited by ionized impurity scattering, compensation of Ga donors with acceptor defects, and electron scattering by low-angle grain boundaries limited by quantum-mechanical tunnelling. The data indicates that ionized impurity scattering is the dominant mechanism limiting the mobility in the range of 15-330 K for GZO layers with high structural quality grown under metal-rich conditions, which have porous features as well as low-angle grain boundaries parallel to the *c*-axis and relatively large average grain size of 20-25 nm, determined by XRD (30-50 nm by TEM). For these GZO layers grown under metal-rich conditions, POP scattering is the mechanism responsible for the temperature-dependence for T>150 K and thereby POP scattering cannot be neglected especially at RT. For the sample with $n=\sim 9\times 10^{20}$ cm^{-3} and LT mobility of ~51 $cm^2/V\cdot s$ at low temperatures, both grain boundary scattering and compensation if present are negligible due to their very minor effects. In contrast, for heavily doped GZO layers grown under oxygen-rich conditions, which have inclined grain boundaries and relatively small grain sizes of 10-20 nm determined by X-ray diffraction (10-30 nm by TEM), the compensation and grain boundary scattering became dominant. The high donor compensation in these layers is caused presumably by (Ga_{Zn}-V_{Zn}) complexes having the lowest formation energy in degenerate GZO grown under oxygen-rich conditions. The evolution of temperature dependences of mobility when the electron concentration reduces from 10^{20} cm^{-3} to 10^{18} cm^{-3} indicates that not only the contribution of grain-boundary scattering becomes stronger but also that the electron transport across boundaries changes from quantum-mechanical tunnelling to thermionic emission. In short, although the significance order of scattering mechanisms can differ for GZO layers with different growth conditions, metal-rich growth conditions, which can produce films with minimal deleterious effects by compensation and grain boundaries, are imperative for attaining high mobilities and high electron concentrations.

Chapter 6 Doped ZnO for p-Type Conductivity

This chapter discusses ZnO doped with a large-size-mismatched element of antimony (SZO) and ZnO codoped with nitrogen and tellurium (ZnO:[N+Te]).

6.1 ZnO doped with a large-size-mismatched element of antimony

Here the electrical properties of SZO layers with carrier concentrations varying from upper 10^{16} to upper 10^{19} cm^{-3} achieved under different growth conditions by plasma-enhanced molecular beam epitaxy (PE-MBE) on a-plane sapphire substrates were studied. The effects of Sb flux on the electrical properties and the structural properties of epitaxial SZO layers were described in details. The effects of substrate temperature T_{sub}, and oxygen pressure P_{O2} as well as the effects of post-growth heat treatments were also investigated to gain insight into the effects of other growth parameters and annealing on the electrical properties of epitaxial SZO layers.

All the SZO layers used in this study have a thickness of ~200 nm. To provide a better nucleation, a ~5-nm-thick low-temperature ZnO layer was inserted between a-plane sapphire substrate and the subsequent SZO film.

6.1.1 Antimony flux effects

To investigate the effect of Sb content on the electrical properties of SZO layers, a series of samples were grown with varying the Sb flux via changing the Sb cell temperature, T_{Sb}, in a wide range, from 370 ^{o}C to 570 ^{o}C. While Zn cell temperature and T_{sub} were kept at 350 ^{o}C and 400 ^{o}C, respectively. P_{O2} during growth was set at ~1×10^{-5} Torr which corresponds to near-stoichiometric growth conditions (reactive oxygen-to-metal flux ratio of ~1).

The Hall effect measurements at room temperature revealed *n*-type conductivity in all the SZO layers grown in a wide range Sb fluxes and thus in a wide range of Sb concentrations.

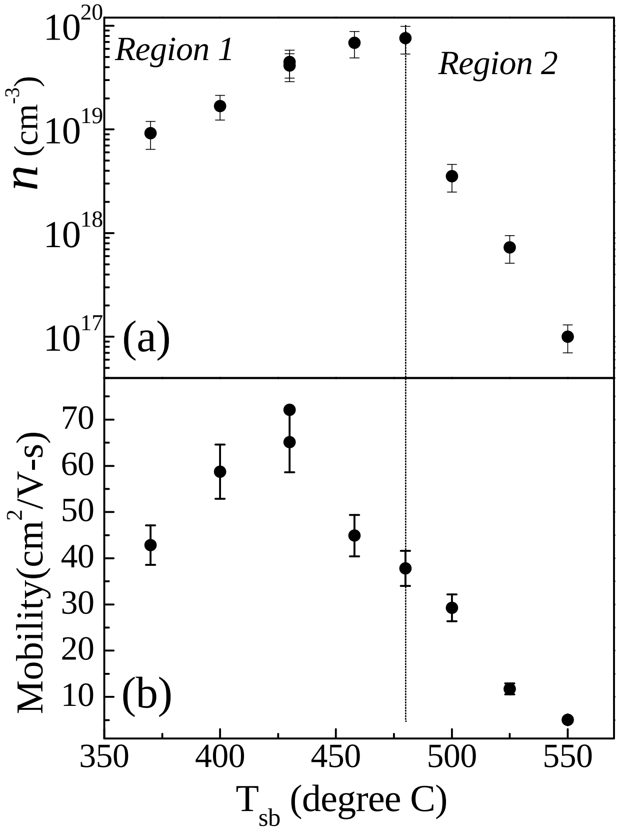

Figure 6.1 (a) Electron concentration and (b) mobility in SZO vs. Sb cell temperature, T_{Sb}.

Figure 6.1 (a) shows the dependence of the electron concentration in SZO on Sb cell temperature, T_{Sb}. As seen from the figure, the electron concentration first rises linearly with T_{Sb} , then tends to saturate at about 7.6×10^{19} cm^{-3} (region 1 in Figure 6.1), and finally drops down to 1×10^{17} cm^{-3} as T_{Sb} further increases from 480 to 550°C (region 2 in Figure 6.1). Further increase in T_{Sb} up to 570°C (not shown) produces insulating SZO films.

The increase in electron concentration in region 1 is obviously due to the increase in Sb flux and, therefore, the Sb concentration in SZO films. For two selected samples grown T_{Sb} = 430 °C (region 1) and T_{Sb} = 520 °C (region 2), the Sb content was estimated from electron dispersive spectroscopy (EDS) performed on cross-section samples in TEM. The Sb concentration was found to be below EDS detection limit (~0.1 at.%) for the first sample, and 0.9 at.% for the second sample. The initial increase in electron concentration indicates that Sb incorporates on Zn sites and act as a donor. The decrease in electron concentration with further increasing T_{Sb} in region 2 may be explained by formation of acceptor-type compensating defects (Sb on oxygen sites and/or point-defect complexes involving Sb) in the samples with high Sb content. Note that the O and Zn concentrations in the film with 0.9 at.% of Sb were found to be 53.52-56.26% and 45.58-42.76 at.%, indicating a near-stoichiometric growth condition but slightly oxygen rich.

Figure 6.1 (b) shows the Hall mobility as a function of T_{Sb}. In region 1, the Hall mobility first rises from 43 cm to ~70 $cm^2/V\cdot s$ as T_{Sb} increases from 370°C to 430°C (which corresponds to the exponential increase in carrier concentration in Figure 6.1 (a) and Arrhenius plot produced a thermal activation energy of ~0.9 eV), and then drops down to 5 $cm^2/V\cdot s$ with the further increase of T_{Sb}.

To explain the mobility behaviour, let us consider factors determining carrier mobility in heavily doped ZnO (carrier concentrations in the range of 10^{19} cm^{-3}). It is generally believed[11] that two major mechanisms limiting electron mobility are operative in this material: scattering on grain boundaries and scattering on ionized impurities.

Temperature-dependent Hall measurements were performed for selective layers to get insight into the origin of the mobility behaviour.

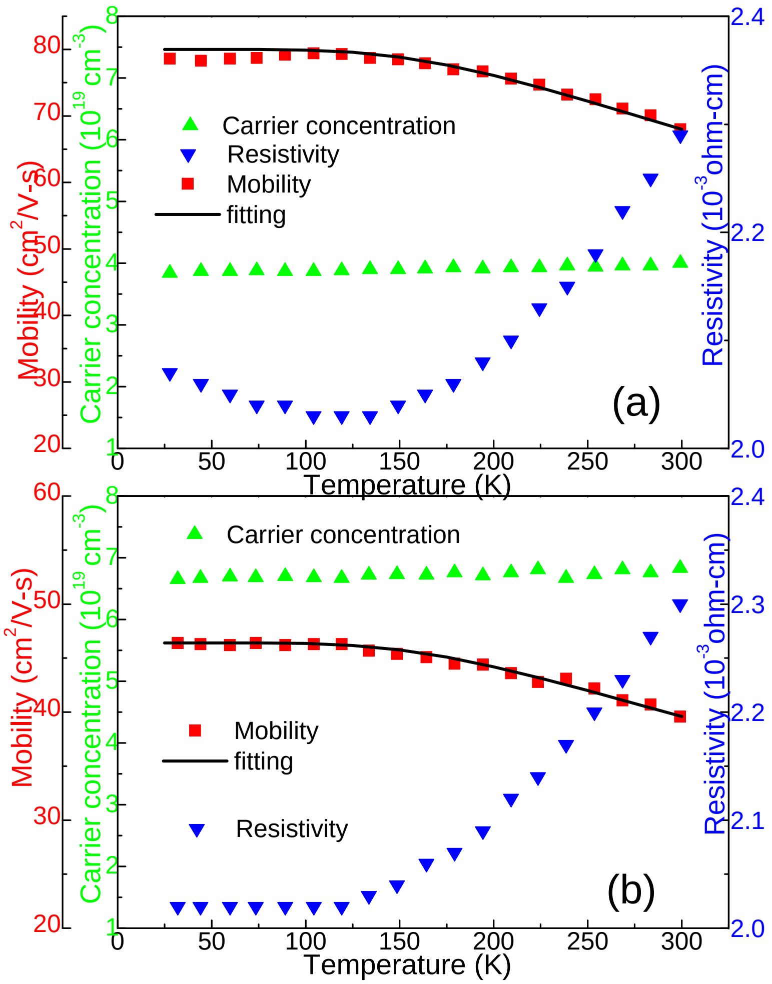

Figure 6.2 Temperature dependent Hall measurements for as-grown SZO layers grown at (a) T_{sb}=430 ^{o}C and (b) T_{sb}=460 ^{o}C.

Temperature dependences of the Hall mobility and electron concentration for the as-grown SZO samples grown at T_{Sb} = 430 ^{o}C (the sample showing the highest mobility) and T_{Sb} = 460 ^{o}C (the sample showing the second highest electron concentration) are shown in Figure 6.2 (a) and (b), respectively. While Figure 6.3 (a) and (b) illustrate the results of the same measurements for annealed SZO samples grown at T_{Sb} = 430 ^{o}C and T_{Sb} = 460 ^{o}C, respectively. As seen here, the carrier concentration in all the samples is temperature independent indicating the degenerate nature of the material. For all the samples, the temperature-dependent mobility curves were fitted

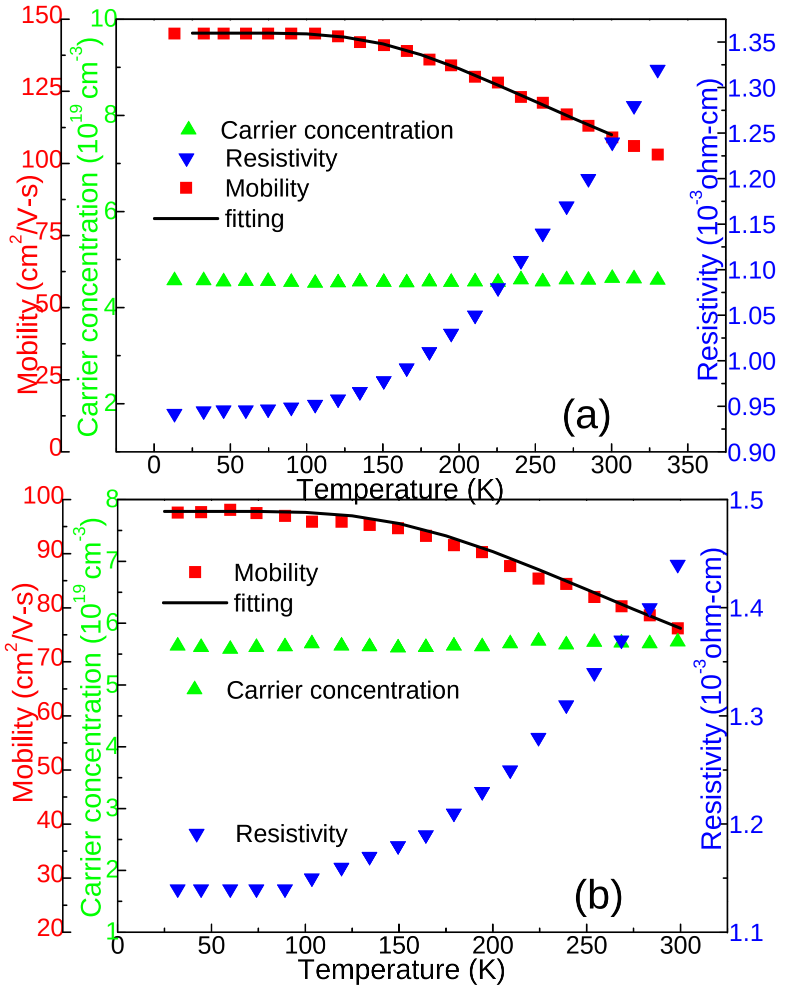

Figure 6.3 Temperature dependent Hall measurements for annealed SZO layers grown at (a) T_{sb}=430 ^{o}C and (b) T_{sb}=460 ^{o}C.

using the same method as used for heavily doped GZO (see Chapter 5). For all the samples, the mobility is independent of temperature in the temperature range below ~150 K. Fittings suggested that ionized impurity scattering with compensation is the dominant mechanism limiting the low-temperature mobility. The reduction in mobility at temperatures above ~150 K is attributable to polar-phonon scattering. Thus, the initial increase in mobility (corresponding to the increase in carrier concentration) may be explained by screening of ionized impurities by free electrons. Note that the increase in mobility with the increase in Sb content could also exclude that neutral impurity scattering is important in those films. The decrease in mobility with further increase in Sb content may be attributed to the formation of more compensating defects in the layers grown at $T_{Sb} > 430^oC$ (the range where electron concentration tends to saturate and then drops as T_{Sb} further rises in Figure 6.1 (a)) as well as to degradation of structural quality of SZO with increasing Sb content, as evident from RHEED, XRD and TEM data discussed below. Note that, upon annealing for sample grown at $T_{Sb} = 430^oC$, electron concentration even increases slightly and the electron mobility is significantly improved (Figure 6.3 (a)): the annealed sample shows respectful room-temperature value of 110 cm^2/V-s and low temperature value as high as 145 cm^2/V-s which is close to the maximum mobility value (~155 cm^2/V-s) calculated based on the degenerate form of Brooks-Herring formula for ionized impurity scattering. For the other annealed sample (Figure 6.3 (b)), the electron mobility is also significantly improved but the electron concentration slightly decreased. This could be because of either the non-uniformity of electron distribution or over-annealing since the optimum annealing temperature slightly varies from sample to sample.

The RHEED characterization indicated that the growth mode changed from weekly 3-dimentional (3D) growth mode to 3D growth mode when T_{Sb} increased from 370 to 480^oC. The RHEED patterns became blurry when T_{Sb} further increased to 550 ^oC [see Figure 6.4].

Figure 6.5 illustrates the XRD 2θ-ω scans for SZO grown at $T_{Sb}=430^oC$ (solid line) and 550^oC (dash line), respectively. As seen, the (0002) peak of ZnO for the SZO with a blurry RHEED pattern shifted to a much lower angle when T_{Sb} was increased from 430^oC to 550^oC, indicating a much larger out-of-plane *c* lattice constant. The *c* lattice constants for all the samples in Figure 6.1 were calculated based on the XRD measurements.

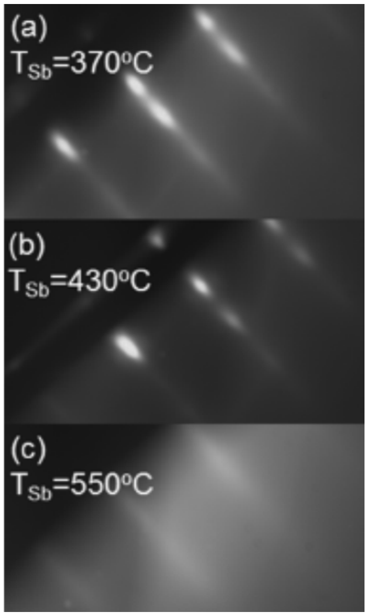

Figure 6.4 RHEED pattern recorded along [1-100] azimuth for SZO grown at (a) T_{Sb}=370°C, (b) T_{Sb}=430°C, and (c) T_{Sb}=550°C

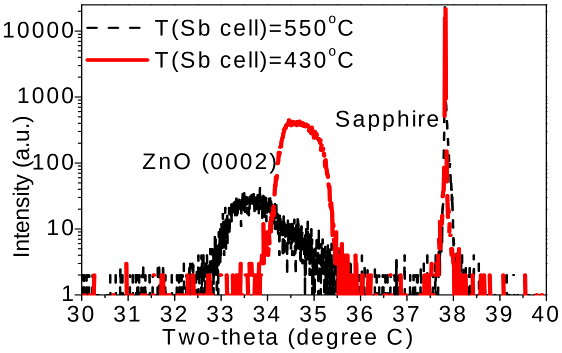

Figure 6.5 XRD 2θ-ω scan of SZO grown at T_{Sb}=430°C (solid line) and 550°C (dash line), respectively.

Figure 6.6 shows the out-of-plane *c* lattice parameter derived from 2θ-ω HRXRD scans as a function of T_{Sb}. At T_{Sb} up to 500°C (the whole region 1 and a portion of region 2 in the carrier concentration vs. T_{Sb} plot in Figure 6.1 (a)) the *c* parameter of SZO layers remains virtually unchanged, close of bulk ZnO value of 5.206 Å, and then abruptly increases to ~5.296 Å for the layer grown at T_{Sb} = 520°C. When T_{Sb} increases from 520°C to 550°C, the *c* lattice parameter further rises. The observed behavior of the *c* lattice parameter can be explained as follows. If we assume that in the SZO layers with lower Sb concentration Sb occupies predominately Zn lattice sites, the *c* lattice will not change too much since the ionic radius of Sb^{3+} (0.78 Å) is close to that of Zn^{2+} (0.74 Å) and therefore Sb incorporation has no profound effect on the ZnO lattice parameter. Moreover, Sb ions on the Zn positions act as donors, which is consistent with the observed increase in electron concentration with increasing T_{Sb} (Figure 6.1 (a), region1). While in the layers with higher Sb content more Sb could be forced to substitute oxygen which could considerably increase the lattice distortion although the amount of Sb in oxygen position could be still very small compared with the total Sb concentration. Note that the ionic radius of Sb^{3-} (2.44 Å) far exceeds that of O^{2-} (1.38 Å), therefore even a small amount of incorporation of Sb on the O sites should lead to an increase in the *c* lattice parameter of SZO as well as to compensation of the Sb_{Zn} donors. It must be pointed out that the other complex-like acceptor defects are not excluded, which could somehow affect both the lattice parameter and the electron concentration.

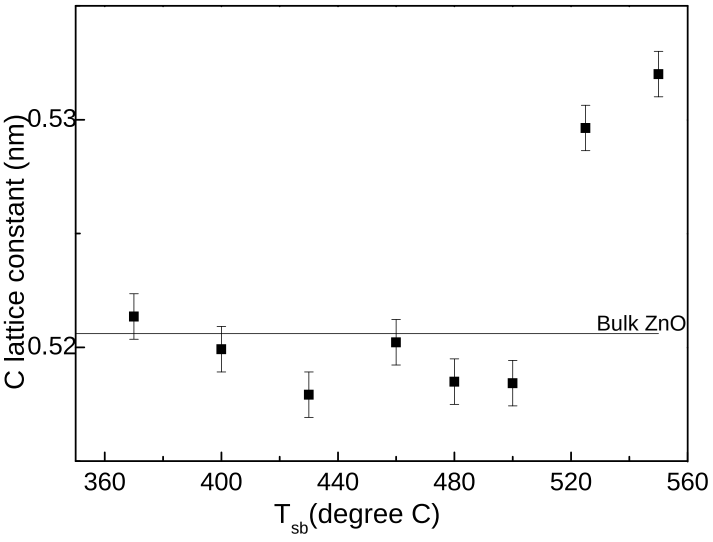

Figure 6.6 out-of-plane *c* lattice parameter derived from 2θ-ω HRXRD scans as a function of T_{Sb}.

Actually, the same phenomenon of the increase in *c* lattice constant with the increase in Sb content was also reported by several groups recently. Yang et al.[84] claimed that not all the Sb took the Zn positions. Instead, some of them formed Sb-O clusters which can significantly increase the *c* lattice constant. However, this kind of clusters was not observed for our samples from TEM measurements, which data will be shown later. Zhu et al.[136] and Samanta. et al.[80] just simply attributed that to the substitution of Zn with Sb since the radius of Sb^{3+} is slightly larger than that of Zn^{2+} (0.92 Å vs. 0.74 Å in reference 136 and 0.78 Å vs. 0.74 Å in reference 80). If this explanation is correct, the reduction in both electron concentration and mobility for samples in region 2 caused by compensation has to be explained due to mainly the Sb_{Zn}-$2V_{Zn}$ complexes since no Sb substitutes O. However, this explanation of the increase in *c* lattice constant due to the substitution of Zn with Sb cannot exclude the possibility of more Sb starting to substitute O for SZO films with high Sb content, although the number of Sb_O is much less than that of $Sb_{Zn.}$ At this stage, it is difficult to determine whether Sb will substitute O. But remember that Wahl et al.[76] concluded that Sb can substitute O, with the possible fraction on O sites being at maximum 5%-6%. So maybe both the Sb_O acceptors and the Sb_{Zn}-$2V_{Zn}$ complex-like acceptors exist, which really need further studies.

Figure 6.7 shows the FWHM of (0002) SZO XRD ω-rocking curves as a function of T_{Sb}. As seen from the figure, the FWHM values remain virtually unchanged (FWHM ~0.53^o) for the antimony-cell temperatures corresponding to region 1 in Figure 6.1 (a) and rapidly increase with T_{Sb} at $T_{Sb} \geq 480^oC$ (region 2). The broad XRD ω-rocking curves point to inferior crystal perfection of ZnO with high Sb concentration.

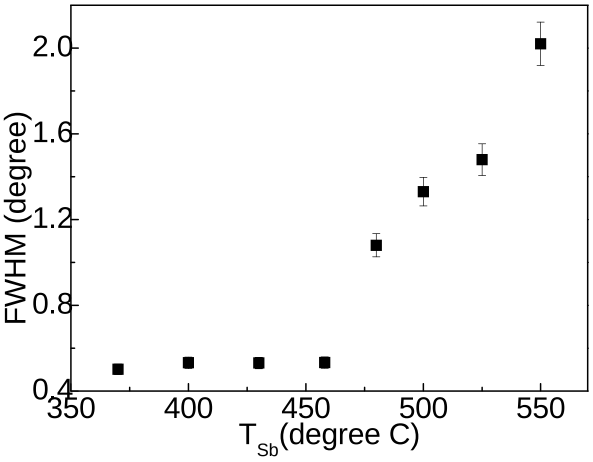

Figure 6.7 FWHM of (002) SZO XRD ω-rocking curves as a function of Sb sell temperature, T_{Sb}

STEM measurements were performed for two selective SZO samples with ~0.1 at.% and ~0.9 at.% Sb contents, corresponding to T_{Sb} =430°C and 520°C, respectively. Pores and dislocations are clearly seen in both samples. The formation of pores is not preparation artifact and has been observed also in GZO as discussed earlier. According to STEM data, the densities of dislocations in both samples are comparable, which are ~$4\pm1\times10^{10}$ dislocations/cm^2. Although the comparable dislocation densities in samples with different Sb concentration are unexpected, the XRD data showing much broader rocking curve for the former sample could still indicate the former sample has more dislocations. Figure 6.8 shows the cross-sectional STEM image of the SZO sample with 0.9 at.% Sb content (T_{Sb} = 520 °C) from which grain boundaries are hardly seen and consequently grain boundary scattering should be not important. Based on Equation 3 for dislocation scattering the mobility limited by dislocating scattering is at least one order of magnitude higher than the measured Hall mobility (~10 cm^2/V-s) for the sample with 0.9 at.% Sb content (T_{Sb} = 520 °C). Therefore, compensation caused by the extra of Sb in the film should be responsible for the low mobility of ~10 cm^2/V-s, which is also consistent with the reduced electron concentration of ~7×10^{17} cm^{-3} at higher Sb content since compensation not only reduce the mobility but also reduce the electron concentration.

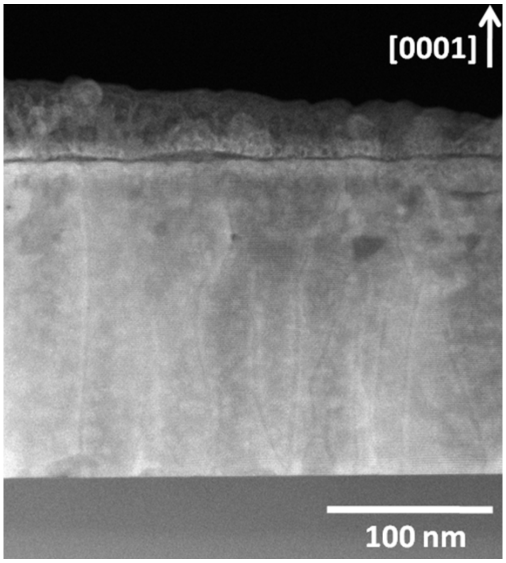

Figure 6.8 Cross-sectional TEM image of the SZO sample with 0.9 at.% Sb content (T_{Sb} = 520 °C).

The increase in dislocation density along with the decrease in electron concentration with increasing Sb content in SZO has also been reported by Guo *et al.*[66] who reported p-type SZO with 1 at.% Sb content. However, the Sb_{Zn}-$2V_{Zn}$ complexes were proposed to be responsible for both the deterioration in crystal quality and the reduction in electron concentration. At this stage, it is still challengeable to use TEM/STEM to determine whether Sb substitutes O or substitutes Zn for our samples and further studies could be needed. In short, the deterioration in crystal quality at higher Sb content, no matter how this happened, could indicate that the large-size-mismatched element of Sb could not be a good candidate to achieve promising p-type conductivity.

6.1.2 Substrate temperature effects

Effect of substrate temperature on electrical characteristics of SZO layers were studied for two selected Sb fluxes, namely T_{Sb}= 400 ^{o}C (region 1) and 550 ^{o}C (region 2). Note that oxygen pressure during growth is still ~1×10^{-5} Torr and film thickness was controlled to be ~200 nm.

Table 6.1 compares the electrical properties of the SZO layers grown at substrate temperatures of 400 and 600 ^{o}C. As seen from the table, the increase in substrate temperature results in the less conductive SZO films for the both T_{Sb} regions. As seen from the table, the higher resistivity of the films grown at 600 ^{o}C is due to the reduction in both electron concentration and mobility. The detail study of the genesis of the observed effects is underway. Generally speaking, the reduced electron concentration and mobility observed at higher substrate temperatures could be caused by the lower incorporation efficiency of Sb on the Zn sites and the formation of acceptor-type defects compensating donors as well as the reduction in native donor defects. Comparison between the undoped ZnO grown at substrate temperatures of 400 and 600 ^{o}C, respectively, confirmed that the electron concentration originated from the native defects was slightly reduced by ~5×10^{16} cm^{-3}, indicating that higher substrate temperature could be better to achieve p-type conductivity if which can be implemented since compensation will be reduced.

Table 6.1 Comparisons of substrate temperature effects on electrical properties of SZO.

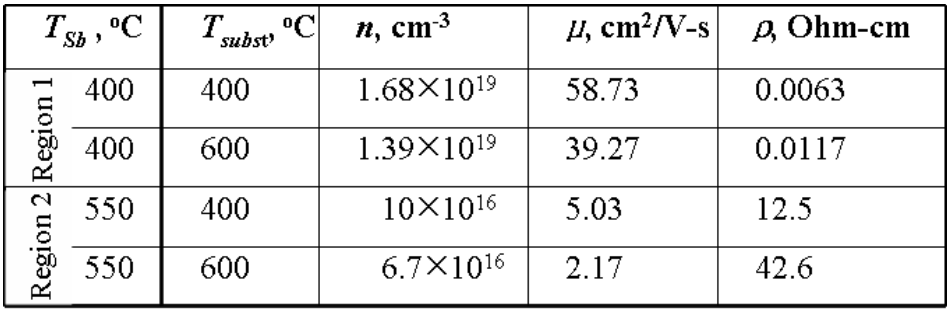

	T_{Sb} , ^{o}C	T_{subst}, ^{o}C	n, cm^{-3}	μ, cm^{2}/V-s	ρ, Ohm-cm
Region 1	400	400	1.68×10^{19}	58.73	0.0063
	400	600	1.39×10^{19}	39.27	0.0117
Region 2	550	400	10×10^{16}	5.03	12.5
	550	600	6.7×10^{16}	2.17	42.6

6.1.3 Oxygen effects

Figure 6.9 shows the effect of oxygen pressure during MBE growth, P_{O2}, on electron mobility and electron concentration in the SZO layers with low Sb concentrations (region 1 in Figure 6.1). One can see that for the layers grown under metal-rich conditions ($P_{O2} = 0.45\times10^{-5}$ Torr) both parameters are considerably lower than those for the samples grown at higher oxygen pressures. We may assume that the oxygen-rich (and, consequently, Zn-deficient) conditions favor the incorporation of Sb on the Zn sites and formation of Sb_{Zn} donors. One the other hand, the formation of Sb_O acceptors compensating Sb_{Zn} donors is suppressed under high oxygen pressure. Both factors results in higher electron concentration and mobility.

Note that the Sb_{Zn}-$2V_{Zn}$ complexes were typically thought to be responsible for the compensation in SZO films. However, this type of acceptors should not exist in the SZO films with low Sb content grown under either metal-rich or oxygen-rich conditions as shown in Figure 6.9. This is because of the followings. The concentration of Sb_{Zn}-$2V_{Zn}$ complexes should increase with the oxygen pressure, since the probability of Zn vacancy formation is higher at high oxygen pressure. And then the measured electron concentration should be reduced for a given Sb cell temperature due to compensation. In contrast, the reduced electron concentration with the increase in oxygen pressure is not observed. So the only possible reason is that for SZO films with low Sb content, no Sb_{Zn}-$2V_{Zn}$ complexes are available due to the low Sb content (<0.1 at.%). While for SZO films grown under metal-rich conditions, a small amount of Sb_O acceptors exist but it is less than that of Sb_{Zn} donors, which makes the films still weak n-type. When oxygen pressure during growth was increased, the formation of Sb_O acceptors was suppressed. Instead, more Sb substituted Zn, resulting in both higher electron concentration and mobility. Note that this hypothesis only applies to SZO with low Sb content. Note that both theoretical and experimental results suggested that oxygen-rich conditions be used to achieve p-type doping for

ZnO doped with a large-size-mismatch element of As or Sb since it will severely suppress the formations of As_O and Sb_O but favor the formations of Sb_{Zn}-$2V_{Zn}$ complexes.[77] The conclusion given here supports the analysis of the data in Figure 6.9.

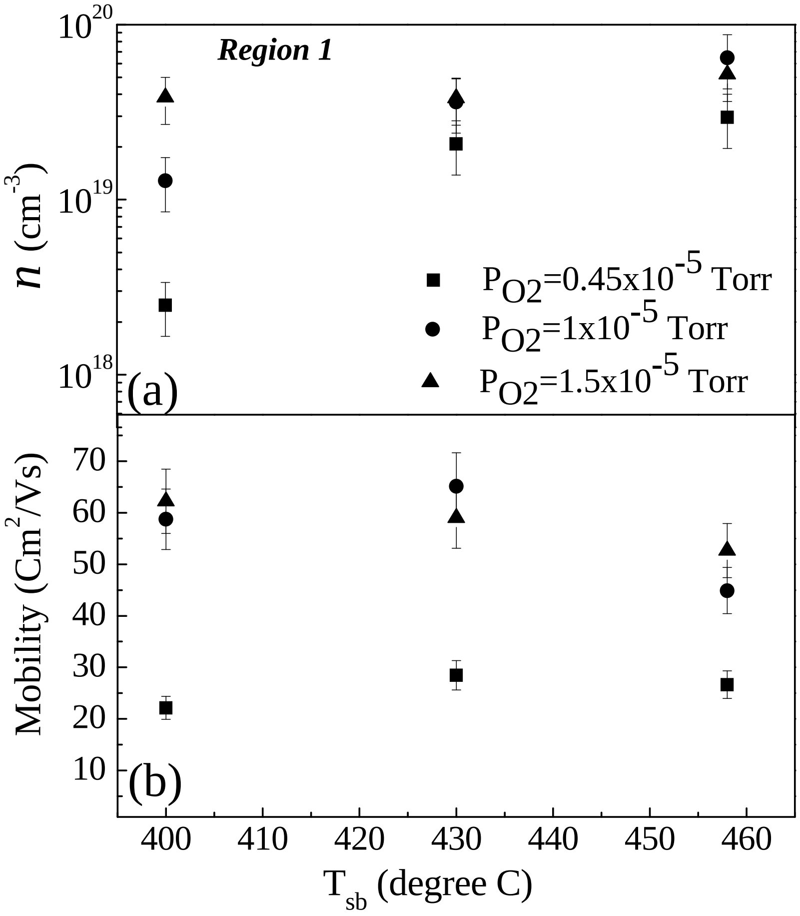

Figure 6.9 Effect of oxygen pressure during growth, P_{O2}, on electron concentration (a) and mobility (b) for the SZO layers grown with low Sb flux (region 1). P_{O2}=0.45×10^{-5} Torr (square,) P_{O2}=1×10^{-5} Torr (circle), and P_{O2}=1.5×10^{-5} Torr (triangle).

As can be seen from Figure 6.9 (a), the electron concentration tends to saturate when T_{Sb} increases for all the oxygen pressures used. This behavior suggests that the incorporation of Sb ions on the Zn sites approaches the effective solubility limit as T_{Sb} approaches 480 °C, *i.e.*, the boundary between region 1 where electron concentration increases with increasing Sb flux and region 2 in which the electron concentration drops with further increasing T_{Sb}. Further increase in Sb flux leads to the incorporation of Sb on the oxygen sites, formation of dislocations and probably point-defect complexes involving Sb (Sb_{Zn}-$2V_{Zn}$ complexes) also acting as acceptors compensating Sb_{Zn} donors. This picture is consistent with the data of structural analysis showing a rapid degradation of SZO crystallinity with increasing T_{Sb} in region 2 as illustrated by Figure 6.4 to Figure 6.7. The Sb solubility in ZnO based on the results here should be lower than 1 at.% since EDS revealed the Sb content in the SZO layer grown at T_{Sb}=520 ^oC is ~0.9 at.%, which is much lower than the reported result of 3 at.%[86], which need further studies.

The results obtained above show that high Sb content and high substrate temperature during growth are the factors decreasing electron concentration in Sb-doped ZnO. Therefore, in attempt to achieve *p*-type ZnO, we grew SZO layers at a higher substrate temperature (600 ^oC) and high Sb flux (T_{Sb}=550 ^oC, corresponding to region 2) at different oxygen pressures, $P_{O2}=0.45\times10^{-5}$, 1×10^{-5}, and 1.5×10^{-5} Torr. In all cases, the SZO were found to be of *n*-type. In the first and second cases, the electron concentrations are in the mid-10^{16} cm^{-3} range, while electron mobilities are ~2-3.7 $cm^2/V\cdot s$, resulting in a resistivity around 27-42 Ohm-cm. For the sample grown at $P_{O2}=1.5\times10^{-5}$ Torr, the resistivity varied around 400 Ohm-cm but the measured carrier concentration and mobility depend on the measurement conditions (applied magnetic field=5-7KG and current=5-20nA) and consequently are not reliable. The unreliability could be caused by strong localization of free carriers caused by high defect concentration in the sample. Note that for $P_{O2}=1.0\times10^{-5}$ Torr, the O and Zn concentrations in the film with 0.9 at.% of Sb were found to be 53.52-56.26% and 45.58-42.76 at.%, indicating a near-stoichiometric growth condition but slightly oxygen rich. Consequently, $P_{O2}=1.5\times10^{-5}$ Torr corresponds to a strong oxygen-rich condition. However, no reliable p-type ZnO was achieved under oxygen-rich condition along with a higher Sb fux and a higher substrate temperature.

6.1.4 Summary for Sb-doped ZnO

To confirm that the high n-type conductivity in SZO grown on a-sapphire substrates is not due to the Al out-diffusion from the substrates, undoped ZnO and Sb-doped ZnO were grown on 330 μm thick bulk ZnO substrates (CrysTec GmbH) for comparisons. Comparisons indicated that the high n-type conductivity is due to the Sb doping effect while not due to the Al out-diffusion from the sapphire substrate. Meanwhile, comparisons between Sb-doped and undoped ZnO on glass substrates grown under either vacuum or oxygen environment by pulsed laser deposition[136] also support the above conclusion, where the increase in electron concentration of ZnO once doped with Sb is in the range of $1.6\text{-}5.78\times10^{19}$ cm^{-3}.

In summary, the investigation of Sb flux effect (T_{Sb}) indicated that Sb acts as a donor in a wide electron concentration range (upper 10^{16} to upper 10^{19} cm^{-3}) and optimum growth condition along with post-growth annealing in nitrogen environment even produced high mobility of 145.2 $cm^2/V\cdot s$ at 15K or 110 $cm^2/V\cdot s$ at 300K along with the electron concentration of 4.53×10^{19} cm^{-3}. The donor behavior of Sb indicated that the majority Sb ions reside on Zn sites instead of O sites and the thermal activation energy of the donor determined by the Arrhenius plot is ~0.9 eV. While the reduction in both electron concentration and mobility with increasing Sb flux is caused by the deterioration of crystal quality and the lattice distortion revealed by increased *c* lattice constant and FWHM, which are indicative of the formations of extended defects such as dislocation, various grain and domain boundaries, point defects, and point-defect complexes related to the extra Sb. The deterioration in crystal quality at higher Sb content, no matter how this happened, could indicate that the large-size-mismatched element of Sb could not be a good candidate to achieve promising p-type conductivity. Substrate temperature effects showed higher substrate temperature can produce SZO with lower electron concentration and lower mobility probably due to the lower incorporation efficiency of Sb, the reduction in native defects in ZnO, and the possible formation of some type of acceptors with Sb involved at higher substrate temperature. Oxygen effects indicate that the probability of the substitution of O with Sb (Sb_O) being an acceptor exists especially in SZO layers grown under lower oxygen pressures but the overwhelming electrons provided by the donors of Sb in Zn sites always make the SZO layers n-type. The electron concentration tends to saturate when T_{Sb} increases up to 480 ^oC for all the oxygen pressures used, which indicates the incorporation of Sb ions on the Zn sites approaches the effective solubility limit.

6.2 ZnO co-doped with nitrogen and tellurium

6.2.1 Experiments

The same plasma power supply as used before for GZO or SZO growth was used to ignite both the oxygen and nitrogen simultaneously in order to supply the reactive oxygen and nitrogen. The flux of oxygen and that of nitrogen into the plasma power supply were controlled by two MFCs and the total pressure in the growth chamber was controlled by a pressure gauge installed in the main chamber.

Figure 6.10 shows an example of optical spectra obtained for the plasma power supply when only oxygen was supplied (dots). The main oxygen emission peak is located at ~778 nm. When both oxygen and nitrogen were supplied, the optical spectra (line) show considerable changes in some wavelength ranges, indicating one plasma power supply could be successfully used to ignite both oxygen and nitrogen. The detailed explanation of nitrogen-related emission peaks can be found elsewhere[137], where the optical spectra were obtained from the same plasma power supply as used here. In general, the changes in the wavelength range of 280-400 nm (second positive molecular series) and in the wavelength range of 550-650 nm (first positive molecular series) are caused by molecular N_2. The main atomic nitrogen related emission peak is located at ~750 nm as seen in Figure 6.10. Note that the spectra here were collected by an optical fiber and therefore the resolution is relatively low.

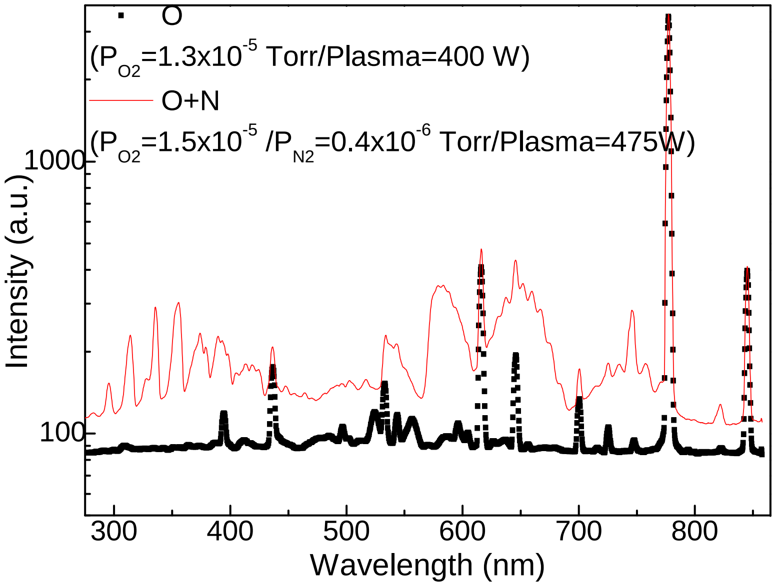

Figure 6.10 Optical spectra from the plasma power supply with only oxygen (dots) and with both oxygen and nitrogen (line). Note that the main peaks for oxygen emission (~778 nm) for the two cases have a comparable intensity

The doping level of N in the ZnO films was expected to be controlled by changing the ratio of N to O. One effusion cell with 5N Te was used as the doping source of Te. First, the effects of substrate temperatures on the electrical and structural properties of N-doped and N and Te co-doped ZnO were investigated for a selective Te flux and a fixed ratio of N to O. Next, Te flux effect and the effect of N-to-O ratio were investigated. RTA annealing was employed for selective layers to study the annealing effects on films. For all films, a ~10 nm LT ZnO buffer layer was employed to provide better nucleation.

6.2.2 Substrate temperature effects

Te cell temperature (T_{Te}) of 375 °C and N-to-O ratio of 0.3 (3×10^{-6} Torr vs. 10×10^{-6} Torr) were chosen to study the substrate temperature effects on the properties of ZnO:N or ZnO:[N+Te], which are 400, 500, and 600 °C, respectively. Meanwhile, Te doping effects can also be studied once Te dopants were introduced into the films.

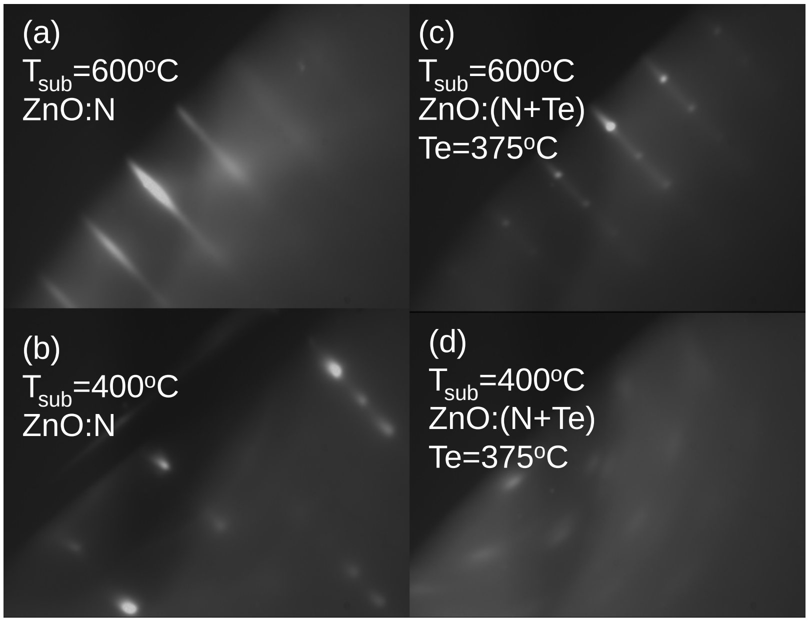

Figure 6.11 RHEED images of (a) ZnO:N grown at T_{sub}=500 °C, (b) ZnO:N grown at T_{sub}=300 °C, (c) ZnO:[N+Te] grown at T_{sub}=500 °C, and (d) ZnO:[N+Te] grown at T_{sub}=300 °C. Note: T_{Te} = 375 °C and N-to-O ratio = 0.3 (3×10^{-6} Torr vs. 10×10^{-6} Torr).

Figure 6.11 shows the RHEED patterns recorded for ZnO:N and ZnO:[N+Te] grown at different substrate temperatures. From Figure 6.11 (a) and (b), we can see that the growth mode for ZnO:N films changed from 2D to 3D when substrate temperature was reduced from 600 °C to 400 °C. Note that the growth mode for the ZnO:N grown at substrate temperature of 500 °C is also 2D. This could be because of that higher growth temperature is favorable to obtain a smooth surface due to the longer migration length of adatoms.[138] However, once Te was introduced into the ZnO:N films grown at the same conditions as those in Figure 6.11 (a) and (b), the RHEED pattern indicated much worse surfaces of those ZnO:[N+Te] films [see Figure 6.11 (c) and (d)]. The ZnO: [N+Te] films with a RHEED pattern as shown in Figure 6.11 (d) are not acceptable in terms of the crystal quality.

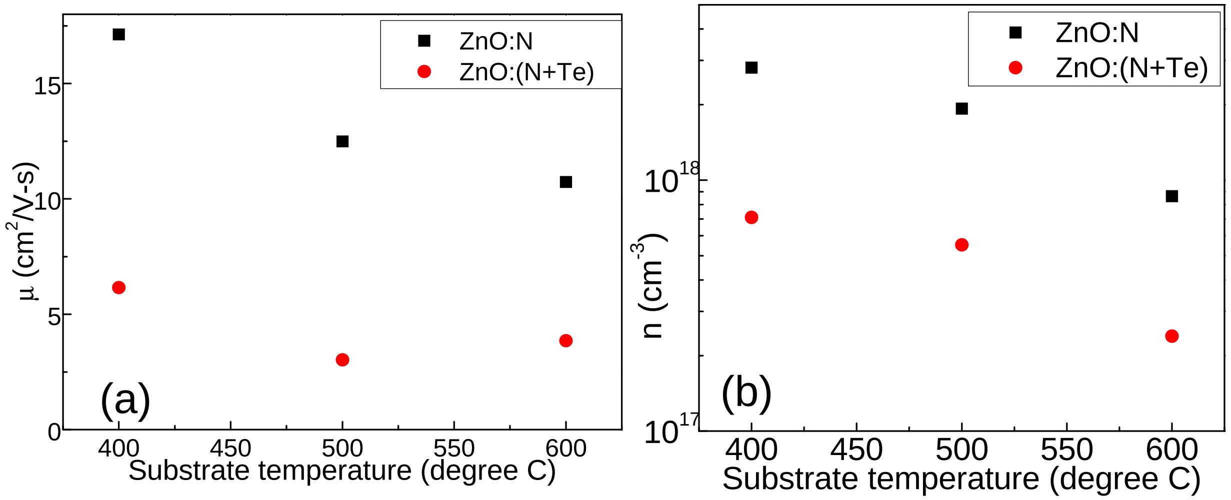

Figure 6.12 (a) mobilities and (b) electron concentrations of ZnO:N and ZnO:[N+Te] grown at different substrate temperatures. Note: N/O ratio=0.3, P_{O2}=10^{-5} Torr, and T_{Te}=375°C.

Figure 6.12 (a) and (b) show the mobilities and electron concentrations of above-mentioned ZnO:N and ZnO:[N+Te] layers grown under different substrate temperatures, respectively. As seen, higher substrate temperature produced lower electron concentration and lower mobility for both ZnO:N and ZnO:[N+Te] layers. For ZnO:N samples, even grown at higher substrate temperature of 600 °C, no signs of N being a p-dopant can be seen from the electrical measurements. In general, the electron concentration of N-doped ZnO layers is slightly higher than that for undoped ZnO grown at the same substrate temperature, while the corresponding mobility is lower. Park et al.[95] also observed the n type conductivity of N-doped ZnO with an electron concentration of 2.5×10^{17} cm^{-3} but once Te was also introduced into the ZnO film p-type ZnO was achieved. It is noteworthy that bulk ZnO substrate instead of sapphire substrate was used in the work just mentioned, which could be the reason why p-type ZnO was achieved by co-doping technique once Te was also introduced. Recently, theoretical results from Lyons et al.[139] and experimental results from Tarun et al.[140] produced a conclusion that nitrogen is a deep acceptor in ZnO and consequently it cannot produce p-type ZnO. More studies are needed since the above-mentioned results are not consistent with the predication of N being O position as a shallow acceptor as well as the reported results of p-type ZnO doped with N. Anyway, both the electron concentration and mobility were considerably reduced once Te was introduced as seen in Figure 6.12, indicating Te can suppress the formation of donors, which was explained as Te can help increase the incorporation of N[97].

6.2.3 RTA annealing effects and Te effects

For reported p-type ZnO, they are more often achieved by means of post-annealing in oxygen environment. Therefore, annealing in oxygen environment was carried out to investigate whether p-ZnO can be achieved through the co-doping of N and Te technique. It is obvious that the ZnO:[N+Te] grown at substrate temperature of 600 ^{o}C is the best sample to be used for annealing since its mobility and electron concentration are the lowest (~3.8 cm^2/V-s and ~ 2.4 $\times10^{17}$ cm^{-3}).

Figure 6.13 shows the RTA annealing temperature effects. After annealing, the ZnO:[N+Te] samples grown at the substrate temperature of 600 ^{o}C are still n type. For the sample annealed at temperature of 800 ^{o}C, the resistivity is considerably increased (~40 ohm-cm) compared with the as-grown sample (~6.8 ohm-cm). For the sample annealed at temperature of 800 ^{o}C, the measured mobility and carrier concentration scattered based on the applied current and magnetic field, which sometimes exhibited a p-type but it is not reliable. However, the considerable increase in resistivity is consistent with what Porter et al.[93] observed, indicating Te could reduce the Madelung energy as propsed[91].

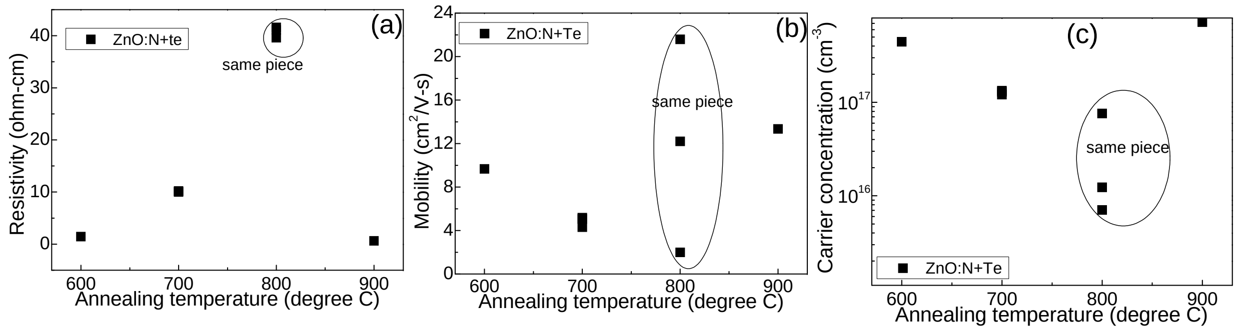

Figure 6.13 RTA annealing temperature effects on (a) resistivity, (b) mobility, and (c) carrier concentration of ZnO:[N+Te].

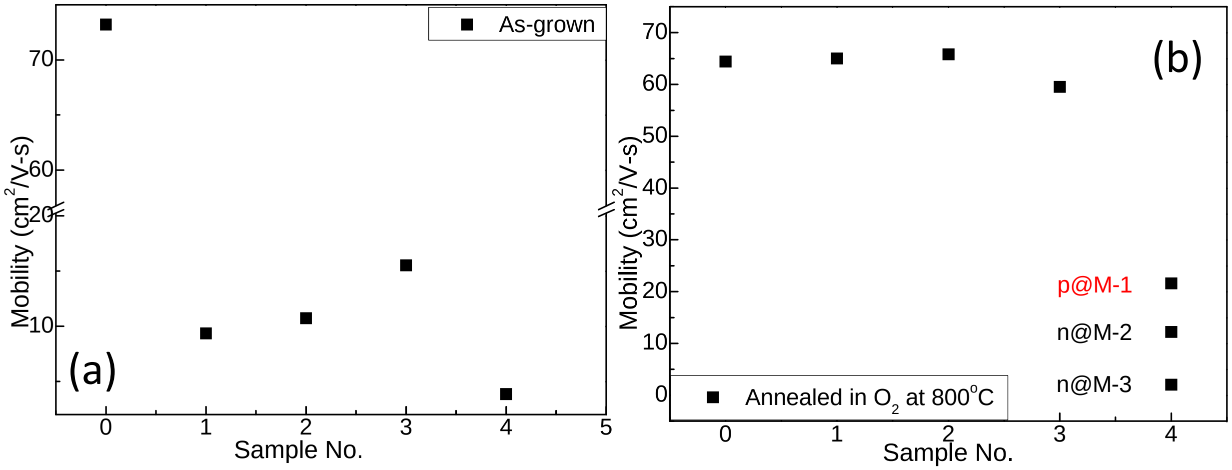

Figure 6.14 Comparisons of mobilities before and after RTA annealing at the same temperature of 800 ^{o}C in oxygen environment for reference samples of ZnO, ZnO:N, ZnO:Te, and ZnO:[N+Te]. Note that the numbers of 0, 1, 2, 3, and 4 are assigned for the best ZnO achieved, ZnO possibly affected by Te from the sample holder, n-doped ZnO, Te-doped ZnO, and co-doped ZnO respectively.

To confirm the effect of Te helping increase the resistivity of ZnO:[N+Te], 4 reference samples of ZnO, ZnO:N, ZnO:Te are annealed at the temperature of 800 ^{o}C in oxygen environment. Note that the T_{Te}=375 ^{o}C for the growth of Te-doped ZnO sample. The numbers of

0, 1, 2, 3, and 4 are assigned for the best ZnO achieved, ZnO possibly affected by Te from the sample holder, n-doped ZnO, Te-doped ZnO, and co-doped ZnO respectively. It is obvious to see from Figure 6.14 that all reference sample showed a very high mobility above 60 cm^2/V-s and only the ZnO:[N+Te] exhibited a mobility much lower than 30 cm^2/V-s after they were annealed at the temperature of 800 ^{o}C in oxygen environment. Also, it is obvious to see from Figure 6.15 that after annealing all the reference samples including the undoped ZnO, N-doped ZnO, and Te-doped ZnO, their electron concentrations are ~ 10^{18} cm^{-3}. In contrast, the electron concentration of the ZnO:[N+Te] annealed at the temperature of 800 ^{o}C in oxygen environment is lower than 10^{17} cm^{-3}, which is one order of magnitude lower and sometimes exhibit p-type results from Hall measurement although it is not reliable at all. In general, the reference samples become more conductive and their resistivities are about 0.1 ohm-cm while that of the ZnO:[N+Te] after annealing is about 40 ohm-cm. The comparisons as mentioned above support that Te really helps increasing the resistivity of ZnO:[N+Te], which shows the potential to help achieve the p-type ZnO doped with N if N is really a shallow acceptor.

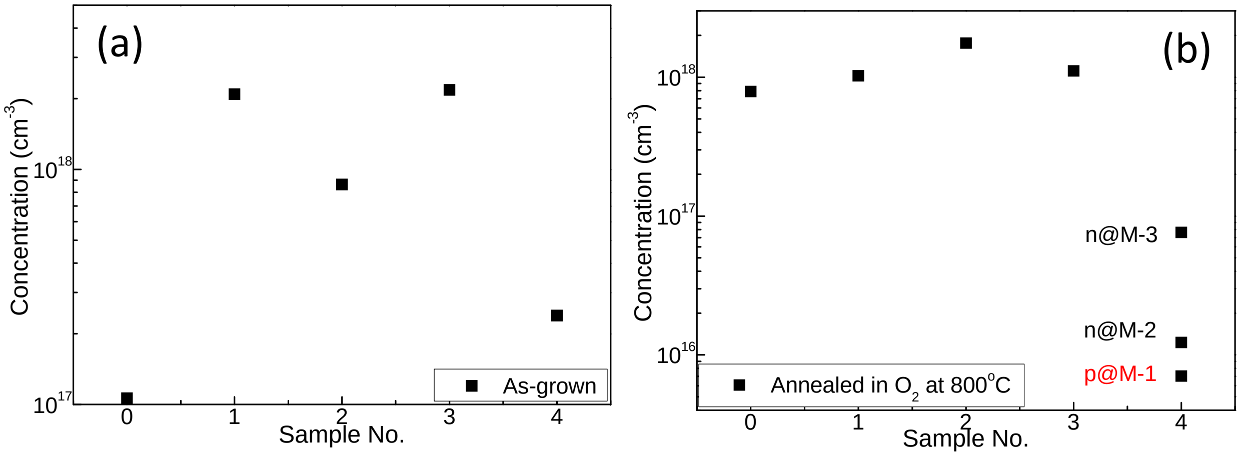

Figure 6.15 Comparisons of carrier concentrations before and after RTA annealing at the same temperature of 800 ^{o}C in oxygen environment for reference samples of ZnO, ZnO:N, ZnO:Te, and ZnO:[N+Te]. Note that the numbers of 0, 1, 2, 3, and 4 are assigned for the best ZnO achieved, ZnO possibly affected by Te from the sample holder, n-doped ZnO, Te-doped ZnO, and co-doped ZnO respectively.

Annealing in oxygen environment could be a necessary technique to achieve p-type ZnO because it can significantly improve the crystal quality and consequently possibly increase the incorporation of N. The annealing process could also help get rid of the excess Te from the ZnO film since the red color from Te disappeared after annealing. The XRD 2θ-ω scan and XRD ω scan as shown in Figure 6.16 proved that the annealing process considerably improved the crystalline quality of the ZnO:[N+Te]. The FWHM of the annealed ZnO:[N+Te] is about 0.33° which is comparable to the best un-doped ZnO as discussed earlier in sections for GZO. AFM (5μm by 5μm scan) revealed that the RMS surface roughness for the annealed sample is about 2.6 nm. However, no reliable p-type ZnO has been achieved even if annealing was used. To achieve p-type ZnO, more optimized condition could be needed.

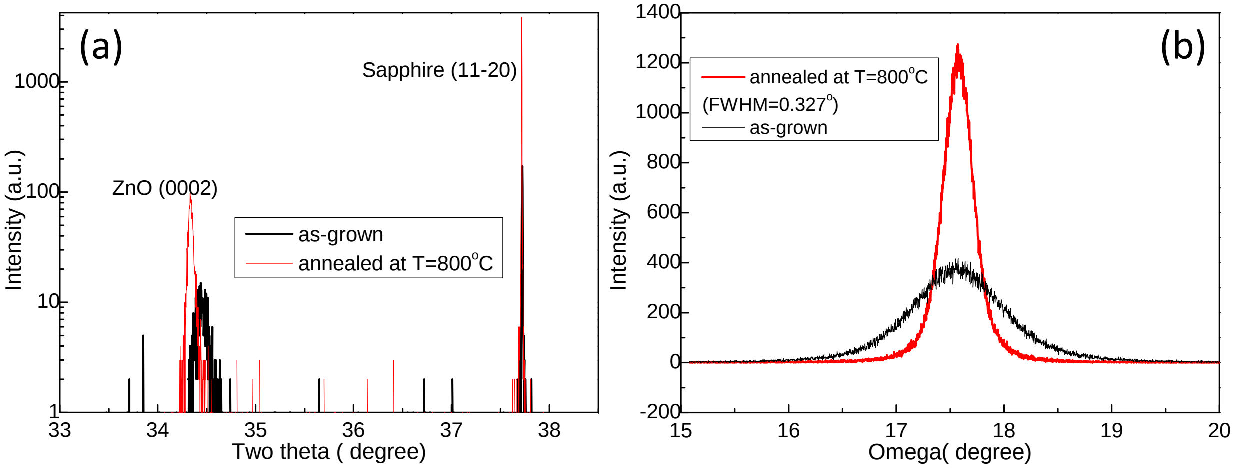

Figure 6.16 (a) XRD 2θ-ω scan and (b) XRD ω scan for ZnO:[N+Te] before and after annealing at temperature of 800 °C in oxygen environment.

6.2.4 Effects of N/O ratio and Te flux

Te cell temperature (T_{Te}) was varied from 350 °C to 425 °C to investigate the Te flux effect. Note that the N-to-O ratio is ~0.27 (4×10^{-6} Torr vs. 15×10^{-6} Torr) and substrate temperature was fixed to be 600 °C. As seen from Figure 6.17, the growth mode for all samples is 3D. The sample grown at higher Te flux could have slightly worse crystalline.

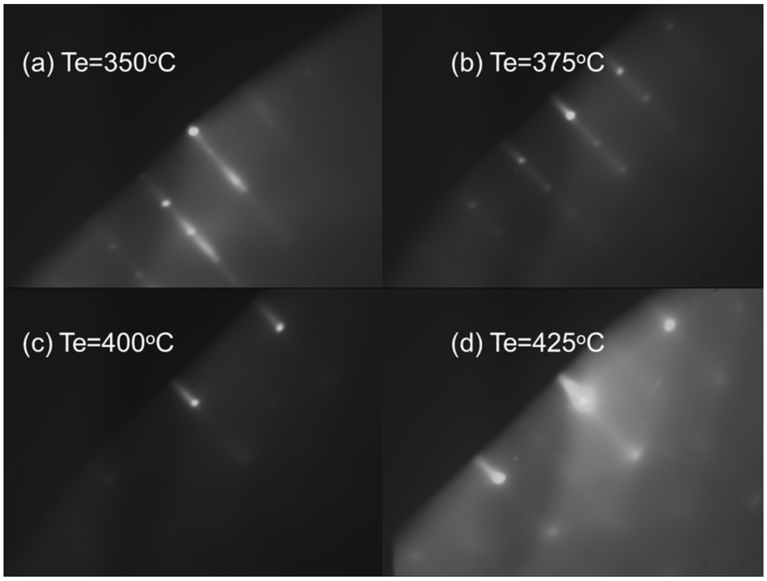

Figure 6.17 RHEED patterns of ZnO:[N+Te] grown under different Te cell temperatures (note: N/O=0.27 and Tsub=600°C).

For all samples, Hall measurement revealed n-type conductivity. In general, the resistivity for the as-grown samples increased from ~0.5 ohm-cm to 12 ohm-cm when T_{Te} was increased from 350 °C to 425 °C. All the samples were annealed in oxygen environment at the temperature of 800 °C. For the annealed sample grown at T_{Te}=425 °C, it became semi-insulating and therefore is not measurable by the Hall system. Figure 6.18 shows the average resistivity measured under different applied current in Hall measurement for the other samples. Compared with the corresponding as-grown samples, the resistivities become larger due to annealing. Meanwhile, the resistivity seems to increase with the increase in T_{Te}. Sometimes, p-type conduction was achieved for less conductive samples. However, the measurement p-type was thought unreliable

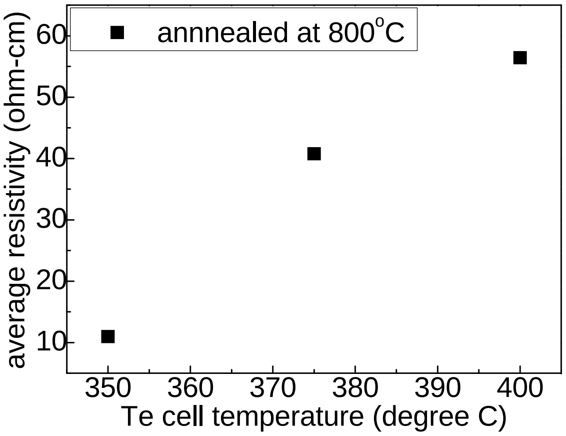

Figure 6.18 Average resistivity of ZnO:[N+Te] grown under different Te cell temperatures (note: N/O=0.27 and Tsub=600^{o}C). For the one grown at T_{Te}=425 ^{o}C, it is semi-insulating after annealing.

Te cell temperature and substrate temperature were fixed to be 375 ^{o}C and 600 ^{o}C, respectively. The ratio of N to O was varied to investigate the N/O ratio effect. The ratios are ~0.235 (4×10^{-6} Torr/17×10^{-6} Torr), ~0.471 (8×10^{-6} Torr/17×10^{-6} Torr), ~0.533 (8×10^{-6} Torr/15×10^{-6} Torr), and ~1 (11×10^{-6} Torr/11×10^{-6} Torr).

Figure 6.19 shows RHEED patterns of ZnO:[N+Te] grown under different N/O ratios as mentioned earlier. It is interesting to see that the ZnO:[N+Te] grown at higher N/O ratio of 1 showed 2D growth mode while all others showed 3D growth mode, which could indicate that a suitable amount of N and Te help to achieve smooth surface [see Figure 6.19 (d)]. The growth rates of the ZnO:[N+Te] samples exhibiting 3D growth mode are comparable, which are about 66-68 nm/h. In contrast, the growth rate of the ZnO:[N+Te] with 2D growth mode is about 55 nm/h. The lower growth rate is due to two reasons. First, the oxygen pressure used for this sample is 11×10^{-6} Torr, which is lower than others. Second, simultaneously supplying of both nitrogen and oxygen can suppress the emission intensity of oxygen as shown in Figure 6.10. So there is no doubt that the growth rate is lower because more nitrogen is supplied together with the much less oxygen.

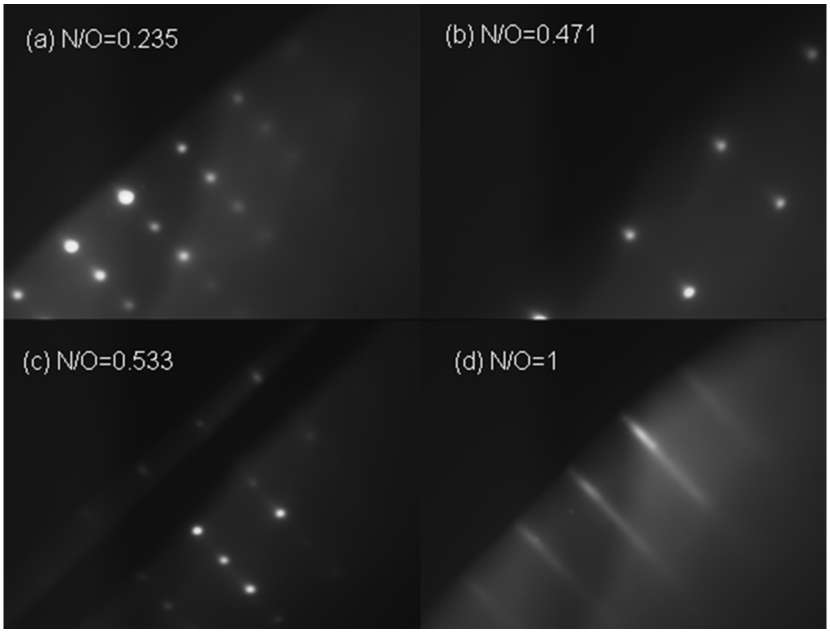

Figure 6.19 RHEED patterns of ZnO:[N+Te] grown under different N/O ratios (note: T_{Te}=375 ^{o}C and Tsub=600^{o}C).

All the four ZnO:[N+Te] samples showed n-type behavior. Their electron concentrations are about 10^{18} cm^{-3} and mobilities are below 7 cm^{2}/V-s. As shown in Figure 6.20 (a), the resistivities of the as-grown ZnO:[N+Te] samples are about 0.5-2 ohm-cm, which do not have a big difference. These ZnO:[N+Te] samples were annealed at temperatures of ~800 ^{o}C in oxygen environment. Figure 6.20 (b) shows that the resistivities of those annealed ZnO:[N+Te] samples increase with the increase in the ratio of N-to-O. Below the dash line in Figure 6.20 (b), stable n-type can be achieved while above that sometimes unstable p-type can be achieved. The achieved p-type is not reliable for the samples with higher resistivities because the default value set in the Hall system for an open circuit is p-type.

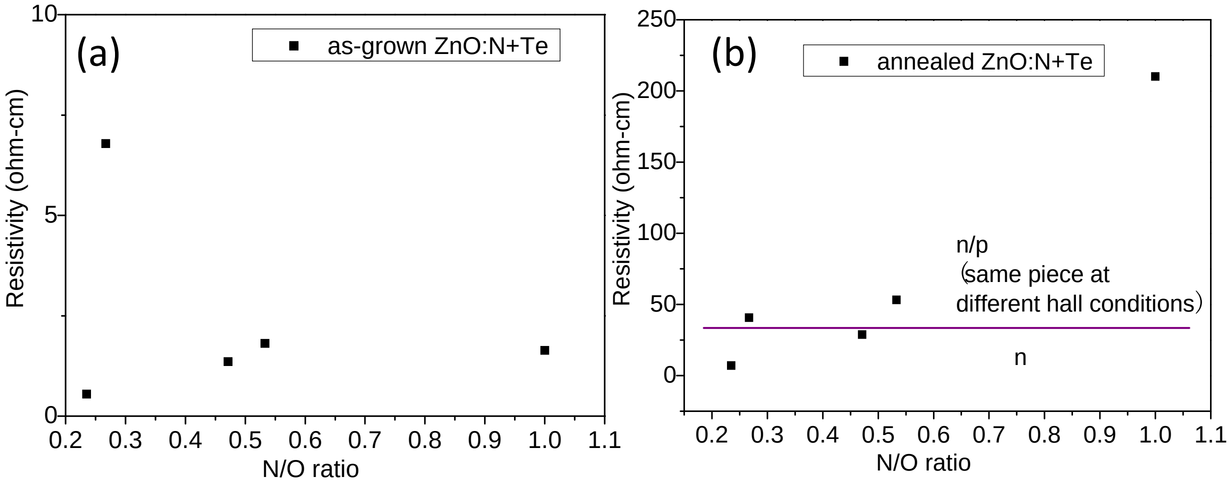

Figure 6.20 Resistivities of ZnO:[N+Te] grown under different N/O ratio. (a) before and (b) after annealing at temperature of 800 ^{o}C in oxygen environment.

6.2.5 Summary for ZnO co-doped with N and Te

Higher substrate temperature of 600 ^{o}C produced less conductive ZnO:N and ZnO:[N+Te] samples. N doped ZnO exhibited n-type conductivity, which could be inconsistent with the reports of p-type ZnO:N in literature and consequently need more studies. Te was found to help suppress the formation of donors in N and Te co-doped ZnO samples. ZnO:[N+Te] samples annealed at the temperature of 800 ^{o}C in oxygen environment became less conductive as compared with the corresponding as-grown samples, which could be due to the improvement in crystalline quality as revealed by XRD measurements, thereby resulting in more incorporation of N . The effect of Te helping suppress the formation of donors were further proved by annealing the reference samples such as un-doped ZnO, N-doped ZnO, and Te-doped ZnO. After annealing, the reference samples became more conductive than the corresponding as-grown samples as well as the annealed ZnO:[N+Te] samples. The annealed ZnO:[N+Te] samples can have resistivities higher than 30 ohm-cm, which sometimes produced p-type behavior but it was believed unreliable due to the Hall system limit. The investigations of either Te flux effect or N-to-O ratio effect indicate that either higher Te flux or higher N-to-O ratio can produce much less conductive ZnO:[N+Te] films. In short, more experiments could be needed to investigate the possibility of p-ZnO co-doped with N and Te by further optimizing the Te flux and N/O ratio.

Chapter 7 Conclusions

(1) Effects of MBE growth parameters including oxygen pressure, Ga flux, and substrate temperature on the GZO properties have been intensively investigated due to the lack of the detailed studies in literature. The ratio of metal (Ga+Zn) to oxygen was found to be a critical parameter to achieve highly conductive and transparent GZO layers, which has strong effects on GZO structural, optical, and electrical properties as revealed by XRD, TEM, PL, transmittance, and Hall measurements. To achieve higher conductivity and higher transmittance, metal-rich conditions (reactive oxygen to incorporated Zn ratio<1) instead of oxygen-rich conditions (reactive oxygen to incorporated Zn ratio>1) are required. The as-grown GZO layers grown under metal-rich conditions exhibited a resistivity below 3×10^{-4} ohm-cm and optical transparency exceeding 90% in the visible spectral range, due to the strong Burstein-Moss shift of the Fermi level deep into the conduction band. The thicknesses were found to have very minor effects on the resistivities of as-grown GZO layers grown under metal-rich conditions. The GZO layers grown under metal-rich conditions are thermally stable in their resistivities up to 500 ^{o}C in air, which is better than the previously reported ZnO-based TCOs (up to 400 ^{o}C). RTA annealing at the temperature of ~600 ^{o}C for 3 mins in nitrogen environment almost does not reduce the resistivities of GZO layers grown under metal-rich conditions while it considerably reduces those for GZO layers grown under near-stoichiometry or oxygen-rich conditions. The worse structural, optical, and electrical properties of GZO grown under oxygen-rich conditions were presumed due to the acceptor-like complexes of (Ga_{Zn}-V_{Zn}). The optimum Ga flux for the lowest resistivity of GZO could be achieved at a Ga cell temperature (600 ^{o}C in this work) resulting in a Ga concentration just below its solubility in ZnO. In this case, all Ga^{3+} ions will substitute Zn^{2+} ions and will not degrade the crystal quality. Instead, the crystal quality could be improved because

the lattice distortion in ZnO caused by the lattice mismatch along the [1-100] direction of either ZnO or sapphire can be reduced due to the smaller radius of Ga^{3+} ion than that of Zn (0.62 Å vs. 0.74 Å). Substrate temperature was found to have only a moderate effect on the electrical properties of GZO layers but greatly affects their surface morphology, which is important in real applications. Higher substrate temperature tends to produce rougher GZO surface. The optimum trade-off between surface roughness and resistivity was achieved at substrate temperature of 350-400 ^{o}C.

(2) Highly conductive and transparent GZO layers (resistivity$<2.5\times10^{-4}$ ohm-cm and transmittance>90% in the visible spectral range) have been successfully applied as p-side transparent electrodes in GaN-based LEDs. GZO grows epitaxially on GaN with GZO [0001]//GaN [0001] and GZO [10-11]// GaN [10-11]. The calculated lattice parameters of GZO grown on p-GaN are very close to those of bulk ZnO, indicating very low lattice distortion even in ZnO films with very high Ga concentrations. These rough surfaces of GZO layers grown on LED structures with 200-Torr p-GaN on the top are thought to be helpful in photon extractions from LED active regions since they could scatter more photons out of the LEDs. The low resistivity of GZO is the basis for current spreading in LED applications which can be improved by RTA annealing. However, the optimum annealing temperatures for GZO and n-side contacts are different. A trade-off between the resistances of p- and n-side contacts should be made to achieve the best performance of the LEDs, unless GZO films are deposited after the n-contact anneal. The LEDs with GZO electrodes (GZO-LEDs) exhibited many advantages over the LEDs with the traditional thin semi-transparent Ni/Au electrodes (Ni/Au-LEDs). The EQE of the GZO-LED is 1.7-2 times higher than that of Ni/Au-LED at high current densities due to what we believe GZO's relatively higher transparency and rough surface. GZO-LEDs can withstand much

higher current densities (4700 A/cm^2) than that of Ni/Au LEDs (3500 A/cm^2) under pulsed mode. The filamentation phenomenon observed for Ni/Au-LEDs was not seen for GZO-LEDs. The highly conductive and transparent GZOs are promising to replace ITO for practical applications in GaN-based devices. The surface morphologies of GaN were demonstrated to be important in affecting the structural and electrical properties of GZO layers. For applications in LEDs, rougher GZO surface is desired and consequently the rougher GaN template is needed. In contrast, for applications in other GaN-based devices which need smooth surface, smooth GaN surface is needed to grow highly conductive and transparent GZO layers with a smooth surface.

(3) Scattering mechanisms governing electron transport in GZO layers with electron concentrations of 10^{18} cm^{-3}-10^{21} cm^{-3} achieved under different growth conditions have been studied by the means of numerical fittings of the temperature-dependent Hall mobility curves. For heavily doped GZO with carrier concentrations above 10^{20} cm^{-3}, the temperature dependence of mobility measured in the range of 15-330K is well described by the Matthiessen’s rule with mobility being limited by polar optical phonon (POP) scattering, and a temperature-independent mobility limited by ionized impurity scattering, compensation of Ga donors with acceptor defects, and electron scattering by low-angle grain boundaries limited by quantum-mechanical tunnelling. The data indicates that ionized impurity scattering is the dominant mechanism limiting the mobility in the range of 15-330 K for GZO layers with high structural quality grown under metal-rich conditions. For these GZO layers grown under metal-rich conditions, POP scattering is the main mechanism responsible for the temperature-dependence for T>150 K and thereby POP scattering cannot be neglected especially at RT. As seen from Figure 5.3 (c), piezoelectric scattering has a much stronger effect than acoustic phonon scattering but both of them can be neglected. It must be pointed out that piezoelectric scattering has a very minor effect

in the temperature range of ~150K-175K, which is comparable to POP scattering in that range. However, both the effects of POP scattering and piezoelectric scattering in that range are weaker and therefore the mobility slightly reduced with the increase in temperature. For the sample with n=~9×10^{20} cm^{-3} and LT mobility of ~51 cm^2/V·s at low temperatures, grain boundary scattering and compensation if present are negligible due to their very minor effects. In contrast, for heavily doped GZO layers grown under oxygen-rich conditions, which have inclined grain boundaries and relatively small grain sizes of 10-20 nm determined by X-ray diffraction (10-30 nm by TEM), the compensation and grain boundary scattering became dominant. The high donor compensation in these layers is caused presumably by (Ga_{Zn}-V_{Zn}) complexes having the lowest formation energy in degenerate GZO grown under oxygen-rich conditions. The evolution of temperature dependences of mobility when the electron concentration reduces from 10^{20} cm^{-3} to 10^{18} cm^{-3} indicates that not only the contribution of grain-boundary scattering becomes stronger but also that the electron transport across boundaries changes from quantum-mechanical tunnelling to thermionic emission. In short, although the significance order of scattering mechanisms can differ for GZO layers with different growth conditions, metal-rich growth conditions, which can produce films with minimal deleterious effects by compensation and grain boundaries, are imperative for attaining high mobilities and high electron concentrations. The intrinsic limitations in RT mobility of GZO, are ionized impurity scattering and POP scattering.

(4) Interestingly, Sb was demonstrated to act as a donor in a wide electron concentration range (upper 10^{16} to upper 10^{19} cm^{-3}) and optimum growth condition along with post-growth annealing in nitrogen environment even produced high mobility of 145.2 cm^2/V·s at 15K or 110 cm^2/V·s at 300K along with the electron concentration of 4.53×10^{19} cm^{-3}. The donor behavior of Sb indicated that the majority Sb ions reside on Zn sites instead of O sites and the thermal

activation energy of the donor determined by the Arrhenius plot is ~0.9 eV. While the reduction in both electron concentration and mobility with increasing Sb flux is caused by the deterioration of crystal quality and the lattice distortion revealed by increased *c* lattice constant and FWHM, which are indicative of the formations of extended defects, point defects, and point-defect complexes related to the extra Sb. The deterioration in crystal quality at higher Sb content, no matter how this happened, could indicate that the large-size-mismatched element of Sb could not be a good candidate to achieve promising p-type conductivity. Substrate temperature effects showed higher substrate temperature can produce SZO with lower electron concentration and lower mobility probably due to the lower incorporation efficiency of Sb, the reduction in native defects in ZnO, and the possible formation of some type of acceptors with Sb involved at higher substrate temperature. Oxygen effects indicate that the probability of the substitution of O with Sb (Sb_O) being an acceptor exists especially in SZO layers grown under lower oxygen pressures but the overwhelming electrons provided by the donors of Sb in Zn sites always make the SZO layers n-type. The electron concentration tends to saturate when T_{Sb} increases up to 480 ^oC for all the oxygen pressures used, which indicates the incorporation of Sb ions on the Zn sites approaches the effective solubility limit.

(5) Higher substrate temperature of 600 ^oC produced less conductive ZnO:N and ZnO:[N+Te] samples. N doped ZnO exhibited n-type conductivity, which could be inconsistent with the reports of p-type ZnO:N in literature and consequently need more studies. Te was found to help suppress the formation of donors in N and Te co-doped ZnO samples. ZnO:[N+Te] samples annealed at the temperature of 800 ^oC in oxygen environment became less conductive as compared with the corresponding as-grown samples, which could be due to the improvement in crystalline quality as revealed by XRD measurements, thereby resulting in more incorporation of

N . The effect of Te helping suppress the formation of donors were further proved by annealing the reference samples such as un-doped ZnO, N-doped ZnO, and Te-doped ZnO. After annealing, the reference samples became more conductive than the corresponding as-grown samples as well as the annealed ZnO:[N+Te] samples. The annealed ZnO:[N+Te] samples can have resistivities higher than 30 ohm-cm, which sometimes produced p-type behavior but it was believed unreliable due to the Hall system limit. The investigations of either Te flux effect or N-to-O ratio effect indicate that either higher Te flux or higher N-to-O ratio can produce much less conductive ZnO:[N+Te] films. More experiments could be needed to investigate the possibility of p-ZnO co-doped with N and Te by further optimizing the Te flux and N/O ratio.

To further carry on the experiments, several things need to be improved or changed. Firstly, different plasma power supplies and MFC controllers should be used for oxygen and nitrogen, respectively. The main problem during the previous growth is the unstable pressure during growth. It is no way to determine whether the variation in oxygen flux or nitrogen flux caused the change in pressure during growth based on the current MBE system. Secondly, NO or NO_2 instead of N_2 as N source should be used. As reported in literature, ZnO doped with N_2 usually results in n-type film, whereas doping with NO_2 or NO sources can lead to p-type films that over time revert to n-type.[141] Since all the ZnO:N layers in this work exhibited n-type conductivity, it is necessary to change the gas source in the co-doping techniques, which could shed more light on the co-doping techniques. Finally, the a-sapphire substrate should be replaced by bulk ZnO, which will probably allow ZnO growth with less extended defects due to no strain and increase the incorporations of N as acceptors.

(6) Although it is still difficult to produce a reliable and reproducible p-type ZnO, ZnO remains a promising material which draws much attention due to its application to LEDs,

varistors, scintillators, solar cells, and transparent electronics.[142] There is no doubt that one of the most difficult tasks in ZnO research is p-type ZnO which requires continuously efforts as well as probably a new perception. Janotti et al.[143] believed that the often-observed n-type conductivity in ZnO cannot be explained by native point defects and to achieve p-type ZnO the impurity such as oxygen introduced during growth and annealing must be well controlled. If reliable and reproducible p-type ZnO materials can be achieved, it will definitely boost the applications of ZnO based on p-n ZnO homojunctions.

Emerging applications of ZnO are UV sensitive photodiodes and transparent field effect transistors[144,145]. Regarding the ZnO transparent thin film transistors or transparent field effect transistors (TTFTs or TFETs), the extensively studied material for the channel is amorphous In/Ga/Zn/O (a-IGZO) because a-IGZO TFTs can have mobilities of an order of magnitude higher than the typical hydrogenated amorphous silicon (a-Si:H) TFTs[146]. Regarding the origin of higher mobility of the amorphous material than its typical crystalline material can be found elsewhere[147]. Most of the a-IGZO TFTs reported by companies exhibited good device characteristics such as a large mobility > 10 cm^2/V-s, a small S value ~0.1 V/decade, and a large On/Off ratio >10^{10}, which satisfy the requirements for practical high-resolution AM_OLED and large-size AMLCD.[148] Although there are still some problems such as difficulty in forming a good electrical contact between an a-IGZO channel and source/drain electrodes[149,150] , instability over environment change[151], and instability under light illumination[152], there is probably no room for universities to involve in this research. It must be pointed out that TFTs with GZO thin films as channel have also been reported by few groups[153-155] but the results are not so good as a-IGZO TFTs.

The above-mentioned TTFTs or TFETs, which are key active devices to substitute a-Si TFTs in active-matrix displays due to their transparency and superior electronic properties, typically have a metal-insulator-semiconductor (MIS) structure (MISFET). However, such MISFETs usually suffer from high operating voltages due to the voltage drop across the insulator and limited switching speed due to carrier scattering at the interface between insulator and semiconductor resulting in low gain.[156] ZnO-based metal-semiconductor FETs (MESFETs) were recently proposed to be a promising alternative to the MISFETs because MESFETs can exhibit much lower operating voltages and higher channel mobilities that ideally equals the semiconductor's Hall-effect mobility. The main contributions in this research are from University of Leipzig in Germany[156-159] , which is worth investigating due to the boom of the transparent electronics.

For the above-mentioned MESFETs, Mg-doped ZnO alloys were used as the channel materials. The field of ZnO-based alloys and heterostructures was just in the initial stage of its development. The purpose of making ZnO alloys is to tailor the band gap of ZnO, which is called band-gap engineering. Recently, $Cd_xMg_yBe_zZn_{1-x-y-z}O$ alloys have attracted much attention because their optical devices operate in the UV and visible region.[142] Mg and Be can be used to increase the band gap of ZnO while Cd is used to decrease the band gap of ZnO. Be is a poison material and therefore it is rarely studied. However, unlike MgO BeO and ZnO share the same hexagonal symmetry and consequently there is no phase segregation problem in BeZnO alloys. Reviews of the status of $Cd_xMg_y(Bez)Zn_{1-x-y(-z)}O$ alloys, their heterostructures and applications can be found elsewhere[112,142,143], which are not repeated here. Due to the promising applications of $Cd_xMg_y(Bez)Zn_{1-x-y(-z)}O$ alloys in fabricating quantum wells, superlattices, 2D electron gas (2DEG) heterostructures, and the devices based on the above-mentioned structures, it is worth investigating this region. Meanwhile, Al or Ga doped Be(Mg)ZnO could be also important as transparent electrode with extended band gap.

In addition to the applications of ZnO doped with Al or Ga as transparent electrodes, they were suggested to be new plasmonic metamaterials due to the low loss in NIR region,[160-163] which is another topic worth investigating.

REFERENCES

[1] Ü. Özgür, D. Hofstetter, and H. Morkoç, Proc. IEEE **98**, 1255 (2010).

[2] Ü. Özgür, Ya. I. Alivov, C. Liu, A. Teke, M. A. Reshchikov, S. Doğan, V. Avrutin, S.-J. Cho, and H. Morkoç, J. Appl. Phys. **98**, 041301 (2005).

[3] V. Avrutin, D. Silversmith, and H. Morkoç, Proc. IEEE **98**, 1269 (2010).

[4] D. C. Look, and B. Claflin, Phys. Stat. Sol. (b) **241**, 624 (2004).

[5] H. von Wenckstern, H. Schmidt, M. Brandt, A. Lajn, R. Pickenhain ,M. Lorenz , M. Grundmann , D. M. Hofmann, A. Polity, B. K. Meyer,H. Saal, M. Binnewies, A.Börger ,K.-D. Becker ,V. A. Tikhomirov , K. Jug, Progress in Solid State Chemistry 37, 153 (2009).

[6] C. H. Park, S. B. Zhang, and S. H. Wei, Phys.Rev.B 66, 073202 (2002).

[7] E. C. Lee, Y. S. Kim, Y. G. Jin, and K. J. Chang, Phys Rev. B 64, 085120 (2001).

[8] S.Limpijumnong, X. Li, S.-H. Wei, and S. B. Zhang, Appl.Phys.Lett. **86**, 211910 (2005).

[9] L. Gao, B. Yao, B. Liu, L. Liu, T. Yang, B. Liu, and D. Shen, J. Chem. Phys **133**, 204501 (2010).

[10] S. H. Park, T. Minegishi, H. J. Lee, J. S. Park, I. H. Im, T. Yao, D. C. Oh, T. Taishi, I. Yonenaga, And J. H. Chang, J. Appl. Phys. 108, 093518 (2010).

[11] H.Y. Liu, V. Avrutin, N. Izyumskaya, Ü. Özgür, and H. Morkoç, Superlattices and Microstructures 48, 458 (2010).

[12] K. Ellmer, and R. Mientus, Thin Solid Films 516, 4620 (2008).

[13] K. Ellmer, J. Phys. D: Appl. Phys. 34, 3097 (2001).

[14] T S Moss Proc. Phys. Soc. Lond. B 67 775, (1954).

[15] T. Minami and T. Miyata, Presentation given at SPIE (Jan 23 2008).

[16] T. Kawashima, T. Ezure, K. Okada, H. Matsui, K. Goto and N. Tanabe, J. Photochem. Photobio. A: Chemistry 164, 199 (2004).

[17] J. W. Bae , S. W. Lee and G. Y. Yeom, Electrochem. Soc. 154, D34 (2007).

[18] M. Oshima, Y. Takemoto and K. Yoshino, Phys. Status Solidi C 6, 1124 (2009).

[19] A. G. Macedo, C. E. Cava, C. D. Canestraro, L. Contini, and L. S. Roman, Microsc. Microanal. 11 (supp 3), 118 (2005).

[20] W. J. Lee, D. Y. Lee, J. S. Song and B. K. Min, Meta. Mater. International, 11/6, 465 (2005).

[21] P. Gerhardinger, and D. Strickler, Key Engineering Mater. 380, 169 (2008).

[22] H. J. Ko, Y, F. Chen, S. K. Hong, H. Wenisch, T. Yao and D. C. Look, Appl. Phys. Lett. 77, 3761 (2000).

[23] T. Minami, Thin Solid Films 516,5822 (2008).

[24] V. Bhosle, A . Tiwari and J. Narayan, Appl. Phys. Lett. 88, 032106 (2006).

[25] B.Z. Dong, G.J. Fang, J.F. Wang, W.J. Guan, X.Z. Zhao, J. Appl. Phys. 101, 033713 (2007).

[26] S. Shirakata, T. Sakemi, K. Awai, T. Yamamoto, Superlattices Microstruct. 39, 218 (2006).

[27] H.Y. Liu, V. Avrutin, N. Izyumskaya, M.A. Reshchikov, Ü. Özgür, and H. Morkoç, Phys. Status Solidi RRL 4, 70 (2010).

[28] H. Kim, D. J. Kim, S. J. Park, and H. Hwang, J. Appl. Phys. 89, 1506 (2001).

[29] J.O. Song, K.K. Kim, S.J. Park, T.Y. Seong, Appl. Phys. Lett. 83, 479 (2003).

[30] C.J. Tun, J.K. Sheu, B.J. Pong, M.L. Lee, M.Y. Lee, C.K. Hsieh, C.C. Hu, G.C. Chi, IEEE Photonics Technol. Lett. 18, 274 (2006).

[31] H. Agura, H. Suzuki, T. Matsushita, T. Aoki, M. Okuda, Thin Solid Films 445, 263 (2003).

[32] S.-M. Park, T. Ikegami, K. Ebihara, Thin Solid Films 513, 90 (2006).

[33] H. Ohta, M. Orita, M. Hirano, H. Tanji, H. Kawazoe, H. Hosono, Appl. Phys. Lett. 76, 2740 (2000).

[34] J.-K. Sheu, Y. S. Lu, M.-L. Lee, W. C. Lai, C. H. Kuo, and C.-J. Tun, Appl. Phys. Lett., 90, 263511 (2007).

[35] T. Minami, T. Yamamoto, and T. Miyata, Thin Solid Films, 366/1, 63 (2000).

[36] P. H. Chen, W. C. Lai, Li-Chi Peng, C. H. Kuo, Chi-Li Yeh, J. K. Sheu, and C. J. Tun, IEEE Transac. Electron Devic., 57/1, 134 (2010).

[37] S. B. Qadri, H. Kim, H. R. Khan, A. Pique, J. S. Horowitz, D. Chrisey, W. J. Kim, E. F. Skelton, Thin Solid Films, 377-378, 750 (2000).

[38] H. Kim, C. M. Gilmore, J. S. Horwitz, A. Pique, H. Murata, G. P. Kushto, R. Schlaf, Z. H. Kafa. and D. B. Chrisey: Appl. Phys. Lett. 76, 259 (2000).

[39] O Nakagawara, Y Kishimoto, H Seto, Y Koshido, Y Yoshino and T Makino, Appl. Phys. Lett. 89, 091904-3 (2006).

[40] K. Yim, H. W. Kim and C. Lee, Mater. Sci. Technol. 23, 108 (2007).

[41] P. K. Nayak, J. Yang, J. Kim, S. Chung, J. Jeong, C. Lee and Y. Hong J. Phys. D: Appl. Phys. 42, 035102-6 (2009).

[42] Z. Yang, D. C. Look, and J. L. Liu, Appl. Phys. Lett. 94, 072101-3 (2009).

[43] V. Assuncao, E. Fortunato, A. Marques, H. Aguas, I. Ferrira, M.E.V. Costa, R. Martins, Thin Solid Films 427, 401 (2003).

[44] H. Kato, M. Sano, K. Miyamoto, and T. Yao, J. Cryst. Growth **237–239,** 538 (2002).

[45] T. Muranaka, A. Nisii, T. Uehara, T. Sakano, Y. Nabetani, T. Akitsu, T. Kato, T. Matsumoto, S. Hagihara, O. Abe, S. Hiraki and Y. Fujikawa, J. Kr. Phys. Soc. **53**, 2947 (2008).

[46] Ü. Özgür, H. Liu, X. Li, and X. Ni, H. Morkoç, Special issue of the Proc. of IEEE **98**, 1180 (2010).

[47] C. H. Kuo, S. J Chang, Y. K. Su, R. W. Chuang, C. S. Chang, L. W. Wu, W. C. Lai, J. F. Chen, J. K. Sheu, H. M. Lo, and J. M. Tsai, Mater. Sci. Eng. **B106**, 69 (2004).

[48] M. Yamada, T. Mitani, Y. Narukawa, S. Shioji, I. Niki, S. Sonobe, K. Deguchi, M. Sano, and T. Mukai, Jpn. J. Appl. Phys., Part 2, **41**, L1431 (2002).

[49] S. I. Na, G. Y. Ha, D. S. Han, S. S. Kim, J. Y. Kim, J. H. Lim, D. J. Kim, K. I. Min, and S. J. Park, IEEE Photonics Technol. Lett., **18**, 1512 (2006).

[50] J. K. Sheu, Y. K. Su, G. C. Chi, M. J. Jou, C. M. Chang, C. C. Liu, and W. C. Hung, Appl. Phys. Lett. **74**, 2340 (1999).

[51] J. O Song, J.-S. Ha, T.-Y. Seong, IEEE TRANSACTIONS ON ELECTRON DEVICES, **57**, 42 (2010).

[52] C. H. Kuo, C. L. Yeh, P. H. Chen, W. C. Lai, C. J. Tun, J. K. Sheu, and G. C. Chi, Electrochemi. Solid-State Lett., **11** (9), H269 (2008).

[53] J.-K. Sheu, M.-L. Lee, Y. S. Lu, and K. W. Shu, IEEE J. QUANTUM ELECTRONICS, **44**, 1211 (2008).

[54] K. Tamura, K. Nakahara, M. Sakai, D. Nakagawa, N. Ito, M. Sonobe, H. Takasu, H. Tampo, P. Fons, K. Matsubara, K. Iwata, A. Yamada, and S. Niki, phys. stat. sol. (a) **201**, 2704 (2004).

[55] K. NAKAHARA, K. TAMURA, M. SAKAI, D. NAKAGAWA, N. ITO, M. SONOBE, H. TAKASU, H. TAMPO, P. FONS, K. MATSUBARA, K. IWATA, A. YAMADA and S. NIKI, Jpn. J. Appl. Phys., **43**, L180 (2004).

[56] H.L. Hartnagel, A.L. Dawar, A.K. Jain, C. Jagadish, Semiconducting Transparent Thin Films, Institute of Physics Publishing, Philadelphia, 1995.

[57] J. Y. W. Seto, J. Appl. Phys. 46, 5247 (1975).

[58] J. Bruneaux, H. Cachet, M. Froment and A. Messad, Thin Solid Films, 197, 129 (1991).

[59] K. Ellmer, R. Mientus, Thin Solid Films 516, 5829 (2008).

[60] T. Minami, S. Suzuki, and T. Miyata, Mat. Res. Soc. Symp. Proc. Vol. 666 (2001) F1.3.1-F1.3.7 (MRS).

[61] J. Steinhauser, S. Faÿ, N. Oliveira, E. Vallat-Sauvain, and C. Ballif, APPLIED PHYSICS LETTERS 90, 142107 (2007).

[62] F. Ruske, A. Pflug, V. Sittinger, B. Szyszka, D. Greiner, B. Rech, Thin Solid Films 518, 1289 (2009).

[63] M. Chen, Z. L. Pei, X. Wang, Y.H. Yu, X.H. Liu, C. Sun, and L. S. Wen, J. Phys. D: Appl. Phys. 33, 2538 (2000).

[64] J.J. Robbins, J. Harvey, J. Leaf, C. Fry. C.A. Wolden, Thin Solid Films 473, 35 (2005).

[65] B. D. Ahn, S. H. Oh, and H. J. Kim, M. H. Jung, Y. G. Ko, Appl. Phys. Lett. 91, 252109 (2007).

[66] W. Guo, A. Allenic, Y. B. Chen, X. Q. Pan, Y. Che, Z. D. Hu, and B. Liu, Appl. Phys. Lett. 90, 242108 (2007).

[67] S. B. Zhang, S. H. Wei, and A. Zunger, Phys. Rev. B 63, 075205 (2001).

[68] C. G. Van de Walle, Phys. Rev. Lett. 85, 1012 (2000).

[69] F. X. Xiu, Z. Yang, L. J. Mandalapu, D. T. Zhao, J. L. Liu, and W. P. Beyermann, Appl. Phys. Lett. 87, 152101 (2005).

[70] A. Allenic, W. Guo, Y. Chen, M. B. Katz, G. Zhao, Y. Che, Z. Hu, B. Liu, S. B. Zhang, and X. Pan, Adv Mater 19, 3333 (2007).

[71] U. Wahl, E. Rita, J. G. Correia, A. C. Marques, E. Alves, and J. C. Soares, and ISOLDE Collaboration, Phys. Rev. Lett. 95, 215503 (2005).

[72] M. Kumar, S.-Y. Choi, Appl. Surf. Sci. 255, 2173 (2008).

[73] M. D. McCluskey and S. J. Jokela, J. Appl. Phys 106, 071101 (2009).

[74] Y. W. Heo, Y. W. Kwon, Y. Li, S. J. Pearton, and D. P. Norton, Appl. Phys. Lett. 83, 1128 (2003).

[75] T. Aoki, Y. Shimizu, A. Miyake, A. Nakamura, Y. Nakanishi, and Y. Hatanaka, Phys. Stat. Sol. (b) 229, 911 (2002).

[76] U. Wahl, J. G. Correia, T. Mendonca, and S. Decoster, Appl. Phys. Lett. 94, 261901 (2009).

[77] S. Limpijumnong, S. B. Zhang, S. H. Wei, and C. H. Park, Phys. Rev. Lett. 92, 155504 (2004).

[78] L. J. Mandalapu, Z Yang, F. X. Xiu, D. T. Zhao, and J. L. Liu, Appl. Phys. Lett. 88, 092103 (2006).

[79] Z. Yang, S. Chu, W. V. Chen, L. Li, J. Kong, J. Ren, P. K. L. Yu, and J. Liu, Appl. Phys. Expr. 3, 032101 (2010).

[80] K. Samanta, P. Bhattacharya, and R. S. Katiyar, J. Appl. Phys. 108, 113501 (2010).

[81] F. Friedrich, I. Sieber, C. Klimm, M. Klaus, Ch. Genzel, and N. H. Nickel, Appl. Phys. Lett. 98 131902 (2011).

[82] Z. Zhao, L. Hu, H. Zhang, J. Sun, J. Bian, J. Zhao, Appl. Surf. Scie. 257, 5121 (2001).

[83] X H Pan, Z Z Ye, Y J Zeng, X Q Gu, J S Li, L P Zhu, B H Zhao, Y Che, and X Q Pan, J. Phys. D: Appl. Phys. 40, 4241 (2007).

[84] T. Yang, B. Yao, T.T. Zhao, G.Z. Xing, H. Wang, H.L. Pan, R. Deng, Y.R. Sui, L.L. Gao, H.Z. Wang, T. Wu, D.Z. Shen, J. Alloys and Compounds 509, 5426 (2011).

[85] X. Pan, Z. Ye, J. Li, X. Gu, Y. Zeng, H. He, L. Zhu, Y. Che, Appl. Surf. Scie. 253, 5067 (2007).

[86] D. H. Kim, N. G. Cho, K. S. Kim, S. Han, H. G. Kim, J. Electroceram 22, 82 (2009).

[87] O. Bierwagen, T. Ive, C. G. Van de Walle, and J. S. Speck, Appl. Phys. Lett. 93, 242108 (2008).

[88] T. Yamamoto, Codoping Method for Solutions of Doping Problems in Wide-Band-Gap Semiconductors (Wiley-VCH, Diepenbeek-Hassels, Belgium, 2002), pp. 423–433.

[89] M. Joseph, H. Tabata, H. Saeki, K. Ueda, and T. Kawai, in Fabrication of the Low-Resistive p-Type ZnO by Codoping Method (Elsevier Science B.V., Awaji Island, Hyogo, 2001), pp. 140–148.

[90] F. Zhu-Ge, Z.-Z. Ye, L.-P. Zhu, J.-G. Lu, B.-H. Zhao, J.-Y. Huang, Z.-H. Zhang, L. Wang, and Z.-G. Ji, J. Cryst. Growth 268, 163 (2004).

[91] T. Yamamoto, H. Katayama-Yoshida, Jpn. J. Appl. Phys. 38, L166 (1999).

[92] K. Nakahara, H. Takasu, P. Fons, A. Yamada, K. Iwata, K. Matsubara, R. Hunger, and S. Niki, J. Cryst. Growth 237, 503 (2002).

[93] H. L. Porter, A. L. Cai, and J. F. Muth, J. Narayan, Appl. Phys. Lett. 86, 211918 (2005).

[94] H. L. Porter, J. F. Muth, J. Narayan, J. V. Foreman, and H. O. Everitt, J. Appl. Phys. 100, 123102 (2006).

[95] S. H. Park, T. Minegishi, J. S. Park, H. J. Lee, T. Taish, I. Yonenaga, D. C. Oh, M. N. Jung, J. H. Chang, S. K. Hong, and T. Yao, Mater. Res. Soc. Symp. Proc. 1201, 1201-HO5-25 (2010).

[96] S. H. Park, T. Minegishi, D. Oh, H. Lee, T. Taishi, J. Park, M. Jung, J. Chang, I. Im, J. Ha, S. Hong, I. Yonenaga, T. Chikyow, and T. Yao, Appl. Phys. Expr. 3, 031103 (2010).

[97] K. Tang, S. Gu, K. Wu, S. Zhu, J. Ye, R. Zhang, and Y. Zheng, Appl. Phys. Lett. 96, 242101 (2010).

[98] D.C. Look, K. D. Leedy, D. H. Tomich, and B. Bayraktaroglu, Appl. Phys. Lett. **96**, 062102 (2010).

[99] K. H. Kim, and E. Arifin, Metals & Mater. International **13**, 489 (2007).

[100] D. O. Demchenko, B. Earles, H.Y. Liu, V. Avrutin, N. Izyumskaya, Ü. Özgür, and H. Morkoç, Phys. Rev. B **84**, 075201 (2011).

[101] S. K. Han, H. S. Lee, D. S. Lim, S.-K. Hong, N. Yoon, D.-C. Oh, B. J. Ahn, J.-H. Song, and T. Yao, J. Vac. Sci. Technol. A **29**, 03A111 (2011).

[102] J.A.Sans, G.Martínez-Criado, J.Pellicer-Porres, J.F.Sánchez-Royo, A.Segura, Appl. Phys. Lett. **91**, 221904 (2007).

[103] B.D.Ahn, J.H.Kim, H.S.Kang, C.H.Lee, S.H.Oh, K.W.Kim, G.Jang, S.Y.Lee, Thin SolidFilms **516,** 1382 (2008).

[104] T.Minami, T.Kuboi, T.Miyata, Y.Ohtani, Phys. Status Solidi (a) **205**, 255 (2008).

[105] J. L. Zhao, X. W. Sun, H. Ryu. Y. B. Moon, Optical Materials **33**, 768 (2011).

[106] X. Li, H.Y. Liu, S. Liu, X. Ni, M. Wu, V. Avrutin, N. Izyumskaya, Ü. Özgür, and H. Morkoç, Phys. Stat. Solidi (a) **207,** 1993 (2010).

[107] B. Thangaraju, *Thin Solid Films*, **402**, 71 (2002).

[108] T. Minami, *Semicond. Sci. Technol.* **20**, S35-S44 (2005).

[109] H.Y. Liu, X. Li, S. Liu, X. Ni, M. Wu, V. Avrutin, N. Izyumskaya, Ü. Özgür, A.B. Yankovich, A.V. Kvit, P.M. Voyles, and H. Morkoç, Phys. Status Solidi (c) **8,** 1548 (2011).

[110] H.Y. Liu, X. Li, F. Zhang, V. Avrutin, N. Izyumskaya, Ü. Özgür, A.B. Yankovich, A.V. Kvit, P.M. Voyles, and H. Morkoç, Proc. SPIE 8262, 826226 (2012).

[111] C. Erginsoy, Phys. Rev., **79**, 1013 (1950).

[112] D. S. Ginley, Handbook of Transparent Conductor Chapter 7 (Springer, 2010).

[113] B. K. Meyer, J. Sann, D. M. Hofmann, C. Neumann and A. Zeuner, Semicond. Sci. Technol., 20 (2005) S62.

[114] B. Pödör, phys. stat. sol., **16** (1966) K167.

[115] K. Seeger, “Semiconductor Physics”, (Springer, Berlin, 1991).

[116] Y. S.Jung, O. V. Kononenko, W.-K. Choi, Solid State Communications **137,** 474 (2006).

[117] J. Bardeen and W. Shockley, Phys. Rev., 80 (1950) 72.

[118] C. Solbrig, Z. Phys., 211 (1968) 429.

[119] D.C. Look, K.D. Leedy, L. Vines, B.G. Svensson, A. Zubiaga, F. Tuomisto, D.R. Doutt, and L. J. Brillson, Phys. Rev. B 84, 115202 (2011).

[120] D.C. Look, D.C. Reynolds, J.R. Sizelove, R.L. Jones, C.W. Litton, G. Cantwell, and W.C. Harsch, Solid State Communications 105, 399 (1998).

[121] P. Wagner and R. Helbig, J. Phys. Chem. Solids, 35 (1974) 327.

[122] D. L. Rode, in “Semiconductors and Semimetals”, Ed.: R. K. Willardson and A. C. Beer (Academic Press, New York, 1975), p. 1.

[123] H. Morkoç, Handbook on Nitride Materials and Devices Vol. 2. Chapter 3 (Wiley, 2008).

[124] R. L. Petritz, Phys. Rev. 104, 1508 (1956).

[125] M. L. Tarng, J. Appl. Phys. 49 (7), 4069 (1978).

[126] J.H. Werner, Polycrystalline Semiconductors III - Physics and Technology, p. 213 (Scitec Publ., Switzerland, Zug, Switzerland,1993).

[127] D.H.Zhang, H.L. Ma, Appl. Phys. A 62, 487 (1996).

[128] S. Riedel, J. Röber, T. Geβner, Microelectronic Engineering 33, 165 (1997).

[129] S. K. Vasheghani, Farahani, T. D. Veal, P.D.C. King, J. Zúñiga-Pérez, V. Munoz-Sanjosé, and C. F. McConville, J. Appl. Phys. 109, 073712 (2011).

[130] S. M. Sze, Kwok K. NG, Physics of Semiconductor Devices, 3rd Edition, Chapter 1, (Wiley, 2007).

[131] R. Holm, J. Appl. Phys. 22, 569 (1951).

[132] M.L. Addonizio, A. Antonaia, G. Cantele, C. Privato, Thin Solid Films 349, 93 (1999).

[133] R. C. Scott, K. D. Leedy, B. Bayraktaroglu, D. C. Look, and Y. H. Zhang, Appl. Phys. Lett. 97, 072113 (2010).

[134] Y.K. Fu, C.H. Kuo, C.J. Tun, C.W. Kuo, W.C. Lai, G.C. Chi, C.J. Pan, M.C. Chen, H.F. Hong and S.M. Lan, J. Crys. Growth **310**, 4456 (2008).

[135] L. M. Wong, S. Y. Chiam, J. Q. Huang, S. J. Wang, J. S. Pan, and W. K. Chim, Appl. Phys. Lett. **98**, 022106 (2011).

[136] B.L. Zhu, S. J. Zhu, X.Z. Zhao, F. H. Su, G.H. Li, X.G. Wu, and J. Wu, Phys. Status Solidi A **208**, 843 (2011).

[137] H. Morkoç, Handbook on Nitride Materials and Devices Vol. 1. Chapter 3 (Wiley, 2008).

[138] Y. Chen, D. M. Bagnall, H. J. Koh, K. T. Park, K. Hiraga, Z. Zhu, and T. Yao, J. Appl. Phys. **84**, 3912 (1998).

[139] J. L. Lyons, A. Janotti, and C. G. Van de Walle, Appl. Phys. Lett. **95**, 252105 (2009).

[140] M. C. Tarun, M. Z. Iqbal, and M. D. McCluskey, AIP Advances **1**, 022105 (2011).

[141] X. Li, Y. Yan, T. A. Gessert, C. DeHart, C. L. Perkins, D. Young, and T. J. Coutts, Electrochem. Solid-State Lett. **6**, 56 (2003).

[142] Y.S. Choi, J.W. Kang, D.K. Hwang, and S.-J. Park, IEEE Transactions on Electron Devices 57, 26 (2010).

[143] A. Janotti, C. G V. d. Walle, Rep. Prog. Phys. 72, 126501 (2009).

[144] "Zinc Oxide Bulk, Thin Films and Nanostructures"; edited by C. Jagadish and S. Pearton (Elsevier, Amsterdam, 2006).

[145] J. F. Wager, Science, **300**, 1245 (2003).

[146] M. Ofuji, K. Abe, H. Shimizu, N. Kaji, R. Hayashi, M. Sano, H. Kumomi, K. Nomura, T. Kamiya, and H. Hosono, IEEE Electron Device Letters **28**, 273 (2007).

[147] H. Hosona, J. Non-Crystalline Solids **352**, 851 (2006).

[148] K. Nomura, T. Kamiya, Y. Kikuchi, M. Hirano, H. Hosono, Thin Solid Films **518**, 3012 (2010).

[149] J.-S. Park, J.K. Jeong, Y.-G. Mo, H.D. Kim, S.-I. Kim, Appl. Phys. Lett. **90**, 262106 (2007).

[150] Y. Shimura, K. Nomura, H. Yanagi, T. Kamiya, M. Hirano, H. Hosono, Thin Solid Films **516**, 5899 (2008).

[151] J.Y. Kwon, J.S. Jung, K.S. Son, T.S. Kim, M.K. Ryu, K.B. Park, Y.S. Park, S.Y. Lee, J.M. Kim, Proc. AMFPD '08, 2008, p. 287.

[152] D.P. Gosain, T. Tanaka, Proc. AMFPD '08, 2008, p. 291.

[153] V. P. Verma, D.-H. Kim, H. Jeon, M. Jeon, W. Choi, Thin Solid Films **516**, 8736 (2008).

[154] H.-Q. Huang, J. Sun, F.-J. Liu, J.-W. Zhao, Z.-F. Hu, Z.-J. Li, X.-Q. Zhang, Y.-S. Wang, Chin. Phys. Lett. **28**, 128502 (2011).

[155] H. Jeon, V. P. Verma, A. Hwang, S. Lee, C. Park, D.-H. Kim, W. Choi, and M. Jeon, Jap. J. Appl. Phys. 47, 87 (2008).

[156] H. Frenzel, A. Lajn, H. V. Wenckstern, M. Lorenz, F. Schein, Z. Zhang, and M. Grundmann, Adv. Mater. **22**, 5332 (2010).

[157] H. Frenzel, A. Lajn, M. Brandt, H. V. Wenckstern, G. Biehne, H. Hochmuth, M. Lorenz, and M. Grundmann, Appl. Phys. Lett. **92**, 192108 (2008).

[158] H. Frenzel, F. Schein, A. Lajn, H. V. Wenckstern, and M. Grundmann, Appl. Phys. Lett. **96**, 113502 (2010).

[159] F. J. KlÜpfel, A. Lajn, H. Frenzel, H. V. Wenckstern, and M. Grundmann, J. Appl. Phys. **109**, 074515 (2011).

[160] P. R. West, S. Ishii, G. V. Naik, N. K. Emani, V. M. Shalaev, and A. Boltasseva, Laser & Photon. Rev., 1-13 (2010)/DOI 10.1002/Ipor.200900055.

[161] G. V. Naik, J. Kim, and A. Boltasseva, Optical Materials Express 1, 1090 (2011).

[162] G. V. Naik, V. M. Shalaev, and A. Boltasseva, Proc. SPIE 7754, 77540M (2010).

[163] A. Frolich, and M. Wegener, Optical Materials Express 1, 883 (2011).

Vita

Huiyong Liu
Date of Birth: Feb. 20, 1978
Citizenship: P. R. China
Email: huiyongliuster@gmail.com

EDUCATION

Doctor of Philosophy, Electrical Engineering .... Aug. 2012
Virginia Commonwealth University, *Richmond, VA,* ***USA***
Dissertation: Investigation of Doped ZnO by Molecular Beam Epitaxy for n- and p-type Conductivity

Master of Science, Optical Engineering..May 2007
Rose-Hulman Institute of Technology, *Terre Haute, IN,* ***USA***
Thesis**:** Sensing Liquid Levels and Measuring the Contact Angles Using Optical Techniques

Bachelor of Engineering, Electrical Engineering... July 2002
Shenyang Normal University, *Shenyang, Liaoning,* ***China***

RESEARCH INTERESTS

- Molecular beam epitaxy (MBE)
- III-nitride and ZnO optoelectronics
- GaN or ZnO based HFETs
- Growth and characterization of perovskite oxides
- Type II superlattice infrared photodetectors

RESEARCH EXPERIENCES

Graduate Research Assistant .... Jun. 2007–Aug. 2012
Microelectronics Materials & Device Laboratory-Virginia Commonwealth University (Richmond, VA, USA)

- Applied highly conductive and transparent GZO layer as transparent electrodes in InGaN-based LEDs;
- Simulated carrier spillover effect on the efficiency droop in InGaN-based LEDs;
- Doped ZnO with Ga, As, Sb, N, Te, Mg, and Be using Molecular Beam Epitaxy for n-type/p-type conductivity/band gap engineering;
- Prepared PbTiO3/PbO bridge layers to integrate Pb(Ti,Zr)O_3 on (0001) GaN or MgO/ZnO bridge layers to integrate Ba(Sr,Ti)O_3 on a-plane sapphire;
- Grew complex oxide materials (Pb(Ti,Zr)O_3, Ba(Sr,Ti)O_3, $BaFe_{12}O_{19}$,) using Molecular Beam Epitaxy;
- Characterized thin films using RHEED, XRD, AFM, SEM/EDX, Lakeshore Hall measurement system, Hysteresis system, I-V/C-V measurement system, and PL;

PUBLICATIONS

- **in journals**

A.V. Kvit, A.B. Yankovich, V. Avrutin, **H. Liu**, N. Izyumskaya, Ü. Özgür, H. Morkoç, P.M. Voyles, "Impurity Distribution and Microstructure of Ga-doped ZnO Films Grown by Molecular Beam Epitaxy", submitted to JAP.

H.Y. Liu, V. Avrutin, N. Izyumskaya, Ü. Özgür, A.B. Yankovich, A.V. Kvit, P.M. Voyles, and H. Morkoç, "Donor Behavior of Sb in ZnO"— J. Appl. Phys. **112**, 033706 (2012).

A.B. Yankovich, A.V. Kvit, X. Li, F. Zhang, V. Avrutin, **H.Y. Liu**, N. Izyumskaya, Ü. Özgür, H. Morkoç, and P.M. Voyles, "Hexagonal-Based Pyramid Void Defects in GaN and InGaN**",** J. Appl. Phys.**111**, 023517 **(**2012).

H.Y. Liu, V. Avrutin, N. Izyumskaya, Ü. Özgür, A.B. Yankovich, A.V. Kvit, P.M. Voyles, and H. Morkoç, "Electron scattering mechanisms in GZO films grown on a-sapphire substrates by plasma-enhanced molecular beam epitaxy", J. Appl. Phys. **111**, 103713 (2012).

D. O. Demchenko, B. Earles, **H.Y. Liu**, V. Avrutin, H. Morkoç, "Impurity complexes and conductivity of Ga doped ZnO", Phys. Rev. B **84**, 075201 (2011).

H.Y. Liu, X. Li, S. Liu, X. Ni, M. Wu, V. Avrutin, N. Izyumskaya, Ü. Özgür, A.B. Yankovich, A.V. Kvit, P.M. Voyles, and H. Morkoç, "InGaN based Light emitting diodes utilizing Ga doped ZnO as a highly transparent contact to p-GaN ", Phys. Status Solidi (c) **8** (2011) 1548-1551.

X. Li, X. Ni, **H.Y. Liu**, F. Zhang, S. Liu, J. Lee, V. Avrutin, Ü. Özgür, T. Paskova, G. Mulholland, K.R. Evans and H. Morkoç, "On the reduction of efficiency loss in polar *c*-plane and non-polar *m*-plane InGaN light emitting diodes", Phys. Status Solidi (c) **8**, (2011) 1560-1563.

H.Y. Liu, V. Avrutin, N. Izyumskaya, Ü. Özgür, and H. Morkoç, "Transparent conducting oxides for electrode applications in light emitting and absorbing devices" Superlattices & Microstructures **48**, (2010) 458-484.

H.Y. Liu, V. Avrutin, N. Izyumskaya, M.A. Reshchikov, Ü. Özgür, and H. Morkoç, "Highly conductive and optically transparent GZO films grown under metal-rich conditions by plasma assisted MBE", Phys. Status Solidi RRL **4**, No. 3-4, 70-72 (2010).

Huiyong Liu, Vitaliy. Avrutin, Bo. Xiao, E. Rowe, H.R. Liu, Ü. Özgür, and Hadis Morkoç, "Epitaxial relationship of MBE grown barium hexaferrite (0001) films on sapphire (0001)", *J. Crystal Growth*, **312** (2010) 671-675.

X. Li, **H.Y. Liu**, S. Liu, X. Ni, M. Wu, V. Avrutin, N. Izyumskaya, Ü. Özgür, and H. Morkoç, "InGaN based Light emitting diodes with Ga doped ZnO as transparent conducting oxide", Phys. Stat. Solidi (a) **207** (2010) 1993–1996.

Ümit Özgür, **H. Liu**, X. Li, and X. Ni, Hadis Morkoç, "GaN-based Light-Emitting Diodes: Efficiency at High Injection Levels", Proc. of IEEE **98**/7 1180 (2010).

Xing Li, **Huiyong Liu**, X. Ni, Ümit Özgür, and Hadis Morkoç, "Effect of carrier spillover and Auger recombination on the efficiency droop in InGaN-based blue LEDs", Superlattices & Microstructures **47**, (2010) 118-122.

Bo Xiao, Hongrui Liu, Vitaliy Avrutin, Jacob H. Leach, Emmanuel Rowe, **Huiyong Liu**, Ümit Özgür, and Hadis Morkoç, "Epitaxial growth of (001)-oriented Ba0.5Sr0.5TiO3 thin films on a-plane sapphire with an MgO/ZnO bridge layer", Appl. Phys. Lett. **95**, 212901 (2009);

V. Avrutin, **H.Y. Liu**, N. Izyumskaya, B. Xiao, Ü. Özugür, H. Morkoc, "Growth of Pb(Ti,Zr)O_3 thin films by metal-organic molecular beam epitaxy", *J. Crystal Growth* **311** (2009) 1333–1339.

Bo Xiao, Vitaliy Avrutin, **Huiyong Liu**, Ümit Özgür; Hadis Morkoç, Changzhi Lu "Large pyroelectric effect in undoped epitaxial Pb(Zr,Ti)O3 thin films on SrTiO3 substrates", Applied Physics Letters, Volume **93**, Issue 5, 052913 (2008).

B. Xiao, X. Gu, I. Natalia, A. Vitaliy, J. Xie, **H.Y. Liu**, M. Hadis, "Structural and electrical properties of Pb(Zr,Ti)O3 grown on (0001) GaN using a double PbTiO3/PbO bridge layer", Applied Physics Letters, Volume **91**, 182908.1-182908.3 (2007).

- **in Conferences**

A.B. Yankovich, A.V. Kvit, X. Li, F. Zhang, V. Avrutin, **H.Y. Liu**, N. Izyumskaya, Ü. Özgür, H. Morkoç, and P.M. Voyles, "Absence of Lateral Composition Fluctuations in Aberration-corrected STEM Images of an InGaN Quantum Well at Low Dose", MRS Proceedings, 1432 : mrss12-1432-g04-03 **(**2012).

H.Y. Liu, X. Li, F. Zhang, V. Avrutin, N. Izyumskaya, Ü. Özgür, A.B. Yankovich, A.V. Kvit, P.M. Voyles, and H. Morkoç, "Electrical properties of ZnO:Ga as a transparent conducting oxide in InGaN based light emitting diodes" Proc. SPIE 8262, 826226 (2012)

A.B. Yankovich, A.V. Kvit, **H.Y. Liu**, X. Li, F. Zhang, V. Avrutin, N. Izyumskaya, Ü. Özgür, H. Morkoç, and P.M. Voyles, "Pyramid nano-voids in GaN and InGaN", Proc. SPIE 8262, 826205 (2012)

J.D. McNamara, M. Foussekis, **H. Liu**, H. Morkoç, M.A. Reshchikov, A.A. Baski, "Temperature dependent behavior of the SPV for n-type GaN", Proc. SPIE 8262, 826213 (2012)

A.B. Yankovich, A.V. Kvit, X. Li, F. Zhang, V. Avrutin, **H.Y. Liu**, N. Izyumskaya, Ü. Özgür, H. Morkoc, and P.M. Voyles, "Indium Composition Variation in Nominally Uniform InGaN Layers Discovered by Aberration-Corrected Z-contrast STEM" Microscopy and Microanalysis **17**, 1386-1387 (2011)

H.Y. Liu, X. Li, S. Liu, X. Ni, V. Avrutin, N. Izyumskaya, Ü. Özgür, A.B. Yankovich, A.V. Kvit, P.M. Voyles, M.A. Reshchikov, and H. Morkoç, "Optimization of ZnO:Ga properties for application as a transparent conducting oxide in InGaN based light emitting diodes" Proc. SPIE 7939, 79392E (2011); doi:10.1117/12.875515

A.B. Yankovich, A.V. Kvit, X. Li, F. Zhang, V. Avrutin, **H.Y. Liu**, N. Izyumskaya, Ü. Özgür, H. Morkoc, and P.M. Voyles, "Vertical composition variation in nominally uniform InGaN layers revealed by aberration-corrected STEM imaging", Proc. SPIE 7939, 79391E (2011) doi:10.1117/12.889392.

H.Y. Liu, V. Avrutin, N. Izyumskaya, M.A. Reshchikov, S. Wolgast, C. Kurdak, A.B. Yankovich, A. Kvit, P. Voyles, Ü. Özgür, and H. Morkoç, "Effect of Growth Conditions of p-GaN Templates on Electronic and Structural Properties of GZO Films grown by Plasma-enhanced MBE", MRS Proceedings, 1315, mrsf10-1315-mm09-03, (2011) doi: 10.1557/opl.2011.716.

J.D. McNamara, J.D. Ferguson, M. Foussekis, I. Ruchala, M.A. Reshchikov, A.A. Baski, **H. Liu**, V. Avrutin, and H. Morkoç, "Surface Characterization of Ga-doped ZnO layers", MRS Proceedings, 1315, mrsf10-1315-mm06-25 (2011) doi:10.1557/opl.2011.722.

H.Y. Liu, X. Li, X. Ni, V. Avrutin, N. Izyumskaya, Ü. Özgür, and H. Morkoç, "InGaN light emitting diodes with highly transparent ZnO:Ga electrodes", GALLIUM NITRIDE MATERIALS AND DEVICES V Book Series: Proc. SPIE 7602 (2010) 76020I-76020I-8

V. Avrutin, **H.Y. Liu**, N. Izyumskaya, M.A. Reshchikov, Ü. Özgür, A.V. Kvit, P.M. Voyles, and H. Morkoç, "Effect of growth conditions on structural and electrical properties of Ga-doped ZnO films grown by plasma-assisted MBE", MRS Proceedings, 1201, 1201-H05-20 (2009). doi: 10.1557/PROC-1201-H05-20.

Xianfeng Ni, Xing Li, **Huiyong Liu**, Natalia Izyumskaya, Vitaliy Avrutin, Ümit Özgür, Hadis Morkoç, Tanya Paskova, Greg Mullholland and Keith R. Evans (2009). On the Light Emission in GaN Based Heterostructures at High Injection. MRS Proceedings, 1202 , 1202-I02-06 doi:10.1557/PROC-1202-I02-06